FABRICATION AND MECHANICAL CHARACTERIZATION OF NOVEL HYBRID CARBON-FIBER/EPOXY COMPOSITES REINFORCED WITH TOUGHENING/SELF-REPAIRING NANOFIBERS AT INTERFACES

A Thesis
Submitted to the Graduate Faculty
of the
North Dakota State University
of Agriculture and Applied Science

By

Md. Arifur Rahman

In Partial Fulfillment of the Requirements
for the Degree of
MASTER OF SCIENCE

Major Department:
Mechanical Engineering

February 2012

Fargo, North Dakota

North Dakota State University
Graduate School

Title

Fabrication and Mechanical Characterization of Novel Hybrid Carbon-Fiber/Epoxy Composites Reinforced with Toughening/Self-Repairing Nanofibers at Interfaces

By

Md. Arifur Rahman

The Supervisory Committee certifies that this ***disquisition*** complies with North Dakota State University's regulations and meets the accepted standards for the degree of

MASTER OF SCIENCE

SUPERVISORY COMMITTEE:

Dr. Xiangfa Wu
Chair

Dr. Ghodrat Karami

Dr. Chad Ulven

Dr. Jing Shi

Approved:

3/19/12	Dr. Alan Kallmeyer
Date	Department Chair

ABSTRACT

This research was aimed at fabrication and characterization of novel hybrid carbon-fiber/epoxy composites reinforced with toughening/self-repairing nanofibers at interfaces. For interfacial toughening, continuous electrospun polyacronitrile (PAN) and carbon nanofibers (CNFs) were incorporated between carbon fabrics to form the ultrathin toughening interlayers after resin infusion and curing. Mode I interlaminar fracture tests showed that PAN nanofibers can noticeably enhance the fracture toughness of Epon 862 based composites, while the toughening results were scattered for SC-15 resin based system. Furthermore, core-shell dicyclopentadiene (DCPD)/PAN nanofibers mats were fabricated by coelectrospinning, which were inserted between carbon fabrics and formed the ultrathin self-repairing interlayers after resin infusion and curing. Three-point bending tests showed up to 100% recovery of the flexural stiffness of pre-damaged composite specimens by the core-shell nanofibers. The research demonstrated novel high-strength, self-healing lightweight structural composites for broad applications.

ACKNOWLEDGMENTS

First and foremost, I would like to start by expressing my gratitude to my advisor Prof. Xiangfa Wu for giving me the opportunity to work with him. I am very fortunate to work with him. His guidance and support are the reasons I was able to accomplish this work. As an excellent mentor, Dr. Wu directed me through various obstacles in my thesis work. In the course of my study I learned how to deal with difficult situations. His strong personality, work ethics, hardworking nature, and deep understanding of the research problems have made him a model for me.

I extend my gratitude to my defense committee members Prof. Ghodrat Karami, Prof. Chad Ulven and Prof. Jing Shi for their continuous advice and supervision on my master's thesis and research process. Also, I would like to give my special thanks to Dr. Chad Ulven for his helpful suggestions on the composite manufacturing process.

I would like to thank Mr. Zhengping Zhou, Mr. Mike Fuqua, and Mr. Scott Payne for their continuous supports in the laboratories, in which Mr. Zhengping produced all the PAN and core-shell nanofibers used for this research, and Mr. Scott Payne assisted to take all the SEM images used in this thesis. In addition, I would like to thank all of my fellow graduate friends for their supports.

I would also like to thank the Mechanical Engineering Department at North Dakota State University for giving me the opportunity to complete this master's program.

Finally, it is also my great pleasure to express a deep sense of gratitude to my parents, who gave everything they could to make me what I am today. Their contributions to this work, though invisible, are invaluable to me.

The support of this research by the ND NASA EPSCoR, ND DOE EPSCoR-SUNRISE Program, NDSU Development Foundation, and Faculty Research Initiative Grant is gratefully appreciated.

TABLE OF CONTENTS

LIST OF TABLES

LIST OF FIGURES

LIST OF APPENDIX FIGURES

CHAPTER 1. INTRODUCTION

Advanced polymer composites made of polymeric resins reinforced with high-performance fibers (such as boron and carbon fibers) were first introduced due to the seminal research in the U. S. Air Force Materials Laboratory and several U.S. universities in 1960s (Tsai, 2005). Due to their unique high specific strength and toughness, superior manufacturability, and excellent corrosion resistance and fatigue tolerance, polymer composites have been extensively integrated in aerospace, aeronautical and ground vehicles, sports utilities (e.g. fishing rods, tennis rackets, racing cycles, boats, etc.), and industrial sectors (e.g. wind mills, offshore derricks, etc.) (Jones, 1998; Chand, 2000). For instance, advanced polymer composites now play a crucial role in a wide range of contemporary generation military aerospace systems, resulting in weight saving of 10-60% compared to metal design, with 20-30% being typical as achieved by the U. S. Air Force B2 bomber and recent F-22 raptor (24%). Besides, commercial transport aviation has also witnessed a remarkable increase in adoption of polymer composites in the past several decades; the newly launched Boeing 787 Dreamliner is made from 50% polymer composites by weight and over 50% by volume.

Yet, there continue to be barriers and challenges to the expanded exploitation of composites technology for primary transport structures such as wing and fuselage in aircrafts. The primary considerations include damage tolerance, fuel containment, lightening protection, repair and nondestructive inspection, modeling and failure prediction, cost-effective fabrication, and so on (Tenney and Pipes, 2001). Among these, interlaminar failure due to high interlaminar stresses (especially near laminate edges) and the existence of relatively weak resin-rich interlayers in polymer composites has attracted substantial attentions in composites community in the past three decades. Though several effective toughening techniques and concepts have been successfully formulated such as free-edge delamination-suppression designs (Jones, 1999), laminate stitching (Dransfield et al., 1994), modification of matrix resins by integrating with rigid and rubbery micro and nanoparticles (Garg and Mai, 1988; Low and Mai, 1990), controlled fiber debonding and fiber surface treatment (Kim and Mai, 1990), interleaving (Carlsson and Aksoy, 1999), etc. Though having been integrated in composite structures, limitations still exist in these toughening techniques such as the high costs, noticeable weight penalty, substantial structural modification, and so on.

Recently, by utilizing contemporary progress in fabrication of continuous nanofibers, a novel delamination suppression technique has been proposed for polymer composites via incorporating discrete, ultrathin toughening nanofiber layers at ply interfaces (Dzenis and Reneker, 2001; Dzenis 2008; Wu 2003; 2009). The continuous tough plastic nanofibers with diameter ~300 nm were produced by electrospinning (Reneker and Chun, 1996). The potential toughening mechanisms consist of improvement of interlaminar fracture toughness and suppression of the singular interlaminar stresses near free-edges of the laminates since the entangled nanofibers at ply interfaces behave much like the hooks and loops in Velcro (Dzenis 2008; Wu 2003; 2009). This toughening technique has been validated on aerospace-grade unidirectional (UD) and angle-ply carbon-fiber/epoxy composite laminates made from UD prepregs in a wide range of loading rates including static and quasistatic to fatigue and impact loadings (Wu, 2003; 2009). The main advantages of this interface toughening technique include low-weight penalty (<1% in volume fraction), low nanofiber content, and low impact to the processing and global effective properties of the composites (Wu 2003; 2009). Thus, this toughening technique can be easily integrated into conventional composite fabrication process. However, this toughening technique was only validated experimentally on advanced polymer composites based on UD carbon-fiber/epoxy prepregs and cured in vacuum chamber-based hot press (Wu 2003; 2009). No experimental validation of this toughening technique has been performed yet on other polymer composite systems fabricated by means of other composites processing techniques such as the low-cost vacuum-assisted resin transfer molding (VARTM) method.

Furthermore, similar to almost all other conventional toughening techniques, this interface toughening scheme does not consider the self-repairing function. As a result, the mechanical property of polymer composites reinforced with such toughening nanofibers at ply surfaces will still irreversibly degrade. Thus, in principle, a desirable interface toughening technique for advanced polymer composites would carry both toughening and self-repairing functions. Once interlaminar fracture happens, highly localized healing agent will release at composite interfaces and heal interface cracks and damages, mimicking the bleeding mechanism in mammals (White, 2001; Wool, 2001; van der Zwaag, 2007; Youngblood and Sottos, 2008). Resolution of the above outstanding problems will be directly beneficial to development of high-strength, high-toughness, lightweight polymer composites for aerospace and aeronautical applications. This research is expected to yield novel hybrid multiscale self-repairing structural composites with much higher interlaminar fracture toughness and damage tolerance, than those under contemporary use, and innovative damage self-repairing function (NDSU Invention

Disclosure, 2012). The self-repairing function of the composites will remarkably enhance the material reliability as well as durability and therefore dramatically decrease the maintenance cost as well, which is particularly preferred in high-value aerospace and aeronautical structures and vehicles such as military aircrafts and spacecrafts (Carlson and Goretta, 2006).

The research in this thesis work was formulated in resolving the above outstanding problems experimentally, which includes (1) fabrication of novel hybrid multiscale polymer composites with interface reinforced toughening/self-repairing nanofibers that were produced by electrospinning, and (2) interfacial toughening and self-repairing evaluation and related toughening/self-repairing mechanism exploration based on electronic scanning microscopy (SEM).

Specifically, the overall objectives of this study include:

- Processing of novel hybrid multiscale carbon-fiber/epoxy composites reinforced with electrospun nanofibers at interfaces by means of wet lay-up followed by VARTM technique.
- Three-point bending test and mode I interlaminar fracture test based on double cantilever specimen (DCB) configuration for examination of the interfacial toughening effect of electrospun nanofibers (e.g., PAN) on the novel hybrid multiscale carbon-fiber/epoxy composites. Consequently, SEM-based fractographical analysis of the fractured surfaces to explore the micro and nanoscale toughening mechanisms. Use of two-parameter Weibull model for the data reduction of the interlaminar fracture tests in the statistical sense.

- Processing of the novel hybrid self-repairing carbon-fiber/epoxy composites reinforced with electrospun core-shell nanofibers loaded with healing agent at interfaces by using wet lay-up, followed by VARTM technique.
- Three-point bending test for examination of the self-repairing effect of the novel hybrid self-repairing composites. Recovery rate of the flexural stiffness of the composite specimens was employed as the self-healing criterion. Consequently, SEM-based fractographical analysis of fractured surfaces to explore the toughening and self-repairing mechanism at micro and nanoscale.

The layout of the rest thesis is divided into four parts. Chapter 2 provides the literature review on electrospinning/coelectrospinning, concept of interface toughening, self-repairing composites, etc. Chapter 3 describes the theoretical derivation of several formulas that were used for data reduction of three-point bending and short-beam shear tests of the novel hybrid multiscale composites. Numerical examples were demonstrated to apply the new formulas for interlaminar stress calculation. Chapter 4 delineates the detailed procedure on fabrication and toughening characterization of novel hybrid multiscale carbon-fiber/epoxy composites reinforced with electrospun nanofibers at interfaces. In this chapter, details of specimen fabrication, test instrumentation, loading, and test set-up will be discussed; statistical methods were adopted for data reduction and understanding the significance of the interfacial toughening effect. Chapter 5 demonstrates the experimental study on fabrication and self-repairing characterization of the novel hybrid self-repairing carbon-fiber/epoxy composites reinforced with electrospun core-shell healing-agent-loaded nanofibers at interfaces. Consequently, conclusions, recommendations, and future works of the study are summarized in Chapter 6.

CHAPTER 2. LITERATURE REVIEW

This chapter presents a review of the current research works related to the thesis study. First, a brief introduction to conventional polymer composites and nanocomposites is given, and then interfacial toughening mechanisms of laminated composites are discussed. Consequently, concept of self-repairing structural composites will be introduced.

2.1. Polymer composites

2.1.1. Concept

The idea of composite materials is to combine two or more chemically and physically distinct phases to create a new material with properties superior to those of the constituents. In the case of polymer matrix composites (PMCs), the polymer matrices are reinforced with the high-strength, high-modulus fillers/fibers. For such materials, the polymer matrices bind and protect the reinforcing fillers/fibers, and the fillers or fibers serve as the load-carrying elements (Jang, 1994; Jones, 1999). In addition, the polymeric matrix materials can be further modified by incorporating a variety of fillers for the purpose of improving their mechanical, chemical, or electrical properties (Thostenson et al., 2005) or sometimes merely reducing the cost of the materials (Chan et al., 2002). When using fibrous reinforcing phase in composites, the discrete fibrous phase can be short or long; when using reinforcing fabrics, the fabrics can made of the long fibers in UD or woven format. Furthermore, the reinforcing fillers can also be clay, silica, carbon black, or corn husk, among others. The distribution of reinforcing fibers or fillers can have different arrangements. Figure 2.1 shows a schematic diagram of different fiber reinforcement arrangements in conventional composites. Besides, reinforcing fibers/fillers can also be made of the same material or a combination of fibers/fillers made of different materials (hybrid composites).

Chopped fibers (random) Oriented short fibers Fiber/particulate hybrids

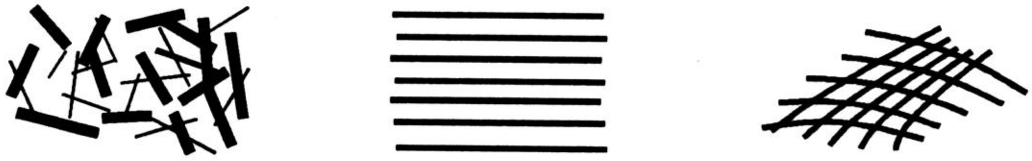

Short fiber hybrids Unidirectional continuous fibers Filament wound cylindrical

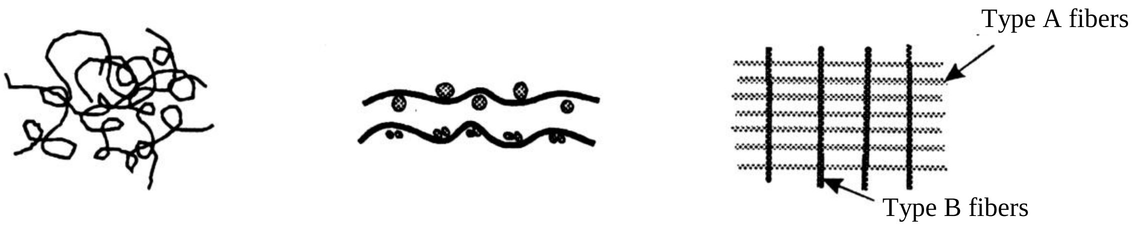

Long/interpenetrating Woven fabrics Continuous/hybrid

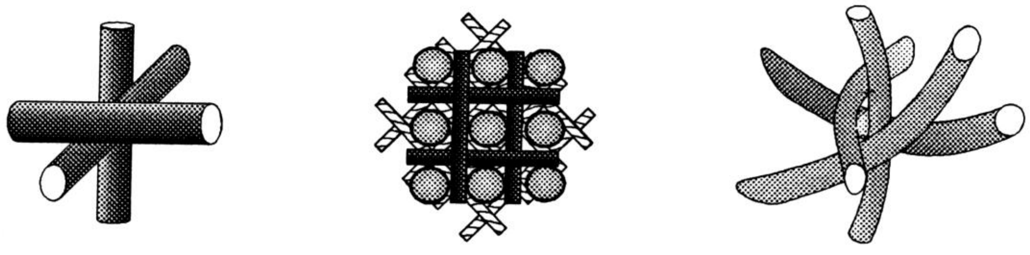

Orthogonal 3-D Multi-axial 3-D weave 3-D braid

Figure 2.1. Different fiber architectures in reinforced composite materials (Jang, 1994).

Because of their favorable mechanical properties such as high specific strength and toughness, superior manufacturability, and excellent corrosion resistance and fatigue tolerance, fiber reinforced composites have been integrated into various aerospace, aeronautical and ground vehicles, sports utilities (e.g. fishing rods, racing cycles, boats, etc.), and industrial sectors (e.g. wind mills, etc.).

2.1.2. Failure modes and toughening techniques

Just a few years ago, people generally believed that polymer composites made of polymer matrix reinforced with nanofillers (e.g. carbon nanotubes-CNTs) were expected to carry exceptional mechanical properties superior to traditional polymer composites. However, due to some processing problems such as agglomeration of filler materials, poor interface bonding strength, defects in the nanomaterials, etc., the mechanical properties improvement of such composites (nanocomposites) are still disappointing, especially when compared with conventional continuous fiber composites (Alexandre & Dubois, 2000; Thostenson et al., 2005; Coleman et al., 2006; Dzenis, 2008). Thus, continuous fiber-reinforced composites still play a dominate role in advanced composites market superior to nanocomposites, especially when considering their mechanical properties. Yet, due to combination of several constituents of different physical and chemical properties in a composite fabrication process, especially when considering the mismatch of their surface properties (e.g. wetting, coefficient of thermal expansion, etc.), defects of various types can be induced in composite materials. Besides, the damage process observed in polymer composites is much more complicated and highly depends upon the microstructures and physical properties of the constituents as well as the types of loads (Talreja, 1994). In general, the failure process in polymer composites is a purely stochastic process and the damage is well distributed throughout the composites (Dzenis, 1996). Typically, damage gradually accumulates and coalesces to form macroscopic cracking shortly before the final catastrophic failure. Moreover, the failure modes in composites are significantly different from those observed in metals, where the failure was typically controlled by the growth and propagation of a single master crack till the occurrence of the catastrophic failure. During the service life, fiber-reinforced polymer composites typically experience various failure modes such as matrix cracking/crazing, fiber breakage, fiber/matrix debonding, and interlaminar delamination (Jones, 1999; Dzenis and Joshi, 1994; Dzenis and Qian, 2001). Figure 2.2 illustrates the common failure modes in polymer composites.

In principle, matrix cracking happens when the tensile stress of the polymer exceeds the maximum tensile strength of the matrix. Fiber breakage happens if the normal stress reaches the ultimate tensile strength of the fiber. Fiber/matrix debonding depends on the interfacial strength properties. Due to the planar architecture of fiber reinforcement, the out-of-plane mechanical properties (e.g., shear strength and interlaminar fracture toughness) of conventional composite laminates are much lower compared to their in-plane counterparts. Thus, interlaminar fracture has been reported as the most severe and catastrophic failure mode in composites. Because of these limitations, significant effort has been devoted to understanding the mechanical and failure behaviors of fiber reinforced composites for better and more reliable applications.

Furthermore, recent progress in nanotechnology has provided a promising technique to enhance the mechanical, electrical, chemical, thermal, etc. properties of fiber reinforced composites. For example, mechanical properties such as interlaminar fracture toughness, flexural and shear strength of laminated composites can be improved by incorporating nanomaterials into the composites. In practice, nanostructured materials can be used to modify the entire resins for composite manufacturing or incorporate into the localized resin-rich interlayers between plies of the composites. Various types of nanostructured materials such as CNTs, nanofibers, , nanoclay, etc. have been considered for the nanoreinforcement of composites (Dzenis & Reneker, 2001; Thostenson et al., 2002; Wu, 2003; 2009; Veedu et al., 2006; Bekyarova et al., 2007; Chen et al., 2011 & 2012). Among a variety of nanomaterials, continuous nanofibers produced by means of electrospinning have attracted significant attention since the last decade. Compared to other nanostructured materials such as CNTs and clay nanoparticles, electrospun nanofibers carry their unique advantages such as continuity, low cost in fabrication, controllable fiber diameter and material properties, etc. A brief discussion on classification of nanomaterials and nanofiber production by electrospinning will be made below.

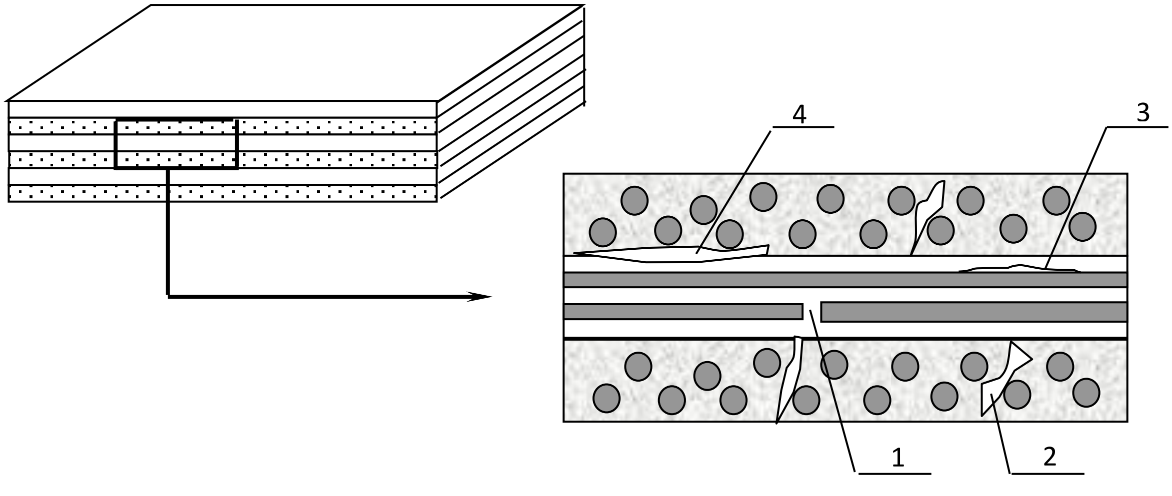

Figure 2.2. Typical damage modes in a cross-ply composite (Wu, 2009): (1) Fiber breakage; (2) matrix cracking; (3) fiber/matrix debonding; and (4) delamination.

Typical 1D nanostructured materials include nanorods, organic and inorganic nanowires, CNTs, and polymer and CNFs, among others. 1D nanomaterials are potential nanoreinforcement that can be used for developing various structural nanocomposites. Among these, CNTs as the hottest candidate have been intensively investigated for improving the mechanical properties of structural materials. However, growing experimental results have projected increasing doubts on the reinforcing effect of CNTs in structural materials due to various reasons aforementioned; in addition, cost of CNTs also limits the broad use of CNTs for large parts such as aerospace and aeronautical structures. Besides, nanoparticles (e.g. clay nanoparticles) have been also widely considered as nanoreinforcing phase to develop novel polymer nanocomposites. It has been shown that clay nanoparticles can improve the mechanical properties of a variety of polymers including the tensile strength, stiffness, and fracture toughness (Koo, 2006; Alexandre & Dubois, 2000; Subramaniyan & Sun, 2007). To date, clay nanoparticle reinforced polymer nanocomposites have found extensive applications, especially in various vehicle parts since the seminal study in Toyota Inc., Japan. Yet, experimental studies also indicated that clay nanoparticles have limited reinforcing effect in the interlaminar fracture toughness of fiber-reinforced polymer composites due potentially to the fact that clay platelets could be parallel to the reinforcing fibers (Subramaniyan & Sun, 2008). To reinforce the interlaminar properties of fiber-reinforced polymer composites, recent research indicated that electrospun polymer nanofibers (Wu, 2009) and functionalized CNTs (Wicks et al., 2010; Sager et al., 2011) can be employed to enhance the interlaminar fracture toughness of fiber-reinforced polymer composites. Yet, the current interlaminar toughening research was focused on carbon-fiber/epoxy systems based on UD prepregs and cured using vacuum-chamber based hot press. No work has been reported yet on interfacial toughening of woven fabrics/epoxy systems produced by means of VARTM technique. In addition, as the CNTs/CNFs are costly and the manufacturing is also a complicated process. Thus, we are most interested in utilizing the low-cost continuous nanofibers produced by means of the electrospinning technique to improve the mechanical properties of fiber-reinforced polymer composites

2.2. Electrospinning and continuous nanofibers

Electrospinning is a novel low-cost, top-down nanomanufacturing technique based on the principle of electrohydrodynamics, capable of producing continuous nanofibers of synthetic and natural polymers and polymer derived carbon, silicon, metallic materials with the diameter less than fifty nanometers to over one micrometer. (Reneker et al., 2000; Theron et al., 2001; Yarin et al. 2001). The schematic setup of electrospinning is shown in Figure 2.3. To date, more than two hundred synthetic and natural polymers have been successfully electrospun into nanofibers (Wu et al. 2012) such as polyethylene oxide (PEO), polyacrylonitrile (PAN), polybenzimidazole (PBI), etc. In the electrospinning process, a sufficiently high DC voltage is applied between a capillary tube containing polymer solution and a conductive nanofiber collector. When the electric field reaches the threshold value, a thin jet ejects from the meniscus surface. After a variety of jet instabilities and solvent evaporation, the jet is deposited on the collector to form a nonwoven nanofiber mat. Besides, a few other effective methods have also been formulated for nanofiber production such as needleless electrospinning (Yarin & Zussman, 2004) and bubble electrospinning (Yong & Ji-Huan, 2007), which can be used for mass production of the polymer nanofibers. Figure 2.4 shows a few typical nanofibers produced by electrospinning in our recent research.

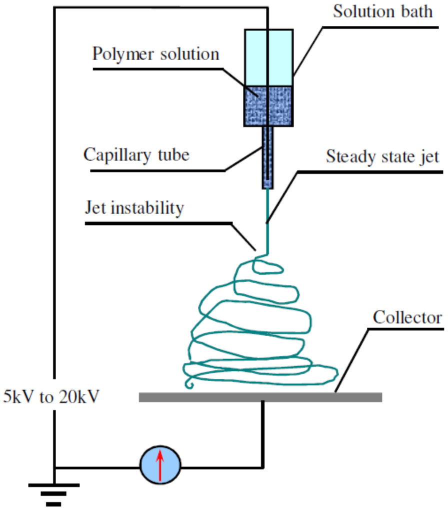

Figure 2.3. Schematic of electrospinning setup (Wu, 2009).

So far, electrospun nanofibers have been considered for use in many areas including tissue engineering, wound dressing, energy storage, and so on. Electrospun nanofibers have also been considered for toughening structural composites (Dzenis, 2008; Wu, 2003; 2009). Yet, no experimental works have been performed on whether and how much the interlaminar fracture toughness can be improved for fiber fabric-reinforced polymer composites fabricated by other processing techniques such as the low-cost VARTM technique. In this thesis, electrospun nanofibers were further used to reinforce the interlaminar region of carbon-fiber/epoxy composites produced by wet lay-up followed by the VARTM technique. Ultrathin nanofiber films were produced and inserted between neighboring plies as toughening interlayers. Several advantages of electrospun nanofibers can be exploited for such advanced composites. As the nanofiber interlayers are very thin and do not alter the thickness and weight of the laminated composites. This interface toughening technique can be easily merged into the conventional processing techniques. Also, the cost of electrospun nanofibers is much lower than CNTs.

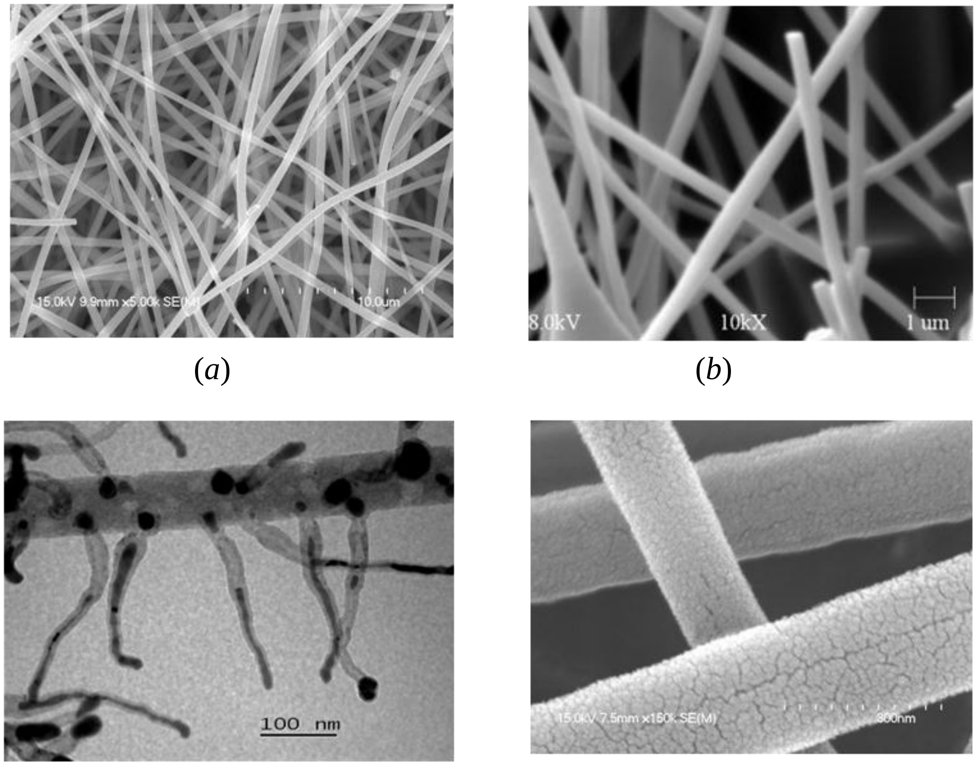

(*a*) (*b*)

(*c*) (*d*)

Figure 2.4. Continuous nanofibers produced by electrospinning: (a) polyimide (PI), (b) polyacrylonitrile (PAN)-based carbon, (c) CNT-grafted carbon (Lai et al., 2008), and (d) nano-cracked chromium-coated nanofibers (Wu et al., 2012).

2.3. Nanotechnology-based interface toughening

For laminated composites, delamination is one of the crucial failure modes. Improving the delamination resistance of polymer composites is one of the most challenging tasks facing composites community and industry. In the past four decades, several effective toughening methods have been formulated to improve the delamination resistance of polymer composites such as modification of laminate design, modification of edge design, modification of matrix resins, and interleafing technique (Wu, 2003). To be very brief, modification in design of laminates is to place the plies with a proper stacking-sequence. Also, 3D weaving and braiding can be utilized to effectively suppress delamination. Edge design can also be adopted via edge reinforcement or edge modification. In edge reinforcement edge cap, stitching or interleaved adhesive layers can be applied. On the other hand, ply termination, notching, and tapering can be considered for edge modification. In addition, concept of resin modification is similar to the toughening technique through adding micro or nanofillers into the resin to achieve desired properties. Finally, interlaminar fracture toughness can also be improved by interleafing, in which discrete plastic thin films are inserted at interfaces. With the recent development of electrospinning technique, Dzenis and Reneker (2001) and Dzenis (2008) proposed a novel interface toughening technique for polymer composites, in which ultrathin fibers (e.g., electrospun polymer nanofiber mats) are placed at ply interfaces to form ultrathin fiber reinforced interlayers to enhance the interlaminar fracture toughness of polymer composites. To do this, the electrospun nanofiber layers are placed in-between the constituent laminas. Figure 2.5 shows schematically how the interleaves can be placed layer by layer.

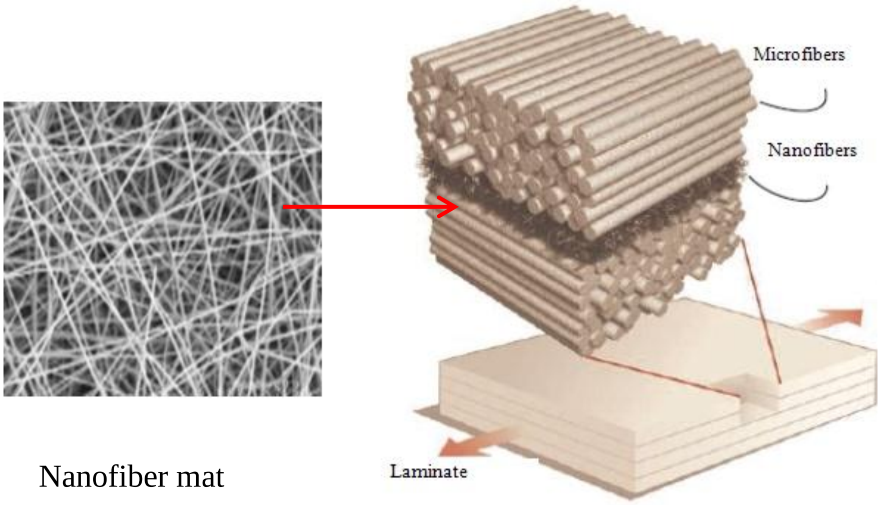

Nanofiber mat

Figure 2.5. Concept of hybrid multiscale nanocomposites (Dzenis, 2008).

2.4. Polymer nanofiber bridging concept

Multiple mechanisms are potentially responsible for interfacial toughening of polymer composites reinforced with nanofibers at interfaces including nanofiber breakage, pull-out, debonding, plastic deformation (necking), and nanofiber related crack kinking and stress shielding, among others. Figure 2.6 illustrates the interfacial failure process of polymer composites toughened with nanofibers at interfaces in which either fiber breakage or interface debonding can be triggered according to the properties of interface and constituents. If the fiber breakage is the case then the failure is brittle in nature, however, if the debonding of fiber-matrix interface takes place, the failure is ductile where sliding of fiber causes this ductility. In this case matrix cracking and interface sliding can be explained with different fracture conditions such as simple fiber breakage with the propagation of crack. This can happen when the interface is strong. In this case where stress is redistributed as the broken fiber exerts tension on the fracture surface, multiple matrix cracks can initiate to redistribute the stress, or matrix shear damage can occur in the case of weak matrix.

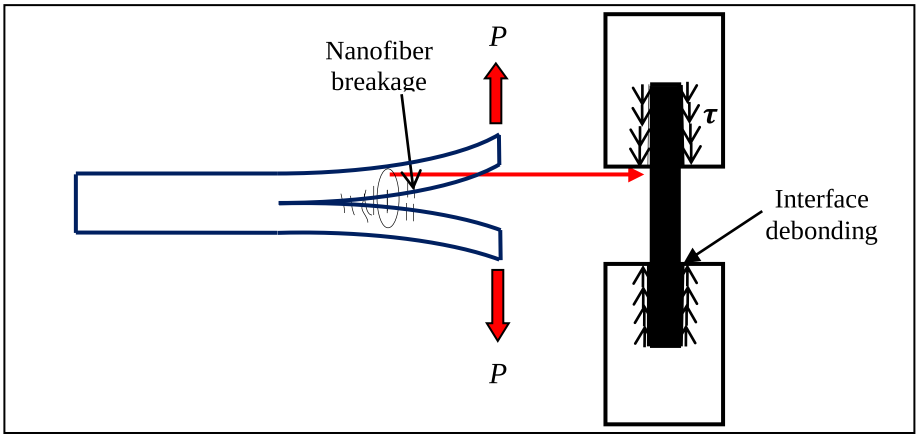

Figure 2.6. Schematic interfacial toughening mechanisms of a DCB composite sample reinforced with nanofibers at interface.

2.5. Data reduction of mode I fracture test

For the data reduction, the equilibrium of an existing crack may be judged from the intensity of elastic stress around the crack tip. It has become a common practice to investigate interlaminar cracks using the critical strain energy release rate, G_c. This quantity is measurable in experiments. The energy approach is based on a thermodynamic criterion for fracture by considering the energy available for crack growth. For an elastic deformation, the unloading curve would return to the origin when the load is released. Before the crack starts to grow, the load reaches the pick (Figure 2.7). Once the crack starts growing at any intervals, the load-displacement curve can be approximated with a straight line (Adams et al., 2003). An elastic potential for a cracked body may be defined as

$$H = W - U \tag{2.1}$$

where W is the work supplied by the movement of the external forces, and U is the elastic strain energy stored in the body. If G_c is the work required to create a unit crack area, the criteria for crack growth can be formulated as,

$$\delta H \geq G_c \delta A \tag{2.2}$$

where δA is the increase in crack area.

At the critical condition, the energy supplied is equal to the energy required to grow the crack; i.e.,

$$\delta H = G_c \delta A \tag{2.3}$$

At the unstable equilibrium condition, the net energy supplied is greater than the required crack growth energy,

$$\delta H > G_c \delta A \tag{2.4}$$

The strain energy release rate, G, can be defined as

$$G = \frac{\delta H}{\delta A} \tag{2.5}$$

Now, for a linearly elastic body containing a crack of original length, a. Figure 2.7 shows the load, *P*, vs. the displacement, *u*, for the cracked body, where the crack growth is assumed to occur at a constant displacement (fixed grip).

In a fixed-grip case, the work term (*W*) vanishes and

$$\delta U = \frac{u\delta P}{2} = \text{area OAA} \tag{2.6}$$

Note that δP is negative because of the loss in stiffness followed by crack extension, and *G* is

$$G = \frac{\delta U}{\delta A} = -\frac{u}{2}\frac{\delta P}{\delta A} \tag{2.7}$$

For a linearly elastic body, the load-displacement relation can be written as

$$P = u/C \tag{2.8}$$

where *C* is the compliance of the specimen. Combination of Eqs. (2.7) and (2.8) gives

$$G = \frac{u^2}{2C^2}\frac{\delta C}{\delta A} = \frac{P^2}{2}\frac{\delta C}{\delta A} \tag{2.9}$$

It can be observed from Figure 2.7 that for any consecutive points on the load-displacement curve, the mode I critical energy release rate can be obtained as

$$G_{IC} = \frac{P_A u_B - P_B u_A}{2W\delta A} \tag{2.10}$$

where P_A and P_B are loads at point *A* and *B*, respectively; u_A and u_B displacements corresponding to the loads P_A and P_B, respectively, W is the width of the specimen, ΔA is the cracked surface. In the case of relatively high crack growth rate, it is inaccurate and inefficient to record the transient crack growth history. The following formula can be used to calculate the average energy release rate (Kevin and Roderick, 1993)

$$G_{IC} = \frac{\int_0^{\delta_c} P(u)du - \frac{1}{2}P_c u_c}{W\Delta a} \tag{2.11}$$

where P_c and u_c are respectively the load and displacement at the point of separation of the flanges, W is the specimen width, and Δa is the crack increment. The expression of G_{IC} can also be derived from the elementary beam theory. The expression of G_{IC} from the elementary beam theory can be also expressed excluding the vertical deflection u. That is, expressing G_{IC} as functions of load P and specimen parameters only. In the elementary beam theory, the specimens are considered as two identical cantilever Euler-Bernoulli beams with built-in ends.

a. Critical strain energy release rate based on the elementary beam theory (ASTM D5528)

$$G_I^{BT} = \frac{12P^2}{E_1 b^2 h^3} a^2 \tag{2.12}$$

where, E_1 is the longitudinal modulus (in the fiber direction), P is the maximum applied load at crack extension, *h* is the cantilever beam thickness, *b* is the specimen width, *a* is the crack length.

b. Critical strain energy release rate based on the transverse shear deformation theory (Daniel & Ishai, 2006)

$$G_I^{SH} = \frac{12P^2}{E_1 b^2}\left[\left(\frac{a}{h}\right)^2 + \frac{1}{10}\left(\frac{E_1}{G_{13}}\right)\right] \tag{2.13}$$

where, G_{13} is the transverse shear modulus.

c. Critical strain energy release rate based on corrected beam theory with consideration of transverse shear deformation and crack tip singularity (Hashemi et al., 1990)

$$G_I^{\chi} = 12\frac{P^2(a+\chi_I h)^2}{b^2 E_1 h^3} \tag{2.14}$$

where the expression for the correction factor χ_I is,

$$\chi_I = \sqrt{\frac{a_{66}}{18K(a_{11})}}\sqrt{3 - 2\left(\frac{\Gamma}{\Gamma+1}\right)^2} \tag{2.15}$$

$\Gamma = 1.18\frac{a_{66}}{\sqrt{a_{11}a_{33}}}$,$a_{11} = 1/E_1$,$a_{33} = 1/E_3$, $a_{66} = 1/G_{13}$ and K is a function of Poisson's ratio.

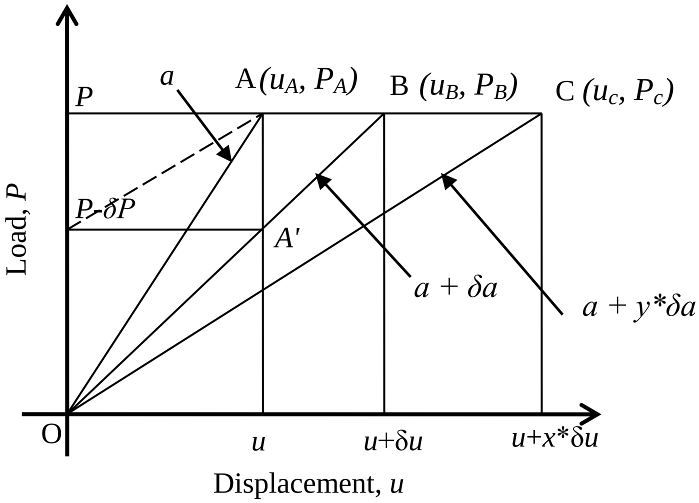

Figure 2.7. Schematic load-displacement behavior for a cracked body at crack lengths a and *a* + δ*a*.

2.6. Statistical reliability analysis of fracture energy release rate

To examine the nanofiber toughening effect in terms of critical strain energy release rate due to crack growth, the scattered data obtained from the tests can be organized using the reliability theory (Wu and Dzenis, 2005). The survival probabilities for the energy release rate can be obtained using a median rank formula,

$$f(x) = 1 - \frac{i-0.3}{n+0.4} \tag{2.16}$$

where i is the i-th specimen for n number of specimens in the increasing fracture energy release rate sequence. The critical strain energy release rate of the laminates can be assumed to follow two or three–parameter Weibull distribution. For example, the two-parameter Weibull distribution can be expressed as

$$P(\sigma) = exp\left[-\left(\frac{\sigma}{\sigma_0}\right)^m\right] \tag{2.17}$$

The mean value can be determined by

$$\bar{\sigma} = \sigma_0\left[\Gamma(1+\frac{1}{m})\right] \tag{2.18}$$

where σ_0 and m are the scale and shape parameters of the Weibull distribution and these parameters can be obtained by the maximum-likelihood estimation theory. $\Gamma(\ )$ is the Γ-function defined by

$$\Gamma(s) = \int_0^\infty x^{s-1}\exp(-x)\,dx. \qquad (s > 0) \tag{2.19}$$

2.7. Concept of self-repairing composites

Composites [e.g., carbon-fiber reinforced plastics (CFRP), fiberglass plastics, etc.] have been extensively used in aerospace, marine and ground vehicles. As discussed in Section 2.1, in spite of having many favorable properties, composite materials are questioned for their unavoidable process induced defects. Interfacial mismatches such as the differences in Poisson’s ratios and moduli of the matrices and fillers are responsible for the micro cracks within a short time of the service. For example, it was reported that the failure of the recent X-33 composite fuel tank was attributed to microcracking of the polymer composite parts (Grimsley, 2001). One of the most crucial issues in design of this type of components is to develop durable, lightweight, reuseable and cryogenic propellant tanks. Some advanced techniques have been under intensive investigation including autonomous/self-repairing polymeric composites (Dry, 1992 & 1996; Brown et al. 2003). Investigations have been conducted by a number of researchers all over the world to fabricate composites with instantaneous repairing function. The most promising proof-of-concept self-repairing composites are based on inclusion of healing-agent loaded microcapsules or hollow microfibers inside the matrix resin (Dry, 1992 & 1996; Brown et al. 2003). Hereafter, we briefly discuss the existing self-repairing techniques and related self-repair mechanisms. In the case of self-repairing composites, if crack initiates, the crack front can be arrested by the healing agent. In this section, a brief review is made on the state-of-the-art work on self-repairing polymers and laminated composites.

2.7.1. Self-repairing techniques

Self-repairing composites can be obtained simply by producing the composites with healing-agent loaded matrix resin, where healing of defects in matrix can be done intrinsically or extrinsically. The intrinsic self-repairing composite is an autonomic healing system without external intervention like the elastic memory polymer (EMC) (Dry, 1994). It enables crack healing under certain stimulation, mostly heating. A 50% recovery of impact strength can be obtained for thermoplastic polymers (Motuku et al., 1999); both physical interaction (Bleay et al., 2001) and chemical interaction (Brown et al., 2003) cause these healing mechanisms. Either thermosetting or thermoplastic polymers can be healed though heating the damaged polymers. Crack healing happens at or above the glass transition temperature and the chemical interactions recombine the broken molecules. In the extrinsic self-repairing case, healing agents are pre-embedded inside the matrix. In this case, healing agents should be encapsulated and embedded into the materials in advance. Two types of vessels have been explored. One method is based on healing-agent loaded hollow glass fibers and the other is based on healing-agent loaded microcapsules. The applicability of hollow glass fibers (Figure 2.8) were first introduced by Dry (1994 & 1996). During the process, the brittle thin-walled vessels are filled with polymerizable medium. Meanwhile, Motuku et al. (1999) used the same approach for the study of self-repairing composites. It needs to be mentioned that both Dry and Motuku utilized the hollow fibers (tubes) with the diameter much larger than that of the reinforcing fibers in composites. In such approach, the hollow glass fibers containing healing agent may act as the initiator responsible for the failure of composites, thus it is unsuitable to use hollow glass fibers with the diameter in millimeters. Later Bleay et al. (2001), Pang and Bond (2005a & 2005b) used a hollow fibers with the diameter much smaller (micro scale) than that used by Dry or Motuku. They used vacuum-assisted capillary-action filling technique to fill the healing agent into the hollow tubes. Furthermore, Trask et al. (2006 & 2007) and Williams et al. in 2007 considered incorporating layers of self-repairing hollow glass fibers into glass-fiber/epoxy and carbon-fiber/epoxy composites. Their experiments indicated that a significant amount of strength restoration can be achieved. In their research, a hollowness of 50% with the fiber diameter ranging from 30-100 μm has been tested.

On the other hand, healing agent loaded microcapsules for use in self-repairing composites have been investigated extensively by researchers. This self-repairing technique is similar to that based on hollow fibers; the difference is that the fragile microcapsule is used as container of the healing agent. Although the microencapsulated approach has yielded high healing efficiencies in several controlled material systems, the number of possible healing events is limited by the delivery of healing agent in the capsules. Furthermore, to address the technical issues of self-repairing composites, the initial focus is to utilize brittle thermosetting materials, for example epoxy, vinyl ester, etc. So far, two efficient catalysts, i.e. Grubbs' catalyst and tungsten hexachloride catalysts, have been explored for healing epoxy-based composites (White et al., 2001; Kamphaus et al., 2008). Use of Grubbs' catalyst was also successful for vinyl ester matrix (Figure 2.9). Figure 2.10 shows a tree diagram of several techniques for effective self-repairing scheme where for extrinsic healing system, either one part or two part resins can be placed inside the polymer matrix (Toohey et al. 2009 & Hansen et al. 2009).

2.7.2. Self-repairing chemistry

Ring-opening metathesis polymerization (ROMP) of dicyclopentadiene ($C_{10}H_{12}$) in the presence of Grubb's catalyst is the latest healing chemistry in the self-repairing of composite polymers. Mouldin et al. (2007) tested a tapered double cantilever beam (TDCB) for both endo-isomer and exo-stereoisomer of dicyclopentadiene and found that exo-stereoisomer has the self-repairing kinetics superior to that of the endo-isomer. They also found that by using healing agents with short gel times such as exo-dicyclopentadiene (DCPD), the healing time can be fast enough to repair the damage shortly after cracks appear. Because faster healing kinetics is important to arrest fatigue damage under extreme conditions by quickly healing rapidly propagating cracks. Thus, for many self-repairing applications, it is desirable to have the fastest healing kinetics possible as long as the quality of the repair is not compromised.

As mentioned earlier, self-repairing highly depends upon the polymerization of healing agent on the crack surface. Thus, the self-repairing materials should possess a long shelf life, low monomer viscosity and volatility, rapid polymerization capacity and low shrinkage upon polymerization (Andersson, 2007). One needs to be careful in selecting the type of healing agent to ensure the aforementioned properties. Self-repairing is a complex problem that involves monomer transport, mixing, catalyst dissolution, and catalyst transport in addition to healing polymerization, so it is necessary to have the fastest healing kinetics without compromising the quality of repair. The fast-reacting exo-DCPD leads to rapid gelation and insufficient time to completely dissolve the embedded Grubbs' catalyst. Jones et al. (2006) showed that complete dissolution of Grubbs' catalyst occurs in the range of 5–10 min. This dissolution rate is acceptable for self-repairing purpose based on endo-DCPD, which gels in approximately 20 min at room temperature. For exo-DCPD, which gels in seconds, much of the catalyst remains undissolved and a largely heterogeneous poly-DCPD film is formed on the crack plane. They also found that the healing efficiency was constant after an endo DCPD: exo DCPD isomer ratio of 60:40 containing 5wt% first-generation lyophilized Grubbs' catalyst.

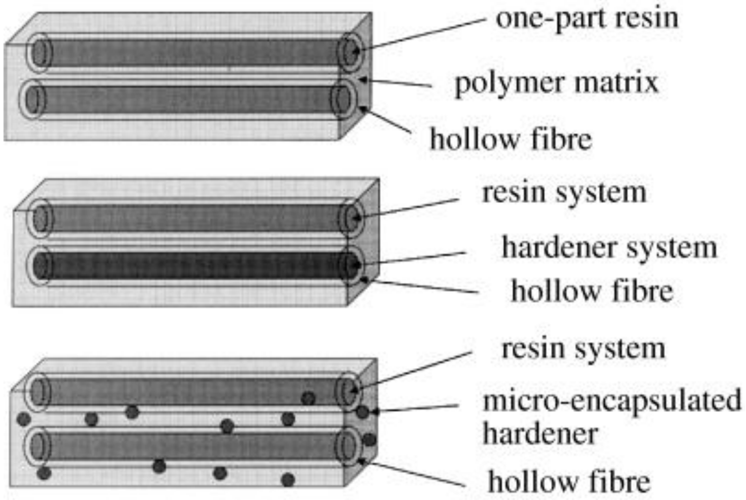

Figure 2.8. Schematic diagram of self-repairing concept for polymer matrix composites based on pre-embedded hollow tubes (Bleay et al., 2001).

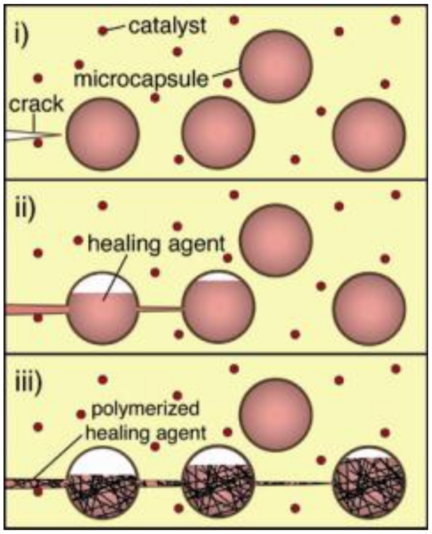

Figure 2.9. Schematic drawing of the principle of self-repairing epoxy based laminates with epoxy loaded microcapsules and latent hardener (White et al., 2001).

2.8. Outstanding problem to be resolved

With consideration of the studies on self-repairing composites performed by Dry (1992) to Mangun et al. (2010), we can find that several proof-of-concept healing systems such as single part or dual part adhesive have been successfully formulated. For single part adhesive, one type of resin like epoxy is used; for dual part resin, epoxy and its curing agent are filled and placed near to each other. Selection of the matrix polymer to fill the hollow glass fibers is critically important. As a matter of fact, if the hollow fibers do not break once the matrix fails, the entire self-repairing process will go in vain. To control the fracture mode, it is needed to reduce the thickness of hollow fiber and selection of appropriate fiber type. Also, the microcapsules and large diameter hollow tubes can produce voids inside the material when they are broken and their mechanical properties are usually lower than the matrix resin and the reinforcing fibers. This can noticeably reduce the global mechanical properties of the composites. This outstanding problem can be resolved by producing hollow fibers down to nanoscale such as core-shell nanofibers (Sun et al. 2003). Figure 2.11 shows an experimental setup of coelectrospinning, which can be used to produce core-shell nanofibers for filling healing agent in this research.

As nanofibers carry higher mechanical properties compared to those of conventional fibers, they can simultaneously toughen the matrix and bridge the crack surfaces. In addition, core-shell nanofibers can seal the crack by releasing the healing agent when they are broken. Figure 2.12 shows the core-shell nanofibers produced by means of coelectrospinning technique.

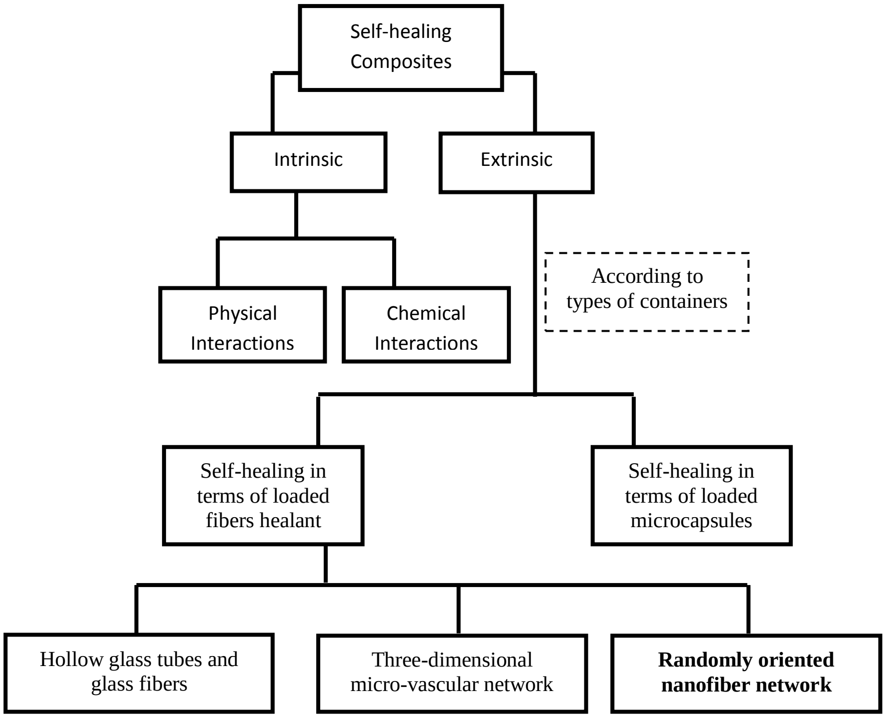

Figure 2.10. Tree diagram of self-repairing schemes.

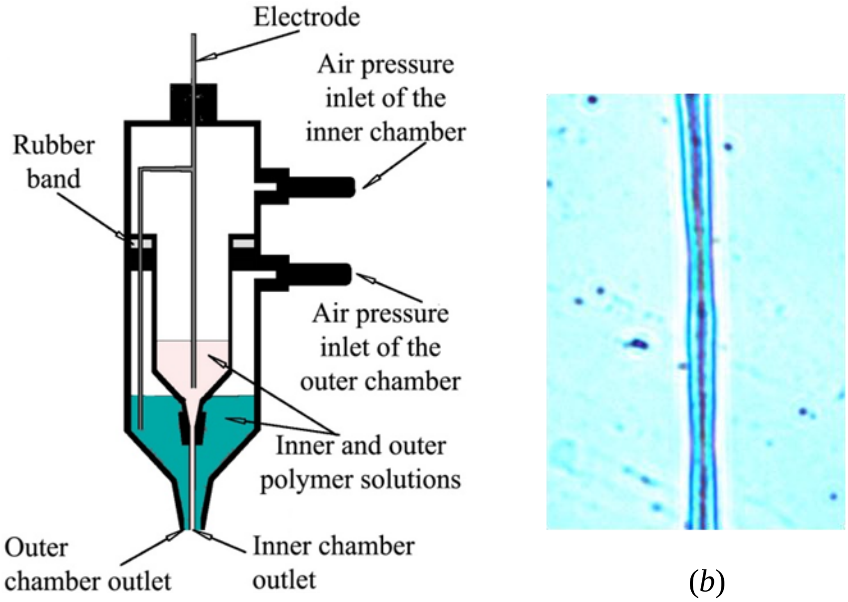

(*b*)

(*a*)

Figure 2.11. Core-shell nanofibers (PAN/DCPD). (*a*) Schematic coelectrospinning setup (Sun et al. 2003), and (*b*) presents the core-shell PAN-NF with DCPD as core material (Z. Zhou, Dr. Wu’s Group at NDSU).

CHAPTER 3. THEORETICAL UNDERSTANDING OF INTERLAMINAR MECHANICAL PROPERTIES OF HYBRID MULTISCALE COMPOSITES

Delamination is one of the common failure modes in advanced composites due to the weak interface bonding and severe interlaminar stress state. To achieve a high interlaminar strength property, the resin-rich interlayers in composite laminates can be modified with ultrathin fibers such as electrospun nanofibers. Composite laminates reinforced with fibers with multiscale diameters are called as hybrid multiscale polymer composites (for details see Section 2.3). In this chapter, a theoretical approach was formulated to investigate the mechanical properties of these hybrid multiscale composites. The influence of interlaminar properties with varying geometrical and material parameters was considered. Both shear and flexural strengths of these novel structural multiscale nanocomposite beams were investigated within the framework of the classical laminate theory with modified beam formulas.

3.1. Introduction

From the recent experimental study, it has been evidenced that the high interlaminar mechanical properties such as interlaminar shear strength and fracture toughness can be achieved via modifying the resin-rich interlaminar region with nanomaterials such as carbon-nanofibers (CNFs) (Chen et al., 2011 & 2012), CNTs (Sager et al., 2011), etc.

In most of the cases, data reductions of these composites are performed using isotropic beam formulas. Results based on isotropic beam formulas are on the conservative side and can be used for materials screening purposes (Rosselli & Santare, 1997). However, for the purpose of design of composites, these results can be further refined (Whitney & Browning, 1985). Specifically, when one of the constituents of the composites carry superior mechanical properties, it is desirable to formulate suitable formulas for accurate determination of the stress and strength of these composite materials. Such effort can be performed via the modification of the existing formulas. Classical laminate theory can give better results, however it has its limitations. For example, in classical laminate theory the transverse shear deformation is neglected (Whitney & Pagano, 1970; Berthelot, 1999). Consideration of shear deformation (first-order or higher-order) will result in more accurate results (Reddy, 1984; Auricchio & Sacco, 2003; Nguyen et al., 2008).

3.2. Motivation and objectives for this study

Our recent collaborative works with Professor Hao Fong’s group at the South Dakota School of Mines and Technology, Rapid City, SD (Chen et al., 2011 & 2012) have showed that incorporation of electrospun nanofiber (ENF) mats in carbon-fiber/epoxy composites can noticeably improve the mechanical properties (flexural and shear strength). It was found that, due to the interlaminar nanoreinforcement (ENF) the flexural and shear strengths were improved respectively 37.43% and 47.8%.

Theoretically, the thicker the nanolayer, the better the structural performance of the composites is. Yet, no experimental evidence has been reported. In experiment, the thickness of nanofiber interlayers can be tuned via adjusting the nanofiber deposition time in the electrospinning process. Thus, it is desirable to investigate the optimal deposition time of the nanofibers to maximize the global mechanical properties of the targeted hybrid multiscale composites. Recent experimental study (Chen et al. 2012) has demonstrated that an optimal nanofiber collection time does exist such that the mechanical properties of the resulting hybrid composites can be maximized. Herein, the nanofiber collection time is defined as the time period for collecting electrospun PAN copolymer (precursor) nanofibers on the CF fabrics. Several nanofiber collection times have been selected between 0 and 20 min to examine the thickness effect of the interlayer on the mechanical properties of the resulting hybrid composites. The experimental results showed that when the collection time was 10 min, the flexural strength, work of fracture, interlaminar shear strength and elastic modulus of the corresponding hybrid composites reach the maxima. The experimental results also motivated us to explore the theoretical understanding of mechanical properties of such hybrid multiscale composites. In this study, mechanical characterization of hybrid multiscale laminated composites and derivation of the stress formulas along the depth of a composite beam section were discussed. A piecewise layered-beam model was formulated for the prediction of the mechanical properties of hybrid multiscale composite beams. Finally, numerical experiments were performed to examine the influence of interlaminar geometrical (thickness) and strength (elastic modulus) parameters on the global mechanical properties (flexural and shear strength properties) of the hybrid multiscale composites.

3.3. Characterization of structural nanocomposites

In general, the stress state of any point in a beam consists of normal and shear stress components. In an isotropic beam, this stress variation across the beam thickness is continuous. In a laminated composite, the out-of-plane stress is usually discontinuous at the interfaces. The lamina configuration can be tailored to change the location of the maximum stresses (normal or shear) (Mallick, 1993). The actual stress distribution of a hybrid multiscale composite can be approached within the framework of classic laminate theory.

3. 3.1. Three-point bending testing of laminated beams

This is a special case of the two-dimensional (2D) laminate theory (APPENDIX A). In the case of a beam subjected to pure bending, only the moment about X-axis exists. The corresponding moment-curvature relation is (Agarwal & Broutman, 1980, p-316):

$$\begin{bmatrix} -\frac{\partial^2 w}{\partial x^2} \\ -\frac{\partial^2 w}{\partial y^2} \\ -2\frac{\partial^2 w}{\partial x \partial y} \end{bmatrix} = \begin{bmatrix} D_{11}^* M_x \\ D_{12}^* M_x \\ D_{16}^* M_x \end{bmatrix} \tag{3.1}$$

where D_{ij}^* are elements of the inverse matrix of D_{ij}, namely the bending stiffness matrix.

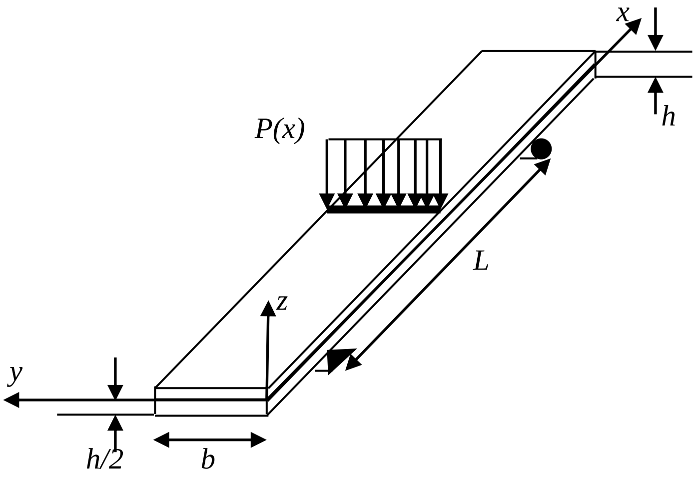

Figure 3.1. Schematic of geometries and loads of three-point bending test.

In the current case, the deflection is independent of *y*, i.e. for an accurate prediction, D_{12}^* effect (the width effect) needs to be considered. However, if the length of the beam is much larger than the width i.e. $L >> b$, the effect of width can be neglected

(Whitney, 1987). Also, the anisotropic shear coupling D_{16}^* can severely affect the result if neglected. Thus, in order to achieve a reliable prediction of results, the *L*/*b* ratio should be high (Figure 3.1). Furthermore, by considering the bending only about *x*-axis in Eq. (3.1), we have

$$-\frac{\partial^2 w}{\partial x^2} = D_{11}^* M_x \tag{3.2}$$

If a high *L/b* ratio is assumed, the deflection *w* can be expressed as *w*= *w*(*x*), a function only with respect to *x*, so Eq. (3.2) is reduced to

$$-\frac{d^2 w}{dx^2} = D_{11}^* M_x$$

or,

$$\frac{d^2 w}{dx^2} = -D_{11}^* M_x \tag{3.3}$$

The above relation can be further reduced as

$$\frac{d^2 w}{dx^2} = -\frac{M}{E_x^b I} \tag{3.4}$$

where $I = \frac{bh^3}{12}$ and $M = bM_x$ and $E_x^b = \frac{12}{h^3 D_{11}^*}$. For a symmetric beam containing isotropic layers or specially orthotropic layers, the effective bending stiffness can be obtained by the following relation (Gay et al., 2003):

$$E_x^b I = \sum_{k=1}^{n} E_x^k I^k \tag{3.5}$$

where E_x^k is the longitudinal modulus of the *k*-th layer and I^k is the moment of inertia of the *k*-th layer with respect to the midplane. In the limiting case where the effective modulus of the laminate E_x^b is replaced by *E*, the classical beam theory can be recovered from Eq. (3.4). In the case of a three-point bending beam, after integrating Eq. (3.4) to satisfy the boundary conditions (BCs), the effective modulus E_x^b can be expressed in terms of the mid-span deflection (w_c):

$$E_x^b = \frac{PL^3}{4bh^3w_c} \tag{3.5}$$

Furthermore, if no body force is assumed, force equilibrium [APPENDIX A Eq. (A-18)] of a differential body element yields,

$$\frac{\partial M_x}{\partial x} + \frac{\partial M_{xy}}{\partial y} - Q_x = 0 \tag{3.6}$$

With consideration of M_{xy}=0 and the shear force Q=bQ_x (Q_x varies along x-axis), we have

$$Q = \frac{dM}{dx} \tag{3.7}$$

The above equation is similar to the one developed in the classic elementary beam theory of homogeneous, isotropically elastic material as expected because this is simply a statement of equilibrium between the bending and transverse shear resultant.

3.3.2. The normal and shear stresses in different lamina (Whitney, 1987)

The normal stress for a particular lamina in x-direction can be obtained from Eq. A-25 (APPENDIX A):

$$\sigma_{xx}^k = z(Q_{11}^k D_{11}^* \quad Q_{12}^k D_{12}^* \quad Q_{16}^k D_{16}^*)M_x$$

or,

$$\sigma_{xx}^k = z\, a_{xx}^k \frac{M_x}{I} \tag{3.8}$$

where

$$a_{xx}^k = (Q_{11}^k D_{11}^* \quad Q_{12}^k D_{12}^* \quad Q_{16}^k D_{16}^*) * I \tag{3.9}$$

Q_{ij} are the stiffness components obtained from the original stiffness matrix (C_{ij}). If the thickness of the ply is *t* then, $I = \frac{t^3}{12}$. Variation of the shear stress along *y*-direction can be neglected as it can be assumed to be constant, i.e. $\frac{\partial \tau_{yx}^k}{\partial y} = 0$, thus,

$$\frac{\partial \sigma_{xx}^k}{\partial x} + \frac{\partial \tau_{zx}^k}{\partial z} = 0$$

or,

$$\frac{\partial \tau_{zx}^k}{\partial z} = -\frac{\partial \sigma_{xx}^k}{\partial x} \tag{3.10}$$

As the stress variation is along *x* and *z*-direction only, it reads

$$\frac{d\tau_{zx}^k}{dz} = -\frac{d\sigma_{xx}^k}{dx} \tag{3.11}$$

Combination fo Eqs. (3.11) and (3.8) yields

$$\frac{d\tau_{zx}^k}{dz} = -\frac{d\sigma_{xx}^k}{dx}$$

or,
$$\frac{d\tau_{zx}^k}{dz} = -z a_{xx}^k \frac{1}{I*b} \frac{dM_x}{dx}$$

or,
$$\frac{d\tau_{zx}^k}{dz} = -z a_{xx}^k \frac{1}{I} \frac{Q}{b} \tag{3.12}$$

Integrating above equation leads to

$$\tau_{zx}^k = -\frac{Q}{2Ib} * a_{xx}^k * (z^2 + c_k) \tag{3.13}$$

By applying the BCs at $z = \pm\frac{h}{2}, \tau_{zx}^k = 0$, constant c_k in Eq. (3.13) can be determined such that $c_k = -\left(\frac{h}{2}\right)^2$. Thus, Eq. (3.13) can be rewritten as

$$\tau_{zx}^k(z) = -\frac{Q}{2Ib} * a_{xx}^k * \left[z^2 - \left(\frac{h}{2}\right)^2\right] \tag{3.14}$$

Eq. (3.14) is similar to that of classic Euler-Bernoulli beam theory and it also satisfies the stress condition of a single ply laminate (beam theory). However, in the case of multiply laminates, it is needed to calculate the constant c_k for each lamina. To calculate the c_k values for each lamina, in-plane stress continuity between neighboring plies can be assumed, i.e., the interlaminar shear stresses at the interfaces are the same:

$$\tau_{zx}^{k}(z_k) = \tau_{zx}^{k+1}(z_k) \tag{3.15}$$

Thus, from Eqs. (3.13) and (3.15) as the *Q*/2*Ib* is constant, it can be yielded as

$$a_{xx}^{k+1}(z_{k+1}^2 + c_{k+1}) = a_{xx}^{k}(z_k^2 + c_k)$$

or,

$$c_{k+1} = \frac{a_{xx}^{k}}{a_{xx}^{k+1}}(z_k^2 + c_k) - z_{k+1}^2 \tag{3.16}$$

3.3.3. Short-beam shear test

In general, for the purpose of determining the flexural properties of composite laminates, three-point or four-point bending tests can be utilized though a variety of shear testing methods are available in the literature for measurement of either in-plane or transverse/out-of-plane shear properties. Due to its simplicity, short-beam shear test has been widely adopted though the results of short-beam shear test may not accurate for thin laminates (less than 10 plies) due to the local compressive failure near the loading points. The failure of short beams happens because of the combination of compression, crushing and shear stresses. To obtain better interlaminar results, it is the rule-of-thumb that composite laminates made of plies more than 50 layers are utilized to ensure the dominating interlaminar/transverse failure. The maximum shear stress can occur at a location *L*/4 from the supports. The below formula is commonly used for the data reduction of short-beam shear test:

$$\tau_s = 0.75\frac{P_m}{b\times h} \tag{3.17}$$

Furthermore, the short-beam shear test is performed for the purpose of determining the out-of-plane/interlaminar/transverse shear strength (τ_{xz}) but not for the in-plane shear strength(τ_{xy}). These two shear stresses have no fundamental difference in the case of isotropic beams. However, the out-of-plane shear stress dominates the catastrophic shear failure in short-beam shear tests, which is out-of-plane shear failure. Murthy (1981) stated that for composite laminates, the transverse shear stress calculation based on the classical laminate theory is inaccurate, and he proposed the modified formulas to improve the predictions. Yet, the required BCs in Murthy's work (1981) were not available. Detailed literature survey indicates that the accurate transverse shear stress based on short-beam shear tests is highly complicated.

3.3.4. Effect of laminate configuration in the experimental characterization of interlaminar shear strength

To date, relation (3.17) has been commonly used for data reduction of short-beam shear tests and also widely accepted by composites community to characterize the shear strength of composite materials (Mourtiz et al., 1997). Nevertheless, it needs to be cautious to adopt this relation for laminated composites since relation (3.17) does not take into account the effect of stacking sequence of the laminate. Specifically, for a cross-ply composite laminate which can be treated being made of orthotropic laminas, a modified shear strength relation for data reduction can be formulated within the framework of mechanics of composite materials (Chou, 1992; Berthelot, 1999; Vable, 2008). Consider a CFF/nanofiber-epoxy composite laminate being made of *n* layers of CFF (effectively isotropic). In this case, *n* should be an even number for the purpose of shear strength test.

The effective modulus, Poisson's ratio, and thickness of the composite laminate after curing are denoted as E_c, υ_c and t_c, respectively. The number of nanofiber layers (effectively isotropic) is n-1, and the corresponding effective modulus, Poisson's ratio, and thickness of the nanofiber layers are E_n, υ_n and t_n, respectively. Based on the composite beam theory and the shear-strength test configuration, the maximum shear stress at the mid-plane can be expressed (Chen et al. 2011) as:

$$\tau_s = \frac{Q_{comp}P_m/2}{b(\sum EI)} \tag{3.18}$$

In the above, P_m is the peak external force at the shear failure point; Q_{comp} is the first moment of the effective modulus of the upper half cross-section of the laminate, i.e. the cross-section with $z \geq 0$, defined as

$$Q_{comp} = \sum_{j=1}^{n/2} \frac{bE_c}{1-\nu_c^2}\frac{1}{2}[z_{c1}^2(j) - z_{c2}^2(j)] + \sum_{k=1}^{n/2} \frac{bE_n}{1-\nu_n^2}\frac{1}{2}[z_{n1}^2(k) - z_{n2}^2(k)] \tag{3.19}$$

ΣEI is the effective flexural rigidity of the entire composite laminate in plane strain defined as

$$\sum EI = \sum_{j=1}^{n} \frac{bE_c}{1-\nu_c^2}\frac{1}{3}[z_{c1}^3(j) - z_{c2}^3(j)] + \sum_{k=1}^{n-1} \frac{bE_n}{1-\nu_n^2}\frac{1}{3}[z_{n1}^3(k) - z_{n2}^3(k)] \tag{3.20}$$

In the above, $z_{c1}(j)$ and $z_{c2}(j)$ are the z-coordinates of the upper and lower surfaces of the j-th CF fabric layer, respectively, and $z_{n1}(k)$ and $z_{n2}(k)$ are the z-coordinates of the upper and lower surfaces of the k-th ENC layer of the upper half cross-section, respectively, except for the mid ENF layer with $z_{n2}(n/2)=0$. Furthermore, the maximum mid-span deflection of the composite laminate in shear strength test can be determined as

$$w_{max} = \frac{P_m L^3}{48(\sum EI)} \tag{3.21}$$

where L is the span between two pins in the shear strength test. Substitution of Eq. (3.21) into Eq. (3.18) leads to the shear strength of composite laminates:

$$\tau_s = 24\frac{Q_{comp}w_{max}}{bL^3}$$

$$= \frac{12w_{max}}{L^3}\left\{\sum_{j=1}^{\frac{n}{2}} \frac{bE_c}{1-\nu_c^2}\frac{1}{2}\left[z_{c1}^2(j) - z_{c2}^2(j)\right] + + \sum_{k=1}^{n/2} \frac{E_n}{1-\nu_n^2}\left[z_{n1}^2(k) - z_{n2}^2(k)\right]\right\} \quad (3.22)$$

Theoretically, relations (3.18) and (3.22) are equivalent within the framework of classic composite beam theory, each of which can be employed for experimental data reduction. However, for relation (3.18) or (3.22), one needs to know the effective moduli E_c and E_n and thicknesses t_c and t_n of the CF and ENF layers, respectively. With the consideration of the possible viscoelastic deformation normally detected in bending tests of polymer composites, relation (3.18) combined with (3.20) is preferred, which yields (Chen et al., 2011)

$$\tau_s = \frac{3P_m}{4b}\frac{\sum_{j=1}^{n/2}\frac{E_c}{1-\nu_c^2}\left[z_{c1}^2(j)-z_{c2}^2(j)\right]+\sum_{k=1}^{n/2}\frac{E_n}{1-\nu_n^2}\left[z_{n1}^2(k)-z_{n2}^2(k)\right]}{\sum_{j=1}^{n}\frac{bE_c}{1-\nu_c^2}\left[z_{c1}^3(j)-z_{c2}^3(j)\right]+\sum_{k=1}^{n-1}\frac{bE_n}{1-\nu_n^2}\left[z_{n1}^3(k)-z_{n2}^3(k)\right]} \quad (3.23)$$

It can be shown that in the limiting case of isotropic material, relation (3.23) can recover the case of isotropic materials as shown in relation (3.17). Furthermore, to examine the applicability of relation (3.17) in the present study, without loss of the generality, here only consider an ideal specimen model of two CF fabric layers with thickness h_c and one ENF interlayer with the thickness h_n, and further set $\upsilon_c \approx \upsilon_n$. Thus, relation (3.23) can be reduced to

$$\frac{\tau_s}{\frac{3P_m}{4b\times 2(h_c+h_m/2)}} = 1 + \frac{(\frac{E_n}{E_c}-1)\frac{h_c h_n^2}{2}}{2\left(h_c+\frac{h_n}{2}\right)^3+(\frac{E_n}{E_c}-1)\frac{h_n^3}{4}} \quad (3.24)$$

This relation gives the ratio of the shear strength based on the classic laminate theory to that based on the classic beam theory of isotropic material. For ENF reinforced CF-epoxy laminate, if selecting $E_c \approx E_n$, relation (3.24) shows that relation (3.17) gives largely acceptable interlaminar shear strength as expected. For CF-epoxy laminate, if replacing the E_n with the modulus of pure resin E_p ($E_c/E_p>20$), relation (3.24) shows that the interlaminar shear strength based on (3.17) for CF-epoxy laminates is slightly larger than the one given by (3.23). Therefore, the data reduction of the current composite laminates based on the approximate relation (3.17) does not significantly affect the results.

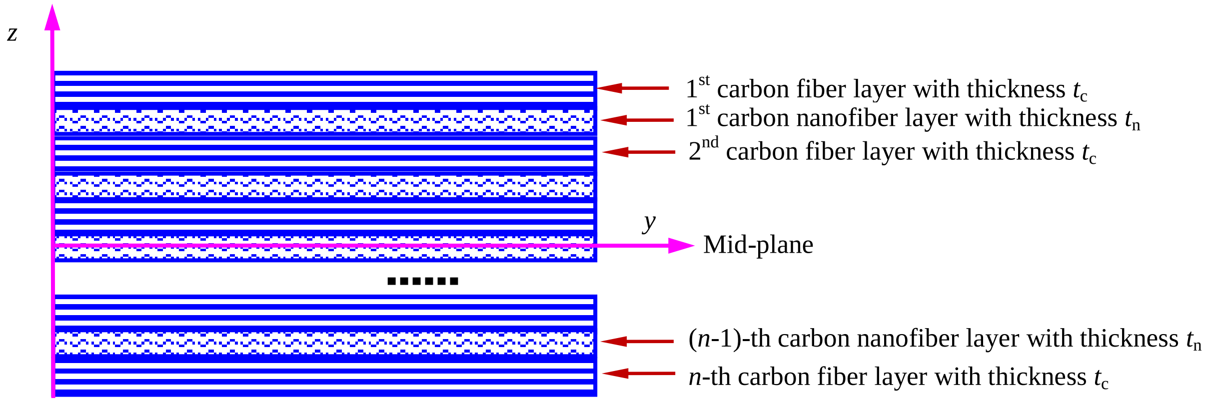

Figure 3.2. Schematic diagram of cross-section of a composite laminate reinforced with a nanofiber layer.

3.4. Numerical examples

3.4.1. Material properties

Table 3.1 tabulates the material properties of a UD carbon-fiber (modulus=222 GPa and Poisson's ratio=0.20)/epoxy (modulus=3.97 GPa and Poisson's ratio=0.35) composite laminate used for the present numerical study.

3.4.2. Beam dimensions

For the numerical analysis of a flexible composite beam, a six-ply laminate was considered. Both unmodified and nanofiber modified interfaces were considered. The dimensions of the flexural beam were 50.8 mm in length, 12.7 mm in width, and 1.6 mm in thickness with a clear span of 25.4 mm. The dimensions of the short beam were 8 mm in length, 4 mm in width, and 1.6 mm in thickness with a clear span of 6.4 mm.

Table 3.1. Properties of a UD carbon-fiber/ epoxy composite (Wu and Dzenis, 2005).

Fiber volume fraction, V_f	0.6
Density, ρ, g/cm^3	1.6
Longitudinal modulus, E_{11}, GPa	135
Transverse in-plane modulus , E_{22}, GPa	8.5
Transverse out-of-plane modulus, E_{33} GPa	8.5
In-plane shear modulus, G_{12}, GPa	4.7
Out-of-plane shear modulus, G_{13}, GPa	4.7
Major in-plane Poisson's ratio, ν_{12}	0.34
Out-of-plane Poisson's ratio, ν_{13}	0.34

3.4.3. Computational procedure

Step 1: Calculate a_{xx}^{k} based on Eq. (3.9) which is a lamina property (considering D_{12}^*, D_{16}^*).

Step 2: Using the top and bottom BCs calculates c_0 for the top surface.

Step 3: Calculate c_1 based on Eq. (3.16).

Step 4: Calculate c_2, c_3, c_4, c_5, c_6 (bottom).

Step 5: Calculate the transverse shear stress for each layer based on Eq. (3.13).

3.5. Results and discussions

3.5.1. Three-point bending test

3.5.1.1. Flexural stress calculation

The properties of individual laminas were calculated from the constituent properties for each fabric layer. For unmodified interlayers, the modulus ratio of the carbon fiber fabric (CFF) layer (E_c) to the isotropic matrix interlayer (E_n) is ~34 and the thickness of the matrix interlayer (t_n) was assumed as half of the CFF layer (t_c). On the other hand, for the nanofiber modified interlayers, the modulus of nanofiber modified interlayers was assumed as twice that of a CFF layer. Figure 3.3 shows the flexural stress variations for CFF-epoxy [Figure 3.3 (*a*)] and CFF/nanofiber-epoxy composites [Figure 3.3 (*b*)] along the depth of the beam at the middle section. It should be noted that the loads for the calculation were obtained from the experimental results (see Section 3.2). From the numerical results, it was observed that, both the classical laminate theory and the modified beam formulas give the same results (here only the classical laminate theory results are presented). Based on the theoretical predictions, it can be found that the normal stress in unmodified laminate at the matrix layer is much lower than that of the CFF layer and vice versa for nanofiber modified laminates. In practice, because of nanofiber bridging at the interfaces as well as the improved mechanical properties of the interlayers, the interfacial strength can be improved significantly.

3.5.1.2. Transverse shear stress calculation

Figure 3.4 shows the transverse shear stress variation along the depth/thickness of the beam. It can be observed that isotropic beam formula is independent of interlaminar material properties; also for the same material properties, the isotropic beam formula and piecewise beam formula give same result. However, Figure 3.4 (*b*) shows that when the interlayer property changes in a piecewise composite beam formula (Eq. 3.23), a significant variation in transverse shear stress can be observed.

3.5.2. Transverse shear stress in short beams

Figure 3.5 shows the shear stress distribution along the depth of the beam in the case of either CFF/epoxy or CFF/nanofiber/epoxy laminates under the same loading condition. It can be observed that there is 6.8% increase of the maximum shear stress in

CFF/nanofiber/epoxy laminate compared to the CFF/epoxy laminate. Also, the thickness of the interlayers can play an important role in the global mechanical properties of nanofiber modified composites. Figure 3.6 shows the effect of interlayer thickness for unmodified and nanofiber modified laminates. It can be seen that, for unmodified laminates, the shear strength is lower in the case of lower CFF layer thickness (h_c). On the other hand, for nanofiber modified laminates with the increasing carbon-fabric layer thickness (h_c), the shear strength value is decreased. This is because in nanofiber modified laminates, the interlaminar properties are higher than those of unmodified laminates based on only CFF layers.

3.6. Concluding remarks

A theoretical study was conducted to examine the effect of interlaminar nanoreinforcement in the novel hybrid multiscale composites. It was found that the shear and flexural strength are dependent of the interlayers. The interlaminar properties can be enhanced substantially with high stiffness and strength interlayers instead of simple pure resin interlayers that are formed in the composite processing. On the other hand, because nanofibers can interlock the adjacent laminas, they can potentially enhance the interlaminar fracture toughness. Furthermore, other physical properties (e.g. electrical, thermal properties, etc.) can be improved by modifying the interlayers with different nanomaterials. To investigate the interlaminar fracture properties of the multiscale composites, a differential experimental study has been conducted and will be discussed in the next chapter.

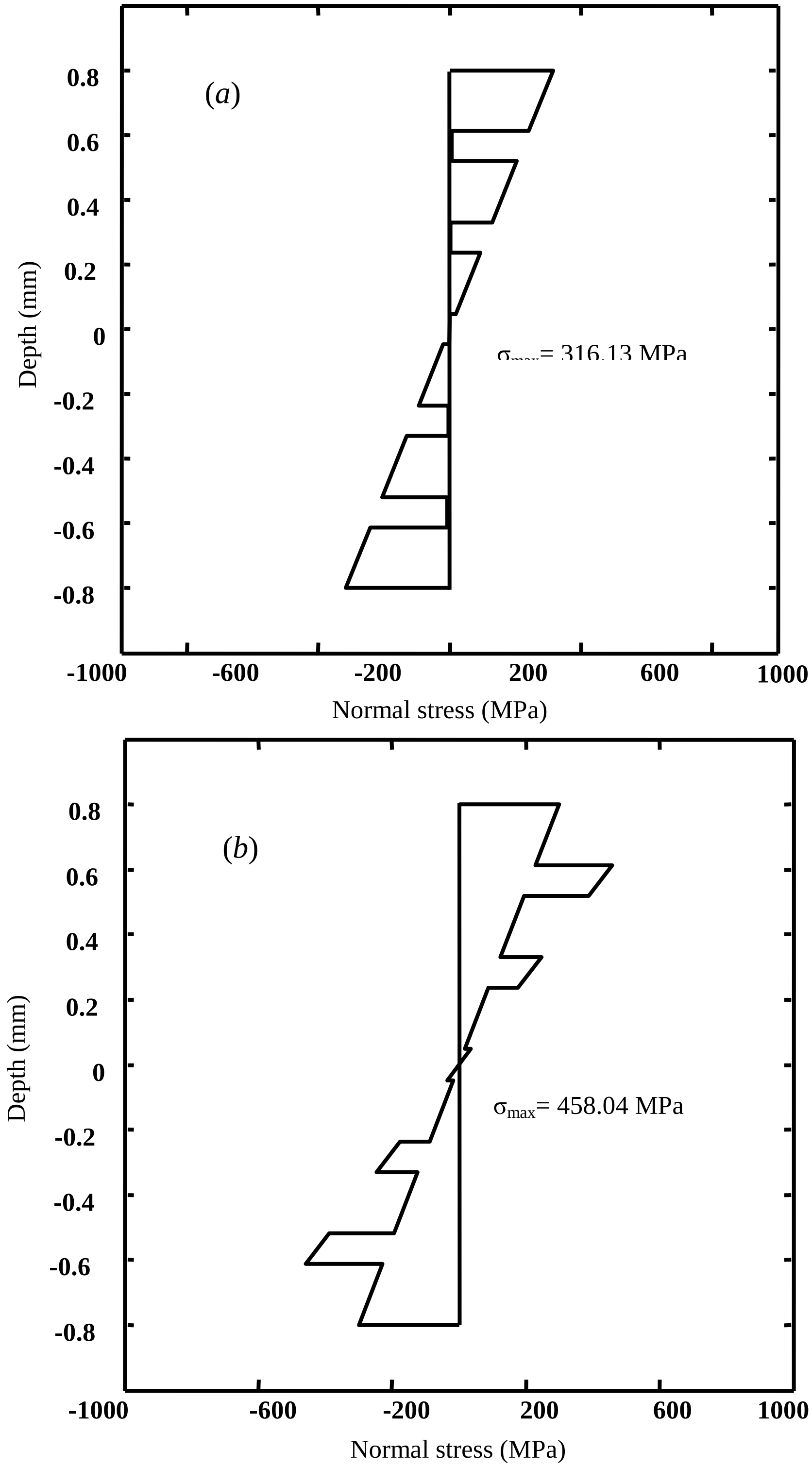

Figure 3.3. Normal stress distribution along the depth of the beam for the same loading condition. (*a*) CF-epoxy (E_c=34E_n and t_c=2t_n) (*b*) CF/ENF-epoxy (E_c=0.5E_n and t_c=2t_n).

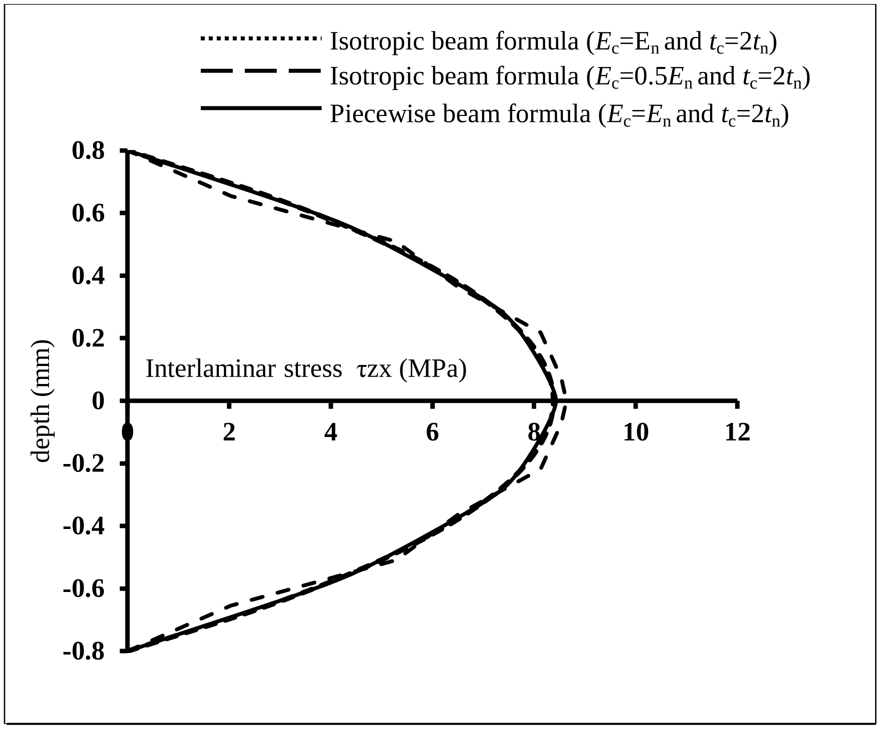

(*a*)

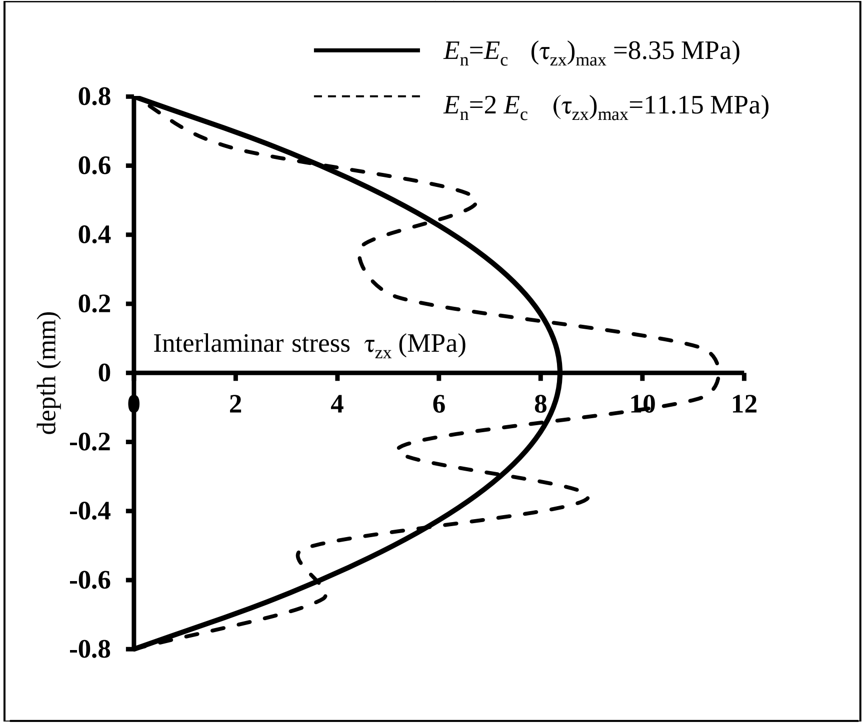

(*b*)

Figure 3.4. Interlaminar shear stress variation along the thickness direction (*a*) comparison of isotropic beam formula and piecewise beam formula (E_c=Modulus of CF layer, E_n=Modulus of interlayer, t_c=Thickness of CF layer, t_n=Thickness of interlayer) (*b*) comparison of piecewise beam formula with different interlaminar property.

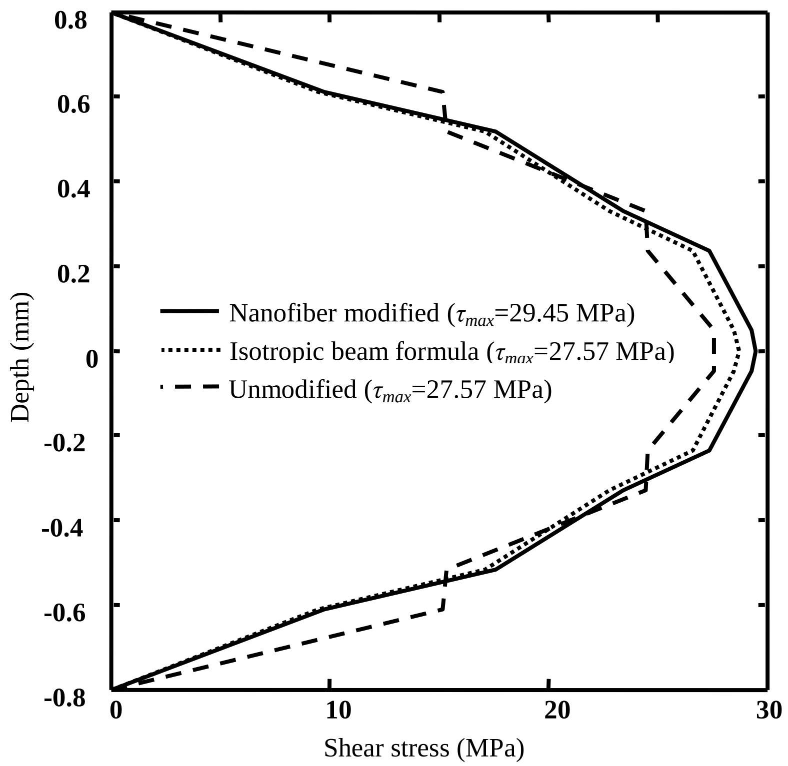

Figure 3.5. Shear stress distribution along the depth of the beam. CF-epoxy (E_c=34E_n and t_c=2t_n) and CF/ENF-epoxy (E_n=2E_c and t_c=2t_n).

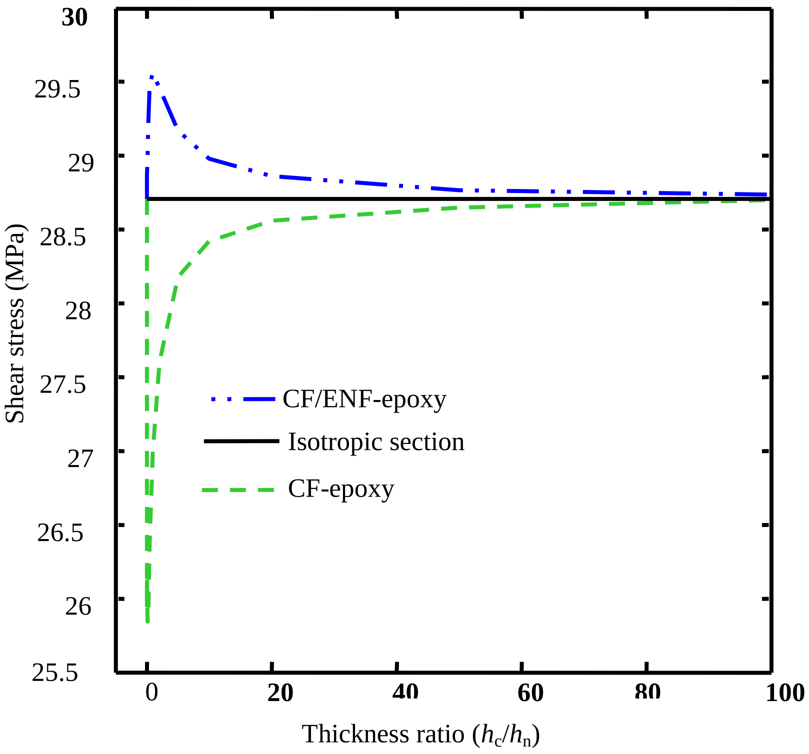

Figure 3.6. Influence of the interlayer thickness on shear stress of the section.

CHAPTER 4. CHARACTERIZATION OF INTERFACIAL TOUGHENING EFFECT IN CARBON-FIBER/EPOXY COMPOSITES REINFORCED WITH ELECTROSPUN NANOFIBERS AT INTERFACES

This chapter focuses on experimental characterization of the toughening effect of nanofiber interlayers on the interlaminar fracture toughness of carbon-fiber fabric (CFF)/epoxy composites. Two kinds of ultrathin nonwoven nanofiber interlayers [i.e. electrospun PAN nanofibers and electrospun PAN-based CNFs] were fabricated and inserted between neighboring CFFs prior to infusion of epoxy resin by VARTM technique. Mode-I interlaminar fracture (delamination) test was performed on the novel hybrid multiscale composite systems. Fractographical analysis of fractured composite samples was performed by means of scanning electron microscopy (SEM); the micro and nanoscale failure and toughening mechanisms at nanofiber-reinforced interfaces were explored.

4.1. Introduction

Laminated composites made of UD or woven fabrics are commonly used in structural applications. When the composite laminates are fabricated, ultrathin resin-rich interlayers with relatively low mechanical properties exist between laminas. These interlayers play an important role in the global performance of the composites, especially the out-of-plane mechanical properties. Compared to the reinforcing fibers, the polymeric matrices have much lower mechanical properties including strength, modulus, fracture toughness, etc. Also, due to the inhomogeneous architecture of the constituents, complicated stress state is induced when the composites are subjected to external stressing. Damages and cracking of various types are commonly triggered in the composite materials during their service life. It has been discussed in Chapter 3 that to improve the mechanical properties such as the flexural and shear strength, the weaker matrix layers can be modified with nanomaterials. In fact, interlaminar fracture is a severe and persistent problem in laminated composites (Dzenis, 2008). The interlaminar mechanical properties of these composites can be enhanced via incorporating various nanomaterials into the resin-rich interlayers. Among a variety of nanomaterials, polymer nanofibers, CNFs and CNTs have been tested in recent years (Wu, 2003; Chen et al., 2011; Sager et al., 2011). With the advancement of nanomanufacturing, polymer nanofibers, CNFs, CNTs have been produced efficiently and used as reinforcing phases to improve the mechanical properties of polymer composites. Most of the previous studies on interlaminar toughening based on polymer nanofibers were conducted on UD prepreg composites, and the improvement was around 20-50%.

In this chapter, a differential study of the toughening mechanisms of CFF/epoxy composites reinforced with electrospun nanofibers at ply surfaces was performed. Two types of composite systems reinforced with commercially available UD CFFs (UDCFFs) and woven CFFs (WCFFs) were produced, respectively. Two types of epoxy resin systems were utilized to examine the toughening mechanisms. Nanofiber mats with randomly oriented PAN nanofibers of diameter ~300 nm were produced by electrospinning; mats with randomly oriented CNFs were synthesized via carbonization of pre-stretched electrospun PAN nanofibers. The thickness of the nanofiber-modified interlayers was maintained approximately the same as the unmodified one, which was ~40 μm. SEM-based fractographical analysis was performed to examine the toughening mechanisms and a reliability model was introduced to analyze the experimental data.

4.2. Experimental

Fabrication and characterization of the laminated composite specimens include fabrication of PAN nanofibers and CNFs by electrospinning followed by carbonization, processing of novel hybrid multiscale composites by means of wet lay-up followed by VARTM technique , and evaluation of the toughening effect in the novel composites by the mode I interlaminar fracture test followed by detailed SEM-based fractographical analysis.

4.2.1. Preparation of nanofiber mats

PAN-nanofiber films were prepared by means of the low-cost, top-down electrospinning technique. CNF fabrics were produced by carbonization of pre-stretched electrospun PAN-nanofibers with the diameter ~200-400 nm. These nanofiber films were utilized as the nano-sized reinforcement for the development of the novel hybrid multiscale composites in this study.

Electrospinning is generally regarded as one of the most promising techniques of producing continuous ultrathin fibers. By means of electrospinning, ultrathin continuous fibers with the diameters in the range less than fifty nanometers to over one micrometer can be produced (Theron et al., 2001; Yarin et al., 2001). Figure 4.1 (*a*) shows a schematic setup of single needle-based electrospinning. In the electrospinning process, a sufficiently high DC voltage is applied to a liquid droplet. When the electric field reaches the threshold value, a thin jet ejects from the meniscus surface. The uniqueness and advantages of the electrospinning process include that: (1) the nanofibers can be readily sandwiched between the CFFs; (2) nanofiber mats can be prepared and placed between the plies during manufacturing; and (3) since the electrospun nanofibers are randomly oriented, the distribution of nanofibers between the laminas in the resulting multiscale composites can be quite uniform. In this study, the CNF mats that were synthesized via carbonization of pre-stretched electrospun PAN nanofibers were supplied by Professor Hao Fong’s group at the South Dakota School of Mines and Technology (Rapid City, SD).

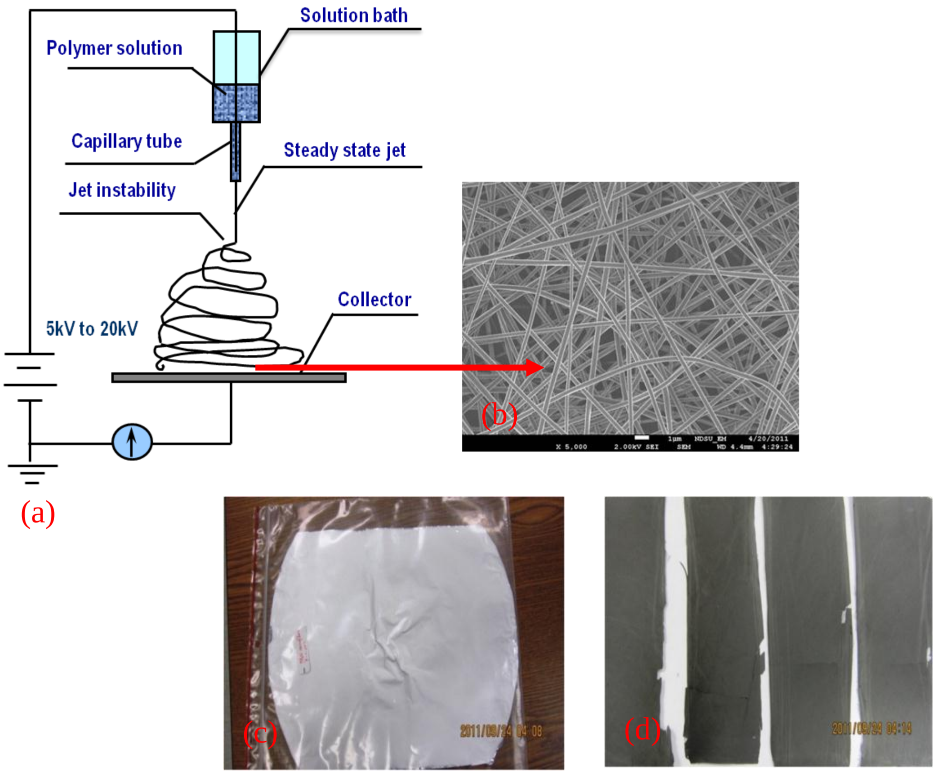

Figure 4.1. Nanofiber mat fabrication. (*a*) Schematic of electrospinning setup (Wu, 2003), (*b*) PAN nanofiber network (SEM image), (*c*) and (*d*) photographs of PAN nanofibers & CNFs.

4.2.2. Composite manufacturing and characterization

During the process, UDCFFs (9.0 oz/yd^2) and WCFFs (5.7 oz/yd^2) were purchased from Fibre Glast Development Corp. (Brookville, OH). SC-15 epoxy resin and corresponding hardener, and Epon 862 epoxy resin and Epicure 3234 curing agent were selected as the polymeric matrix for producing the novel polymer composites. The SC-15 resin system was purchased from the Applied Poleramic Inc. (Benicia, CA). Epon 862 and Epicure 3234 were purchased from Miller-Stephenson Chemical Company, Inc. (Morton Grove, IL). The mix ratio of the SC-15 epoxy resin versus the hardener was 100/30 by weight, while the mix ratio of Epon 862 to Epicure 3234 were 100/14 by weight.

SC-15 is a low viscosity two-part toughened epoxy resin system. Part A of the SC-15 resin is composed of diglycidylether of bisphenl A (60-70%), aliphatic diglycidylether (10-20%), and epoxy toughener (10-20%). Part B of the SC-15 is the hardener with cycloaliphatic amine (70-90%) and polyoxylalkyamine (10-30%). This specially developed resin system has been widely used for VARTM processes. Typical physical and mechanical properties of the SC-15 resin system are listed in Table 4.1 (APPENDIX B for details). Epon 862 is a very low molecular weight difunctional bisphnol-F epoxide (diglycidyl ether of bisphenol-F) and Epicure 3234 is an aromatic tetramine (Triethylenetetramine). Typical physical and mechanical properties of the Epon 862 and Epicure 3234 epoxy resin system are listed in Table 4.2.

Table 4.1. Physical and mechanical properties of SC-15 epoxy resin.

Viscosity @ 77^oF (cP)	Cured density (oz/in^3)	Tensile elontation (%)	T_g (wet) (^oF)	Tensile strength (ksi)	Tensile modulus (msi)	Energy release rate (G_{ic}) (in-lb/in^2)	Fracture toughness (K_{Ic}) (psi-in$^{.5}$)
300	0.63	6	220	9.0	3.8	5.65	1400

Table 4.2. Physical and mechanical properties of Epon 862 and Epicure 3234 epoxy resin system (Source: www.resins.com).

Viscosity @ 77^oF (cP)	Pot life (hr)	Tensile elongation (%)	Glass transition temperature T_g (^oF)	Tensile modulus (ksi)
700-900	0.5-1	7-8	230-248	450-490

For the UDCFF reinforced composites, the laminate panels were simply produced by 12 layers of UDCFF laminas. In contrast, during the fabrication of the WCFF reinforced composites, five layers of UDCFFs were placed on both sides of intermediate four layers of woven fabrics. The involvement of UDCFFs was to enhance the flexural stiffness of the laminates and to avoid large flexural deformation of the arms near the crack tip during mode I interlaminar fracture test based on double cantilever beam (DCB) specimens. It was observed in our initial tests that DCB tests based on pure cross-ply CFF/epoxy laminates resulted in significant flexural damage near the crack tip. In addition, Teflon^{TM} film was placed at the middle layer of the composite laminate to create an artificial crack with the length around 50 mm after pre-cracking. Wet lay-up followed by VARTM technique was used for the laminate manufacturing (Figure 4.2). Usually, laminates prepared by VARTM technique has one surface (the surface in contact with the mold) relatively coarser than the other. The large surface coarseness may lead to stress concentration and therefore localized bending damage in delamination test. In interlaminar fracture tests, the two arms of the DCB specimens should be maintained to carry the same stiffness. Thus, both the top and bottom surfaces should be smooth. To ensure the flanges with the same stiffness value, an aluminum plate was placed on the top surface of the fabric panel during resin infusion. After a couple of troubleshoots of the specimen preparation, the whole processing procedure was fixed. Figure 4.3 shows the photographs of the final process steps adopted in this study. In the first step, CFFs, breather material, release films, vacuum bag, and Teflon films were cut with their appropriate dimensions. In the second step, releasing agent was coated on the glass mold surface after cleaning with acetone. Then, a releasing film was placed on the surface, infusion media was placed surrounding the panel area [Figure 4.3 (*b*)]. In the third step, epoxy resin and the hardener were mixed and the resin system was then used for the wet lay-up process [Figure 4.3 (*c*)]. Nanofiber mat and Teflon films (12.7 μm thin) were placed on the middle layer of the laminate [Figure 4.3 (*d*) & (*e*)]. In the final step, the entire area was sealed with tacky tape and vacuum bag [Figure 4.3 (*f*)].

Vacuum pressure of 27 mm Hg was maintained during the initial curing at room temperature for 24 hrs. The obtained composites were further cured in an oven before the fracture test. Laminates prepared with SC-15 resin was further post-cured in an oven for 6 hrs at 80^{o}C and laminates prepared with Epon 862 resin was post cured in an oven for 1 hr at 100^{o}C.

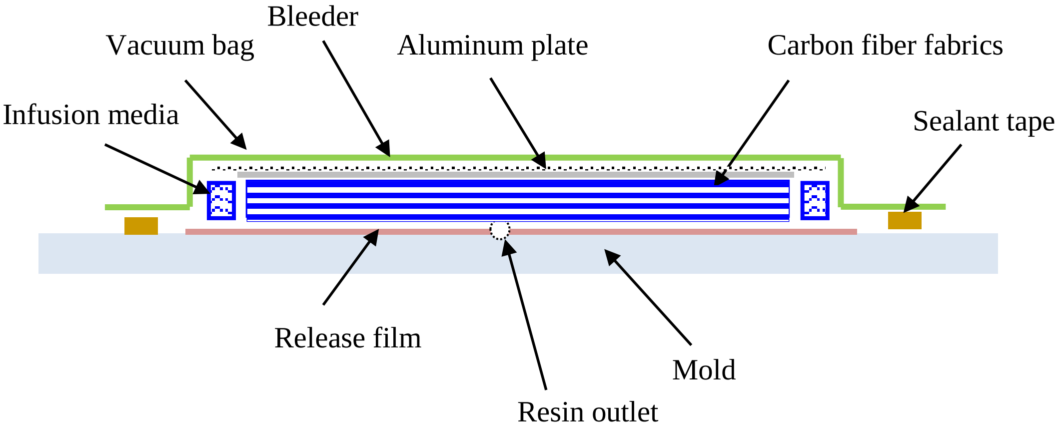

Figure 4.2. Schematic of vacuum assisted resin transfer molding (VARTM) method.

4.2.3. Specimen preparation

DCB specimens were cut from the laminates using a diamond-tipped rotary saw installed with a water-cooling system. Figure 4.4 shows a fracture specimen schematically (Dimensions: ~150 mm in length, ~22.5 mm in width, and ~4.0 mm in thickness). Door hinges were glued with the specimens with desired alignment. Two-part adhesive 907 purchased from Miller Stephenson was used to bond the hinges. Artificial pre-crack created by the Teflon film was then advanced using a screw driver (Figure 4.5).

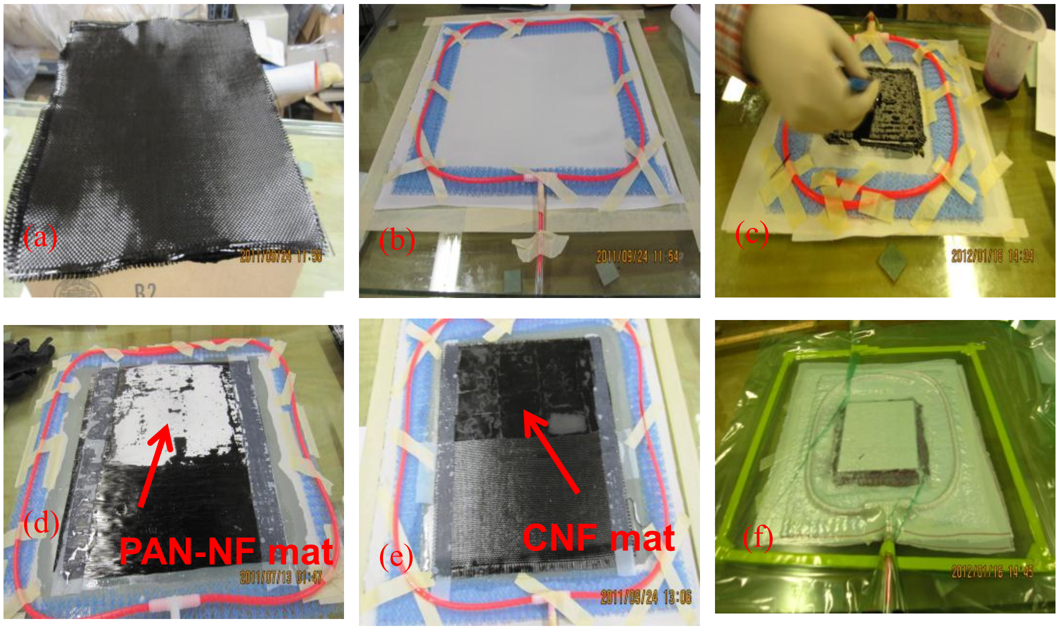

Figure 4.3. Photographic display of wet-layup and VARTM process steps.

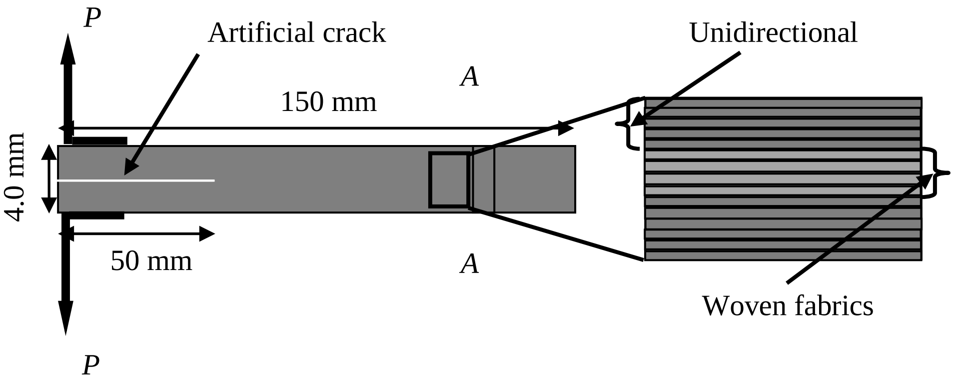

Figure 4.4. Schematic double cantilever beam (DCB) specimen for mode I interlaminar fracture test and cross-sectional configuration of the laminate specimen.

4.2.4. Mode I interlaminar fracture testing

Mode I interlaminar fracture properties of the novel hybrid multiscale composites were characterized at room temperature on a Satec Instron machine (Figure 4.6). Serrated wedge action grips were used for the specimen clamping. Special attention was practiced for the alignment of the specimens. The specimens were tested at a constant crosshead speed of 2 mm/min until the complete failure of the specimen. For the entire mode I interlaminar fracture tests, these test parameters were maintained constant.

From each test, a load-displacement curve can be obtained. Figure 4.7 shows a typical load-displacement diagram of the mode I interlaminar fracture test. As discussed in Chapter 2 (Section 2.5), the following formula is used to calculate the average energy release rate (Kevin and Roderick, 1993)

$$G_{IC} = \frac{\int_0^{\delta_c} P(\delta)d\delta - \frac{1}{2}P_c\delta_c}{W\Delta a} \tag{4.1}$$

where P_c and δ_c are respectively the load and displacement at the point of final failure of the DCB specimen, W is the specimen width, and Δa is the crack length during the test.

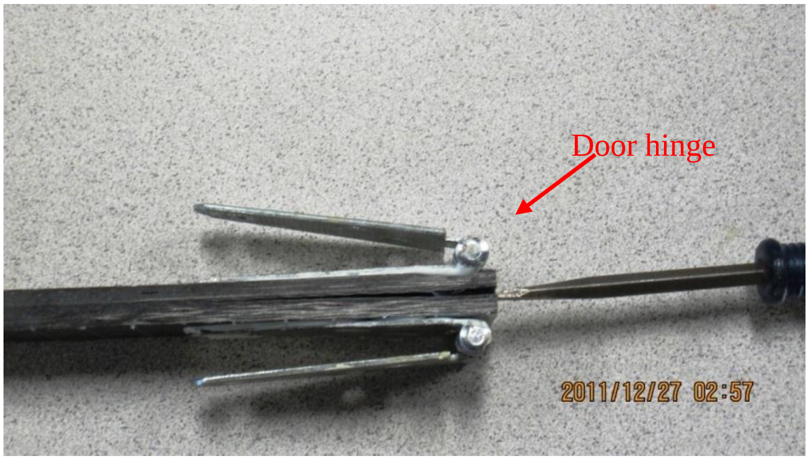

Figure 4.5. Gluing door hinges and advancement of artificial pre-crack.

4.3. Results and discussions

To investigate the toughening effect of PAN-nanofiber interlayers in laminated composites, mode-I interlaminar fracture tests were performed to obtain the quantitative toughening data. In addition, scanning electron microscope (SEM) was employed to examine the micro/nano-scaled morphologies, the distribution of nanofibers in the composites (particularly between the neighboring laminas), and the fracture surfaces to reveal the related toughening mechanisms.

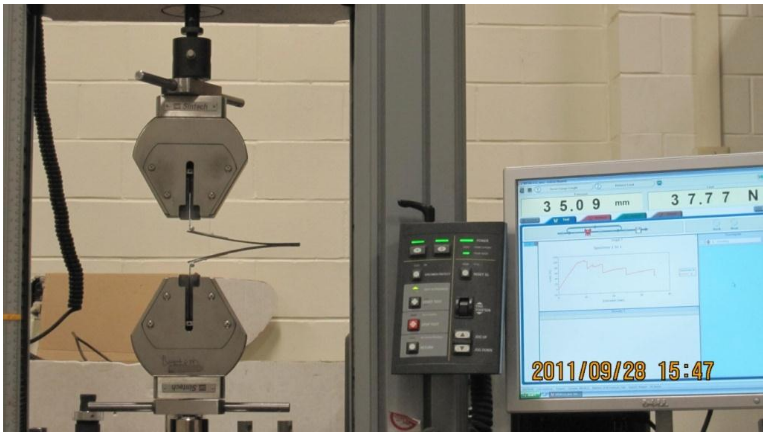

Figure 4.6. Double cantilever beam (DCB) mode I interlaminar fracture test setup.

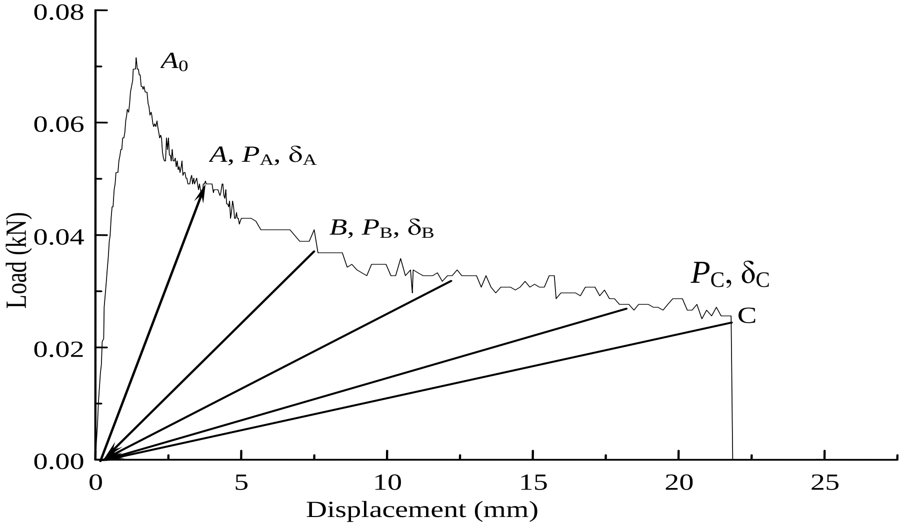

Figure 4.7. Schematic load-displacement diagram of mode I interlaminar fracture test (Wu, 2003).

4.3.1. PAN nanofiber modified UDCFF reinforced specimens

4.3.1.1. Experimental results

In this case, PAN nanofibers were used as interfacial reinforcement between the 6th and 7th plies of the twelve-ply laminate manufactured by UDCFF laminas. The procedure for specimen preparation and test parameters were the same as discussed in Sections 4.2.3 and 4.2.4. Figure 4.8 shows a schematic load-displacement diagram of mode I interlaminar fracture test of PAN nanofiber modified UDCFF reinforced specimens. The average mode I critical strain energy release rate (G_{IC}) of unmodified and modified specimens were calculated based on Eq. (4.1). Table 4.3 shows the critical strain energy release rates of unmodified and PAN nanofiber modified UDCFF composite specimens. It can be observed that the critical strain energy release rates are highly scattered. Thus, a two-parameter Weibull distribution model was used for data reduction to examine the nanofiber toughening effect in the sense of statistics. Figure 4.9 shows the variation of the survival probability vs. the strain energy release rate of the unmodified and modified specimens with a mean value of 1.892 kJ/m^2 and 1.395 kJ/m^2, respectively. As a conclusion, the mean strain energy release rate of PAN nanofiber modified samples was actually decreased 26.27 %, i.e. PAN nanofibers had no toughening effect in this case.

4.3.1.2. SEM fractographical analysis

Evaluation of the fracture surfaces of the specimens indicates that when mode I interlaminar fracture tests are performed, the PAN nanofiber modified specimens suppresses the high microfiber bridging (Figure 4.10). Due to the suppression of microfiber bridging, the strain energy release rate or fracture toughness of the modified specimens was decreased. Nevertheless, the present fracture test also explored the unique deformation and failure modes of plastic PAN nanofibers including nanofiber necking, rippling, plastic deformation, and so on (Figure 4.11). It needs to be mentioned that the unique nanofiber rippling has been also observed recently in single-nanofiber tension tests (Naraghi et al., 2007a, 2007b & 2009) and annealing of electrospun polyimide nanofibers (Wu et al., 2008). Wu et al. (2008) even developed a nanomechanics model to predict the condition and ripple wavelength of the rippling phenomenon in polymer nanofibers subjected to axial stretching.

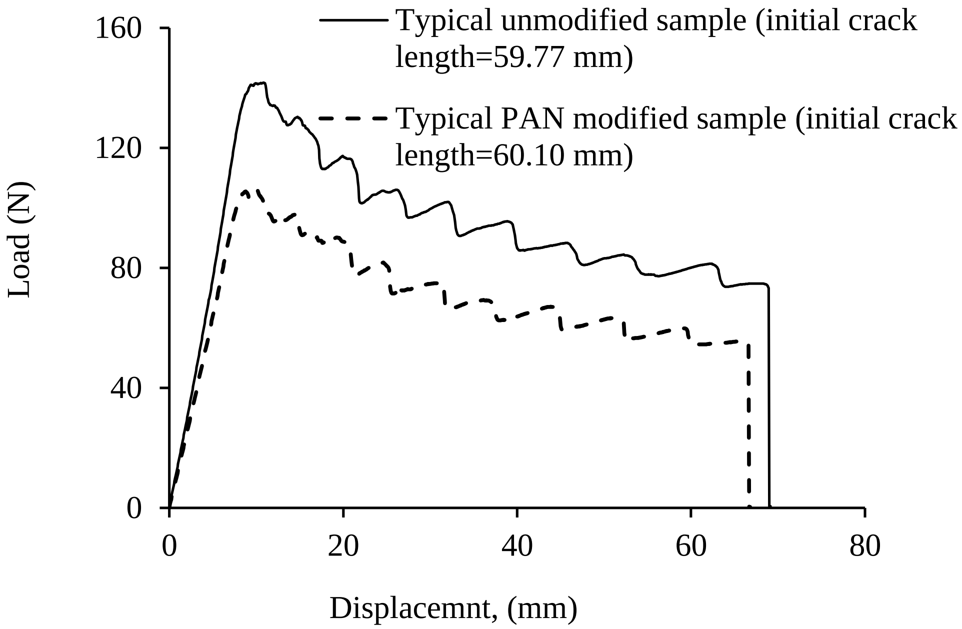

Figure 4.8. Load-displacement curves of mode I interlaminar fracture tests (UDCFF reinforced composites with SC-15 epoxy resin system).

4.3.2. PAN nanofiber modified WCFF reinforced specimens

Due to the suppression of microfiber bridging, no obvious interfacial toughening effect by the PAN nanofibers has been evidenced in the case of UDCFF reinforced composites. To eliminate the microfiber bridging effect for the purpose of differential study of the nanofiber toughening effect, WCFF reinforced composite was further taken into account to examine the potential interfacial toughening effect.

Table 4.3. Experimental results of strain energy release rate of unmodified and PAN-nanofibers modified UDCFF reinforced specimens (SC-15 epoxy resin system).

Sample no.	Mode I fracture strain energy release rate (G_{IC})	
	Unmodified specimens	PAN nanofiber modified specimens
1	1.498	1.188
2	1.720	1.201
3	1.789	1.267
4	1.842	1.315
5	1.863	1.364
6	1.870	1.429
7	1.873	1.439
8	1.892	1.466
9	1.895	1.515
10	1.904	1.522
11	1.969	1.553
12	2.004	1.603
13	2.006	1.612
14	2.008	1.728
15	2.066	1.761
16	2.069	1.802

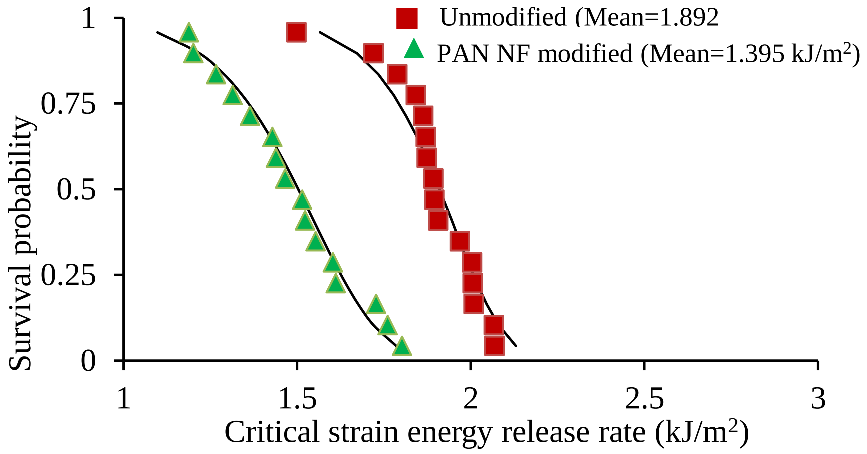

Figure 4.9. Variation of the survival probability vs. the critical strain energy release rate of unmodified and PAN nanofiber modified specimens (SC-15 epoxy resin system).

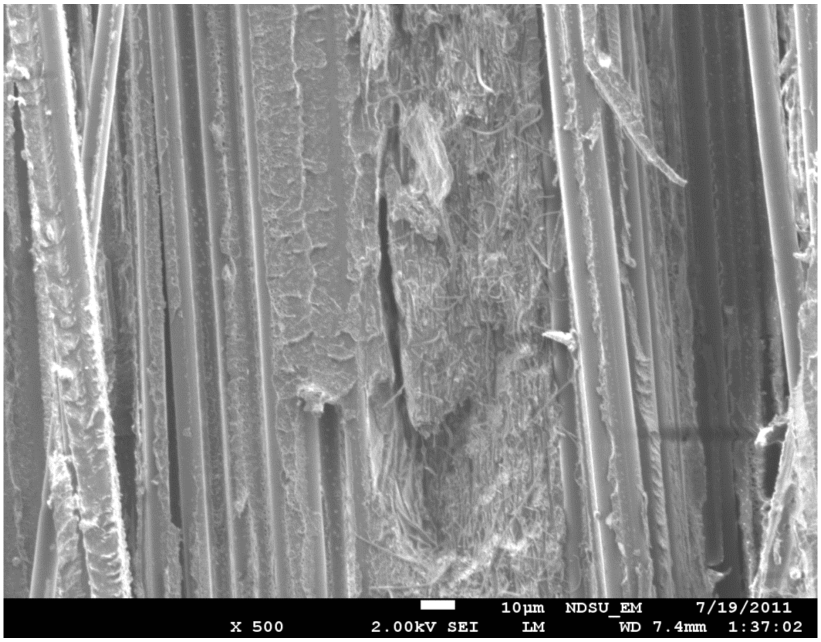

Figure 4.10. Suppression of high microfiber bridging due to the PAN nanofibers

4.3.2.1. Test results

In this case, PAN nanofibers were used as interfacial reinforcement between the 6th and 7th plies of the twelve-ply laminate made of WCFF laminas. The procedure for specimen preparation and test parameters were the same as discussed in Sections 4.2.3 and 4.2.4. Figure 4.13 shows a typical load-displacement diagram of mode I interlaminar fracture test of PAN nanofiber modified and unmodified WCFF reinforced specimens. The average strain energy release rate (G_{IC}) of unmodified and modified specimens were calculated using Eq. (4.1). In this case, scattered results were obtained for different laminates. Table 4.4 lists the critical strain energy release rate of unmodified and PAN nanofiber modified WCFF reinforced specimens. Table 4.4 shows that the difference of the critical strain energy release rate was very high. Thus, a two-parameter Weibull distribution model was further used for data reduction and examination of the nanofiber toughening effect statistically. Figure 4.14 shows variation of the survival probability vs.

the critical strain energy release rate of unmodified and modified specimens with a mean value of 0.524 kJ/m^2 and 0.416 kJ/m^2, respectively. In this case, the mean critical strain energy release rate of PAN nanofiber modified samples was decreased 20.61 %.

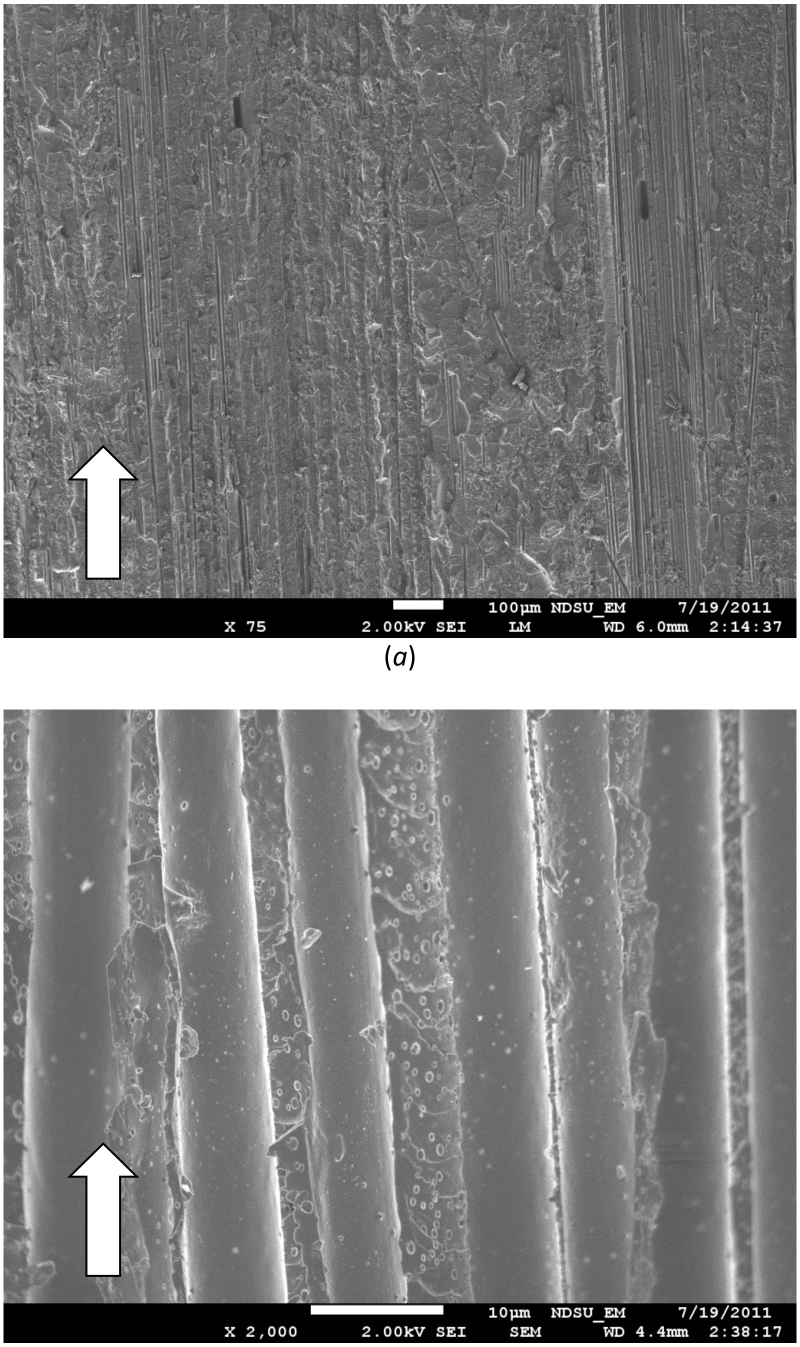

(*a*)

(*b*)

Figure 4.11. SEM fractographical analysis of fractured specimen surfaces of unmodified UDCFF reinforced laminate specimen (SC-15 epoxy resin system).

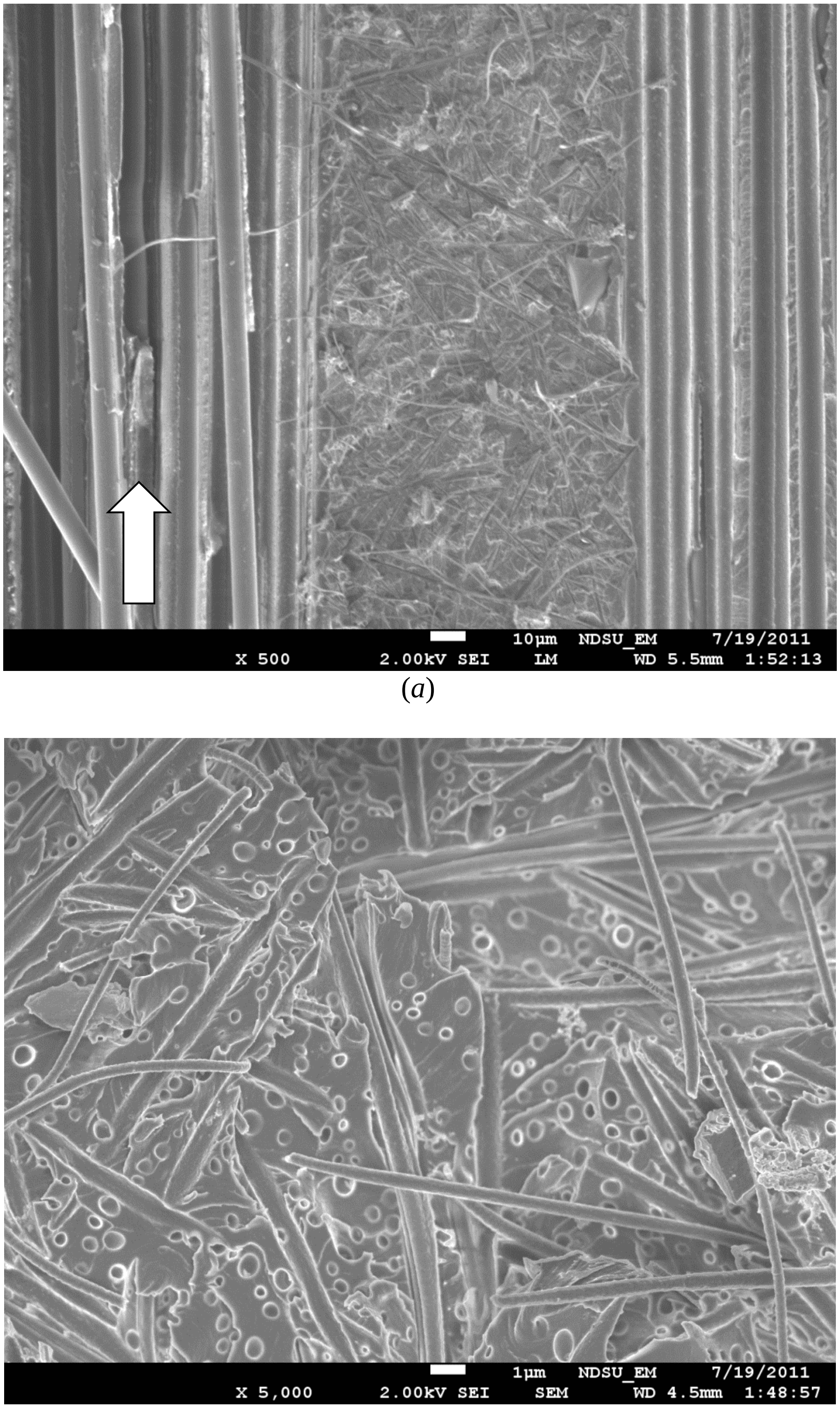

(*a*)

(*b*)

Figure 4.12. SEM fractographical analysis of fractured specimen surfaces of PAN nanofiber modified UDCFF reinforced laminate specimen (SC-15 epoxy resin system).

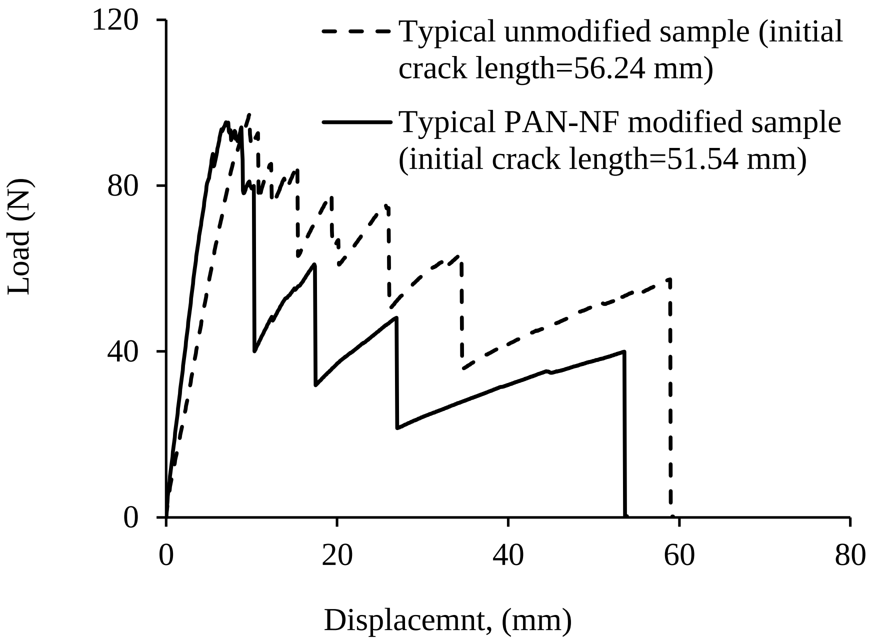

Figure 4.13. Typical load-displacement curves of mode I interlaminar fracture test (WCFF reinforced composites with SC-15 epoxy resin system).

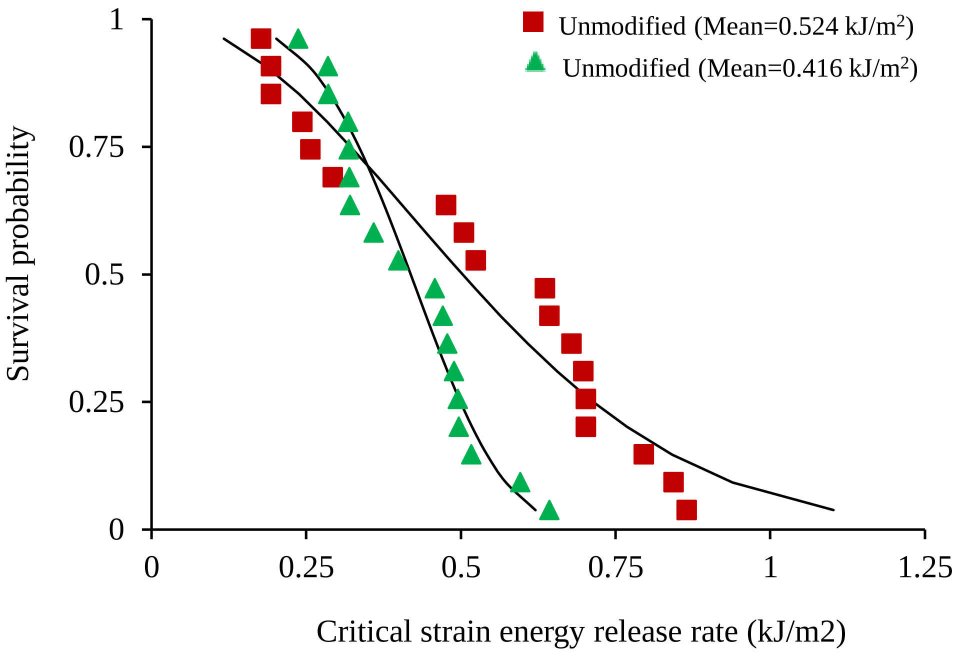

Figure 4.14. Variation of the survival probability vs. the critical strain energy release rate of unmodified and PAN nanofiber modified WCFF reinforced composite samples (SC-15 epoxy resin system).

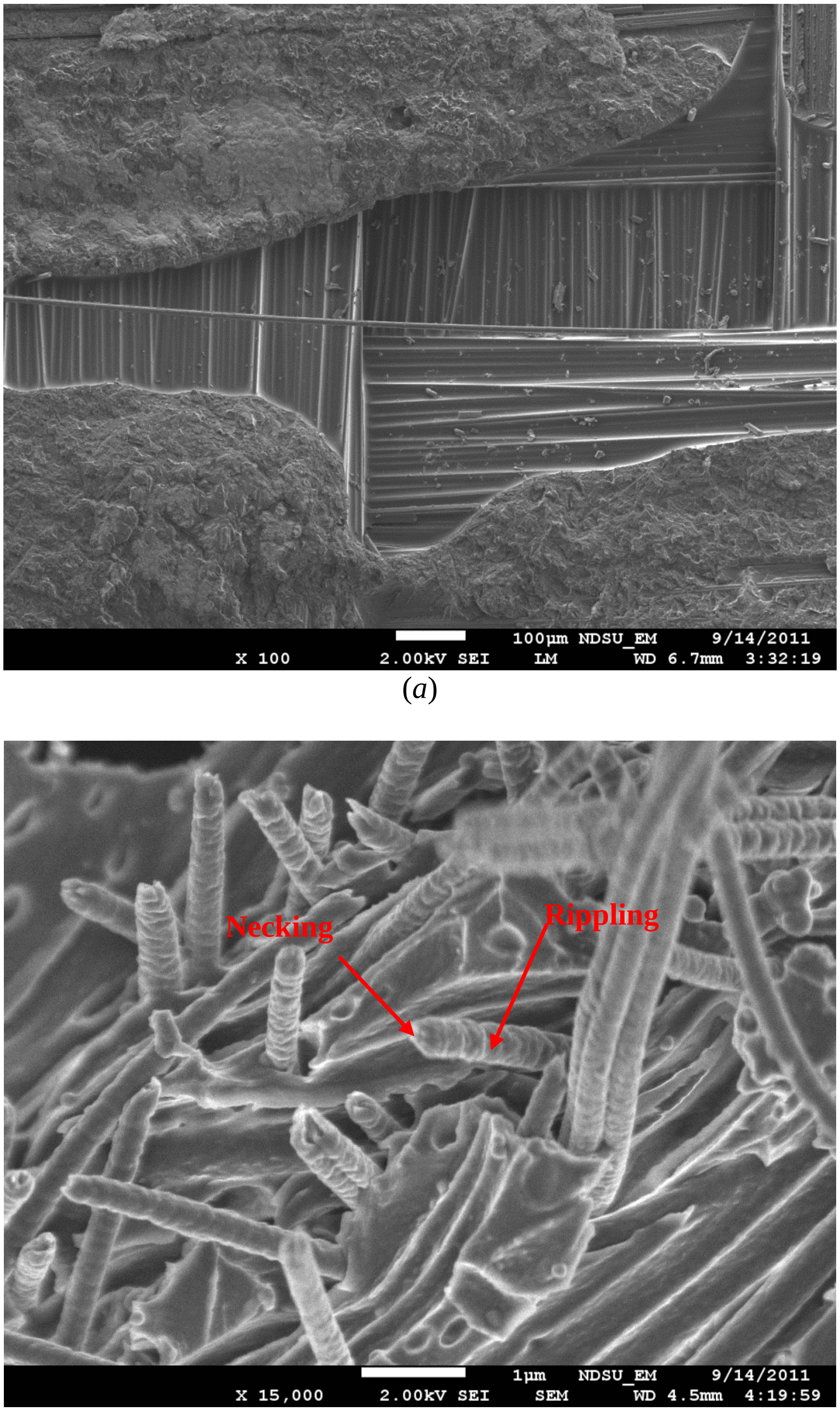

(*a*)

(*b*)

Figure 4.15. (*a*) Fracture surface of WCFF reinforced laminates and (*b*) rippling and necking of PAN nanofibers after pull-out (SC-15 epoxy resin system).

Table 4.4. Experimental results of the critical strain energy release rate of unmodified and PAN nanofiber modified WCFF reinforced specimens (SC-15 epoxy resin system).

Sample no.	Mode I fracture strain energy release rate (G_{IC})					
	Laminate panel 1		Laminate panel 2		Laminate panel 3	
	Unmodified	PAN-NF modified	Unmodified	PAN-NF modified	Unmodified	PAN-NF modified
1	0.177	0.285	0.476	0.237	0.698	0.359
2	0.193	0.286	0.505	0.319	0.702	0.478
3	0.193	0.318	0.524	0.32	0.702	0.489
4	0.244	0.321	0.636	0.399	0.796	0.497
5	0.257	0.471	0.643	0.458	0.844	0.517
6	0.293	0.495	0.679	0.643	0.865	0.596

4.3.3. CNF modified WCFF reinforced specimens

4.3.3.1. Experimental results

For CNF modified laminate specimens, the same fabrication and testing procedures were mandated as PAN nanofiber modified laminates. In this case, CNFs were used as interfacial reinforcement between the 6th and 7th plies of the twelve-ply laminate manufactured by WCFF laminas. Figure 4.16 shows a schematic load-displacement diagram of mode I interlaminar fracture test of CNF modified WCFF reinforced specimens. The average critical strain energy release rate (G_{IC}) of unmodified and modified specimens were calculated based on Eq. (4.1). In this case, also, scattered results were obtained for different laminates. Table 4.5 presents the critical strain energy release rate of unmodified and CNF modified WCFF reinforced specimens. Table 4.5 shows that the difference of the critical strain energy release rates was very high. Similarly, a two-parameter Weibull distribution model was again used for analysis of the experimental data. Figure 4.17 shows variations of the survival probability vs. the critical strain energy release rate of the unmodified and modified specimens with a mean value of 0.241kJ/m^2 and 0.202 kJ/m^2, respectively. As a result, the mean critical strain energy release rate of CNF modified samples was decreased 16.18 %, i.e. CNFs entangled at interfaces cannot enhance the interlaminar fracture toughness of resulting composite laminates

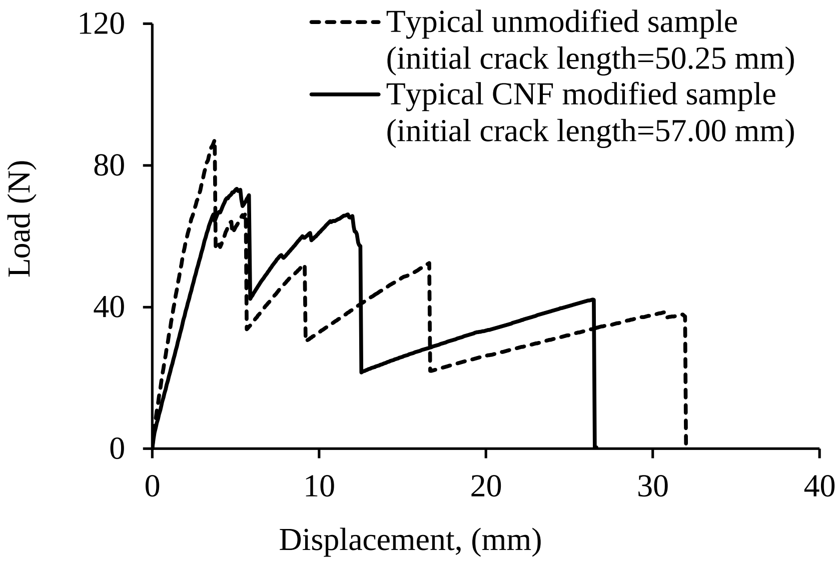

Figure 4.16. Typical load-displacement curves of mode I interlaminar fracture tests of CFF reinforced laminates with and without CNF modified interfaces (WCFF reinforced composites) (SC-15 epoxy resin system).

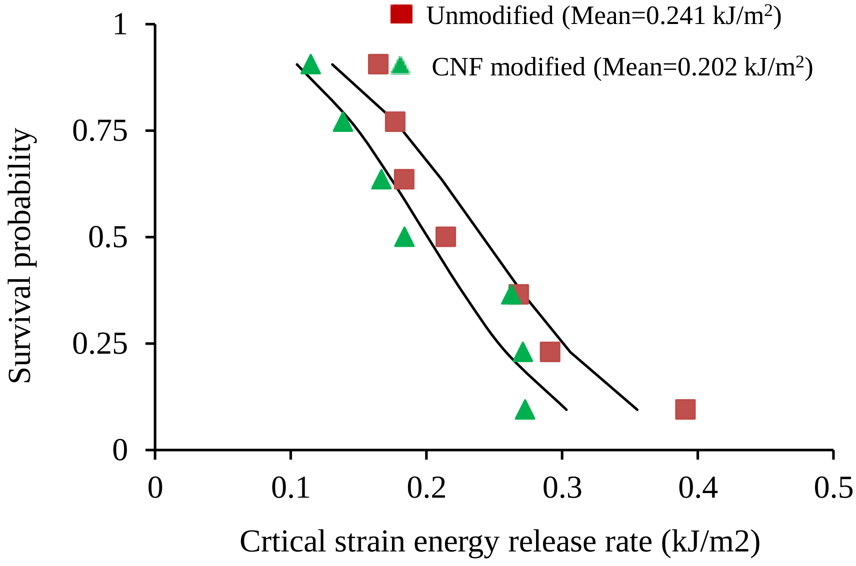

Figure 4.17. Survival probability vs. critical strain energy release rate plot of unmodified and PAN nanofiber modified samples (SC-15 epoxy resin system).

Table 4.5. Experimental results of the critical strain energy release rate of unmodified and CNF modified WCFF reinforced specimens.

Sample no.	Mode I critical strain energy release rate (G_{IC})	
	Unmodified specimens	CNF modified specimens
1	0.164	0.114
2	0.176	0.138
3	0.183	0.166
4	0.214	0.183
5	0.268	0.262
6	0.291	0.271

4.3.3.2. SEM fractographical analysis

Figure 4.18 shows the fracture surface of CNF modified specimens. It can be seen that the CNF breakage is brittle in nature. Because of this brittle nature, CNFs are unable to absorb substantial strain energy before breakage. Also, because the CNF surfaces are extremely smooth, the friction resistance is very low. Thus, the present experimental study indicates that though the CNFs can improve the flexural and shear strength properties (see Chapter 3), they are not capable of improving the interlaminar fracture toughness.

4.3.4. PAN nanofiber modified WCFF reinforced specimens (Epon 862)

From the previous test results, it was found that neither PAN nanofibers nor CNF can improve the interlaminar fracture toughness of SC-15 epoxy resin system. Also, the test results indicated that in general the interlaminar fracture toughness value of SC-15 epoxy was very high. From the literature, it was understood that such resin system has been toughened with rubber nanoparticles. Considering this fact, we further examined the potential interfacial toughening effect of nanofibers in composite laminates based on a relatively weak epoxy resin system without toughening phase. In this case, Epon 862 resin and Epicure 3234 hardener were selected. The following sections will describe the experimental results of composite laminates manufactured by Epon 862 resin and Epicure

3234 hardener system. The laminate manufacturing and testing methods were the same as the previous epoxy (SC-15) resin system. PAN nanofibers were used as interfacial reinforcement between the 6th and 7th plies of the twelve-ply laminates manufactured by WCFF lamina.

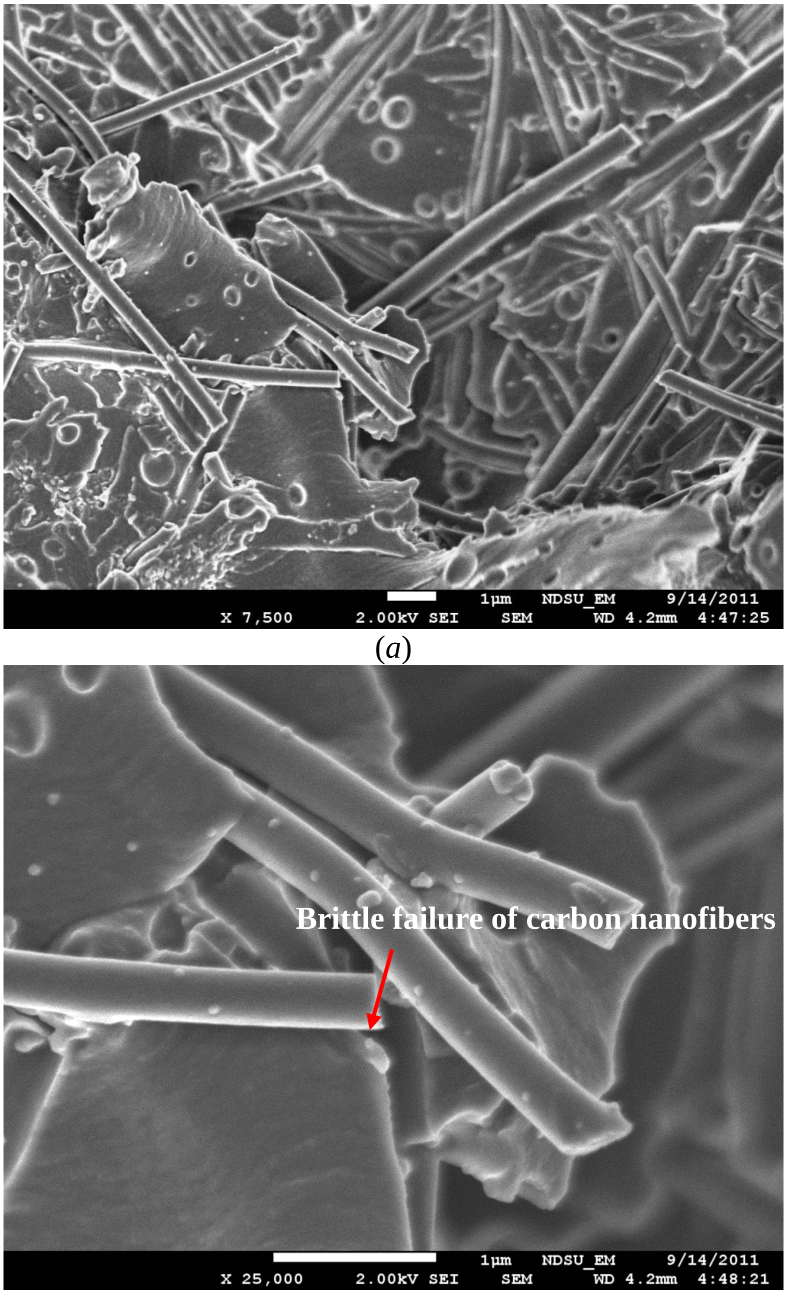

(*a*)

(*b*)

Figure 4.18. SEM fractographical analysis of a CNF modified WCFF reinforced specimen (*a*) fracture surface; (*b*) brittle failure mode of CFs (SC-15 epoxy resin system).

4.3.4.1. Experimental results

Figure 4.19 shows a typical load-displacement diagram of mode I interlaminar fracture test of PAN-NF modified WCFF reinforced specimens with Epon 862 resin and EPICURE 3234 hardener system. In this case, there was a substantial difference between the unmodified and modified load-displacement curves. It can be observed from Table 4.6 that the critical strain energy release rate is rather scattered as those of the previous studies in this research. Again, a two-parameter Weibull distribution model was used for data reduction and to examine the interfacial toughening effect of nanofibers in a statistical manner. Figure 4.20 shows variations of the survival probability vs. the critical strain energy release rate of the unmodified and modified specimens with a mean value of 0.261kJ/m^2 and 0.758 kJ/m^2, respectively. Thus, the mean critical strain energy release rate of PAN nanofiber modified samples was improved by 190.4 %, i.e., the improvement was almost twice.

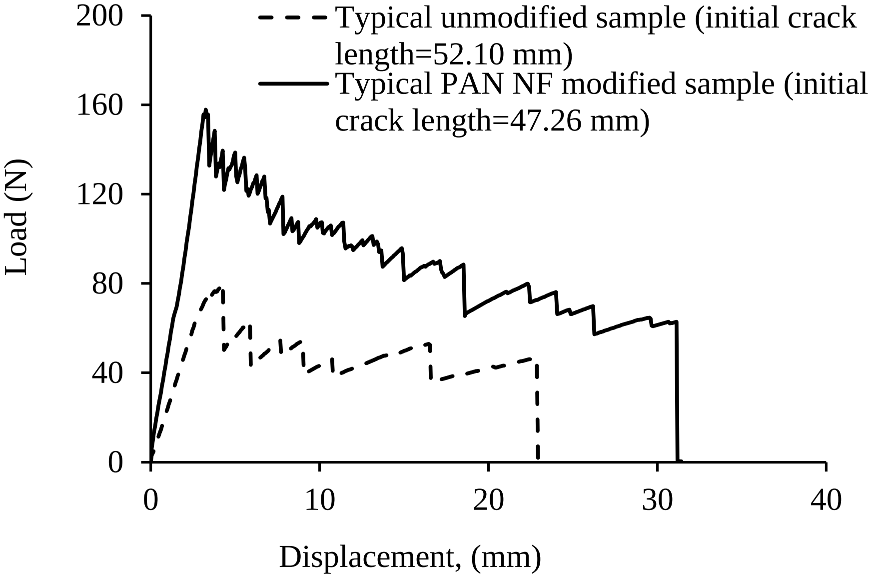

Figure 4.19. Typical load-displacement curves of mode I interlaminar tests (WCFF reinforced composites with Epon 862 epoxy resin system).

4.3.4.2. SEM fractographical analysis

Evaluation of the fracture surfaces of the specimens indicates that when mode I interlaminar fracture tests were performed, the PAN nanofibers experienced a plastic deformation. Also, unique surface rippling, fragmentation, and necking phenomena of PAN nanofibers were observed (Figure 4.21). As mentioned earlier, the surface ripples on the surface of electrospun nanofibers belong to a phenomenon of surface destabilization that could be correlated to the combined effect of surface tension and nonlinear elasticity of the compliant polymer nanofibers (Wu et al., 2008). Because of this property, PAN based nanofibers exhibited a substantial plastic deformation before their breakage and such plastic deformation can absorb a significant amount of strain energy. In addition, nanofiber bridging between the plies also played an important role in improving the fracture property of the interlayer.

4.4. Comparative discussion on the mode I interlaminar fracture behavior of tested laminates

Figures 4.22 to 4.24 show a comparative analysis of the mode I interlaminar fracture behavior of UDCFF and WCFF reinforced laminated composites. Figure 4.22 (*a*) shows that for UDCFF reinforced laminates, the microfiber bridging is very strong. However, no significant microfiber bridging was observed in the WCFF reinforced laminates [Figure 4.22 (*b*)]. Figure 4.23 shows the SEM image of the fracture surfaces for both UDCFF and WCFF reinforced laminates. Strong microfiber bridging accompanied noticeable microfiber breakage in UDCFF reinforced laminates were detected [Figure 4.23 (*a*)]. SEM image [Figure 4.23 (*b*)] shows that for the WCFF reinforced laminates, no obvious microfiber bridging and breakage can be detected. From the load-displacement curves (Figure 4.24), it was observed that the crack propagation in the UDCFF reinforced laminates was approximately consistent with load increase, whereas for WCFF reinforced laminates, big jumps were observed. The photographs of the fracture surfaces (Figure 4.22) also confirmed these big jumps. Such phenomenon may be attributed to the instantaneously unstable crack propagation coupled with rate-related viscoelastic properties of the resin. In this case, the stored energy could be released suddenly to give a brittle nature of the crack growth. Also, by comparing with the critical strain energy release rates of UDCFF (1.892 kJ/m^2) and WCFF reinforced laminates (0.524 kJ/m^2) (Sections 4.3.1.1 and 4.3.2.1), it can be concluded that the critical strain energy release rate for UDCFF reinforced laminates are almost three times that of the WCFF reinforced laminates.

The figures listed in Appendix B show that SC-15 epoxy resin system is rubber-nanoparticle toughened. Such resin exhibits significant crazing behavior both in tension and compression states (Bucknall, 2000). Craze initiation is usually observed at the equatorial region normal to the applied stress direction. In rubber modified epoxy resin systems, the craze terminates when it encounters another craze. Thus in rubber modified epoxy resins (density of the particles are high), crazes can prevent the large crack growth (Shaw, 1994). The process of craze growth can absorb huge fracture energy prior to cracking. It is generally believed that the initial energy absorption per unit area of a crazed region is up to several hundred times greater than that of un-crazed region (http://en.wikipedia.org/wiki/Crazing). Now, from the facture surface of Figure 4.22, it can be observed that the whitening region for UDCFF reinforced laminates (almost all the region is whitened) are much higher than that of the WCFF reinforced laminates. This observation can also confirm the higher fracture toughness of SC-15 epoxy resin system. Finally, it can be concluded that because of the high microfiber bridging, rubber toughening of the resin (SC-15) and consequently, constant crazing of the fracture surfaces, UDCFF reinforced laminates showed the fracture toughness much higher than that of WCFF reinforced counterparts. It is noted here that laminates prepared with Epon 862 and Epicure 3234 resin system did not show any crazing (white region) (Figure 4.25).

Table 4.6. Experimental results of the critical strain energy release rate of unmodified and PAN nanofiber modified WCFF reinforced specimens (Epon 862 epoxy resin system).

Sample no.	Mode I critical strain energy release rate (G_{IC})	
	Unmodified specimens	PAN nanofiber modified specimens
1	0.201	0.607
2	0.223	0.646
3	0.242	0.671
4	0.248	0.707
5	0.264	0.748
6	0.276	0.750
7	0.280	0.764
8	0.293	0.775
9	0.316	0.792

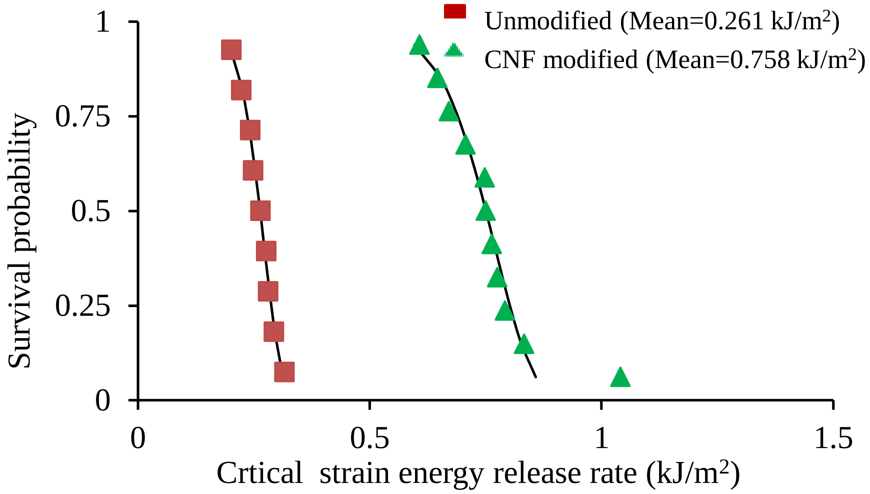

Figure 4.20. Variation of the survival probability vs. the critical strain energy release rate plot of unmodified and PAN nanofiber modified samples (Epon 862 epoxy resin system).

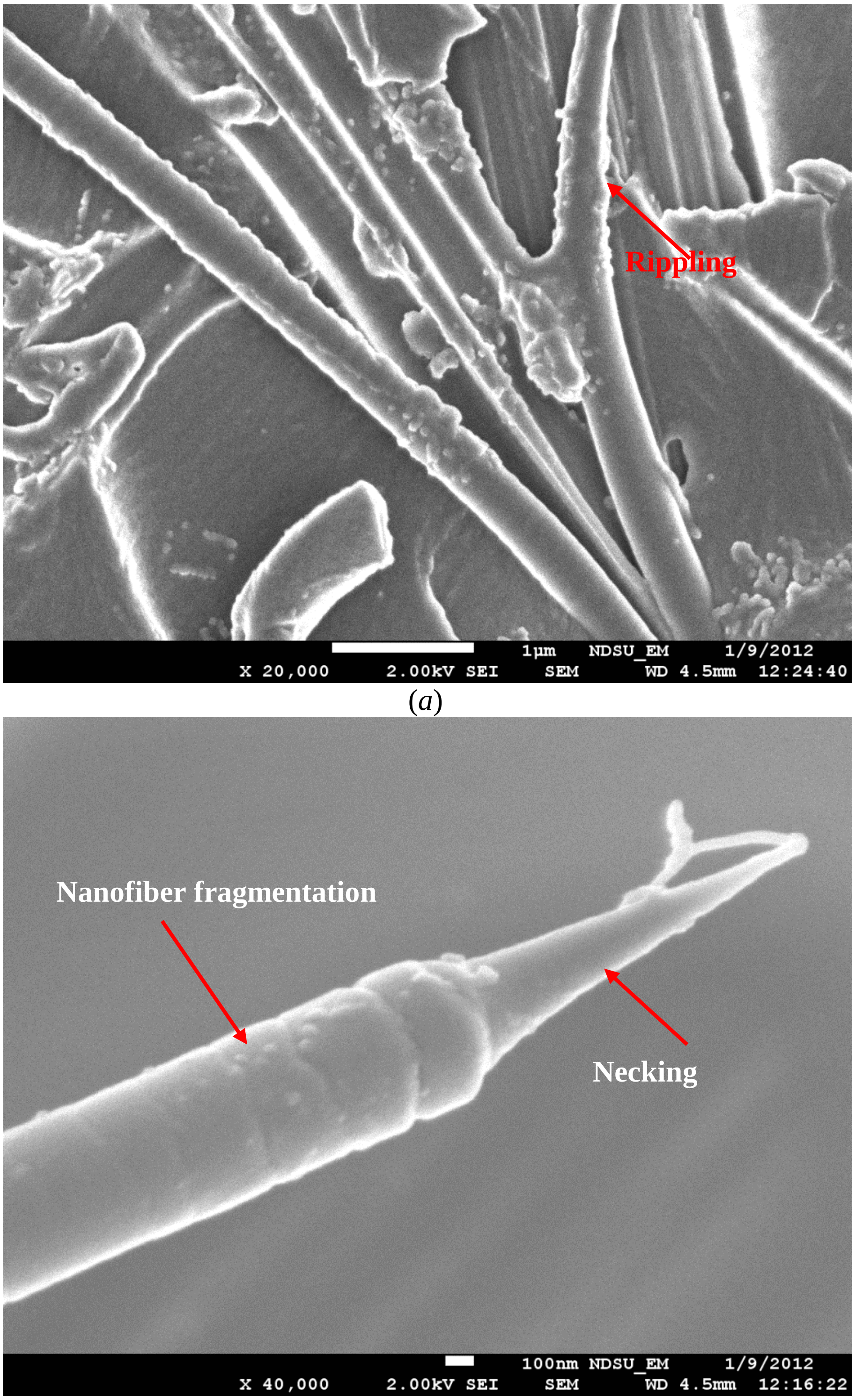

(*a*)

(*b*)

Figure 4.21. Rippling (*a*), fragmentation, and necking (*b*) of PAN nanofibers on the fracture surface of PAN nanofibers modified WCFF reinforced specimens (Epon 862 epoxy resin system).

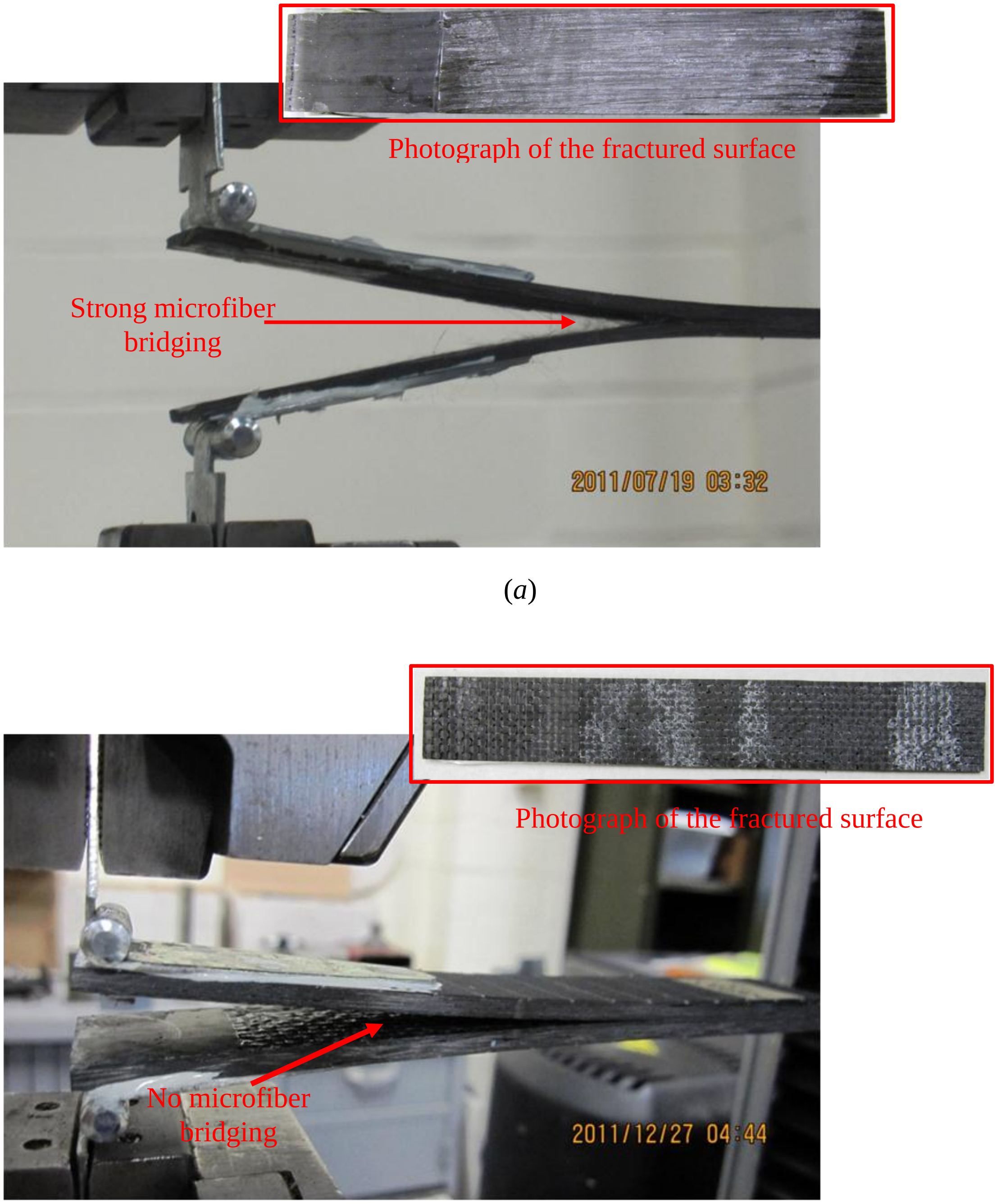

(*a*)

(*b*)

Figure 4.22. Comparison of the fracture surfaces for UDCFF and WCFF reinforced laminates in mode I interlaminar fracture test. (*a*) Strong microfiber bridging in UDCFF reinforced laminate, (*b*) no obvious microfiber bridging in WCFF reinforced laminate.

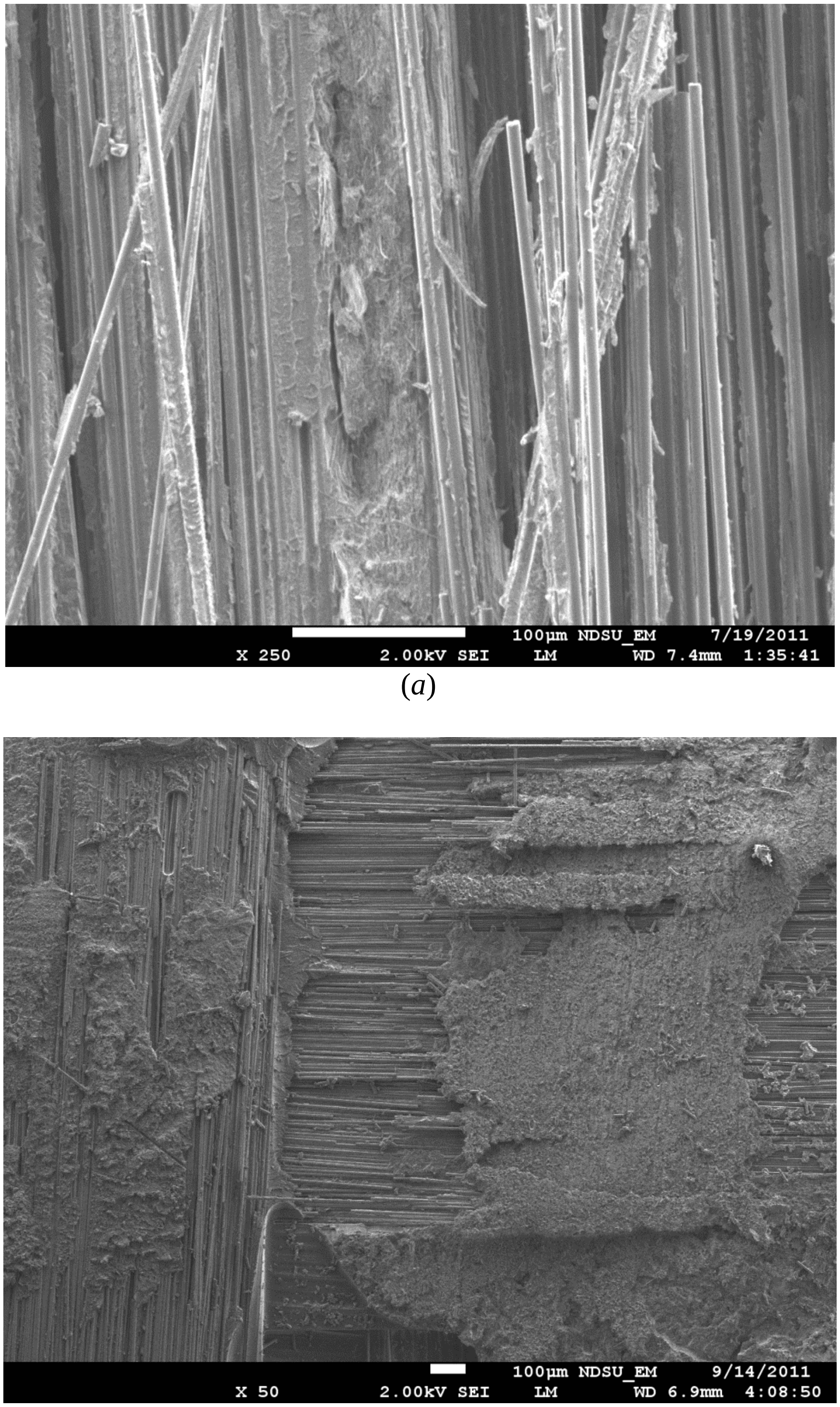

(*a*)

(*b*)

Figure 4.23. Comparison of SEM fractographical surfaces of mode I interlaminar fracture tests. (*a*) UDCFF/epoxy laminate and (*b*) WCFF/epoxy laminate (The matrix resin for both cases was SC-15).

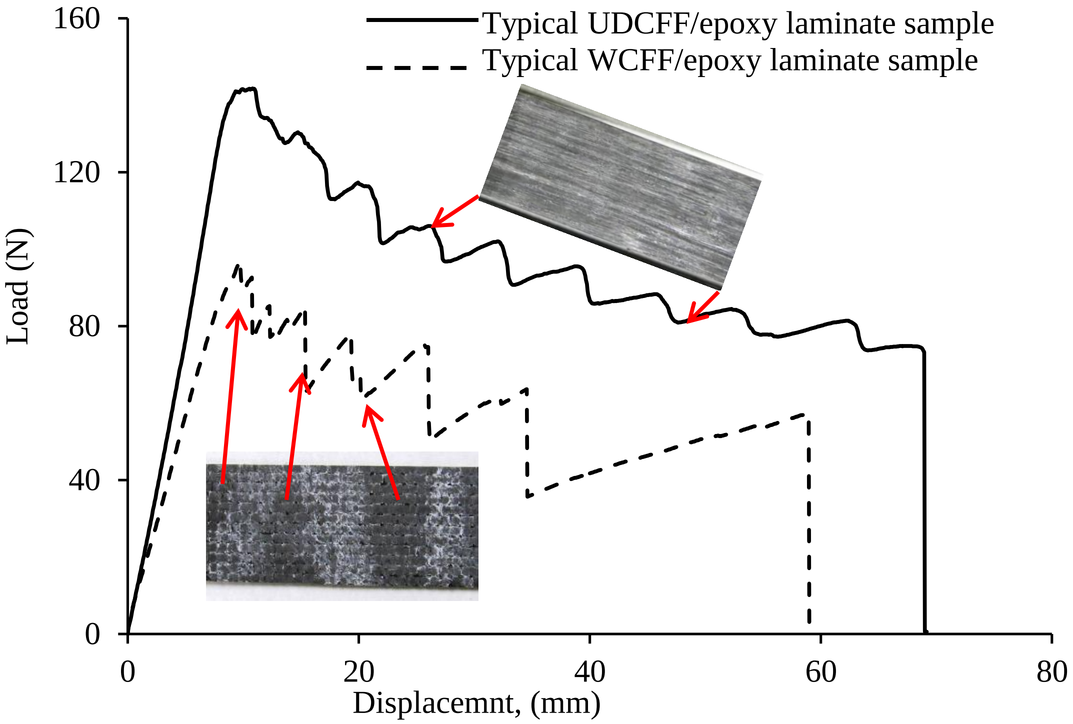

Figure 4.24. Comparison of typical load-displacement curves of mode I interlaminar fracture tests (UDCFF and WCFF with SC-15 epoxy resin system).

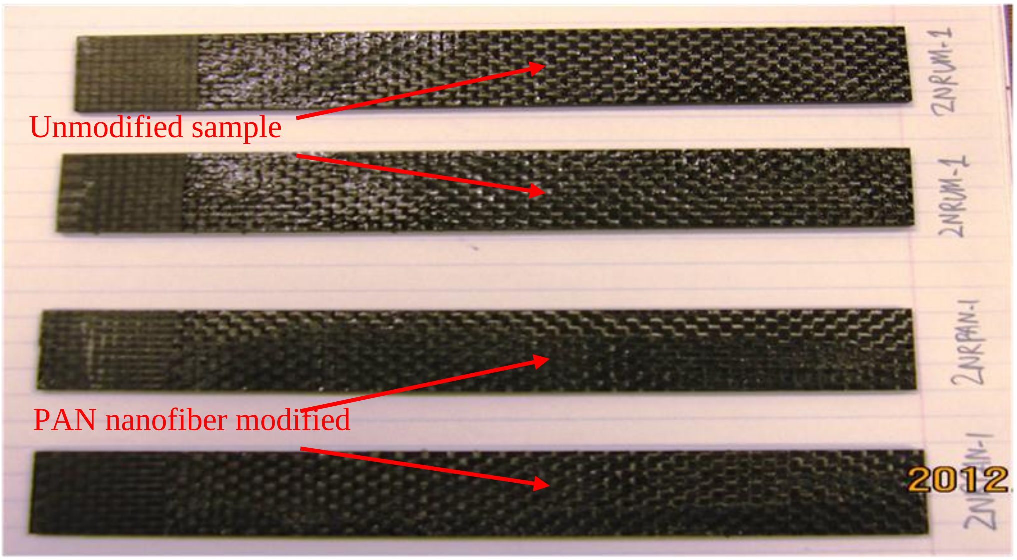

Figure 4.25. Fracture surfaces of unmodified and PAN nanofiber modified WCFF reinforced laminate composite with Epon 862 and Epicure 3234 resin system.

4.5. Summary of the experimental results

4.5.1. Summary of results for composite laminates based on SC-15 resin system

Both UDCFF and WCFF reinforced composites were modified with PAN nanofibers and CNFs to examine the effect of nanoreinforcement. For UDCFF reinforced composites with interfaces modified with PAN nanofibers, due to the suppression of strong microfiber bridging by the PAN nanofibers in UDCFF reinforced specimen, the fracture toughness of the laminates was decreased. Then, for WCFF reinforced composites with interfaces modified with PAN nanofibers and CNFs the toughening results were scattered in a wide range; however, in both cases the fracture toughness of the modified samples was decreased. On an average, it was found that due to incorporation of nanofibers at interfaces, the fracture toughness was decreased 20.21% for PAN nanofibers reinforced specimens and 16.18% for CNF reinforced specimens. The unique surface rippling, necking, and plastic deformation of the polymer nanofibers were revealed in this study. Also, it was found that in general the fracture toughness value for SC-15 epoxy was very high due to the toughening of the resin based on rubber nanoparticles. Thus, the present PAN nanofibers and CNFs could not further improve the fracture toughening of SC-15 based on composite laminates.

4.5.2. Summary of experimental results for composite laminates based on Epon 862 resin system

Mode I interlaminar fracture tests have been performed successfully. Experimental results indicate that the interlaminar fracture toughness of WCFF/epoxy composites reinforced with PAN nanofiber interlayers were increased 190.4% by comparison with those unmodified virgin samples that were fabricated with the same layup and processing conditions. Detailed SEM-based fractographical analysis indicated that the unique nanofiber bridging, surface rippling, fragmentation, and necking exerted by the thermoplastic PAN nanofibers are responsible for such improvement.

CHAPTER 5. CARBON-FIBER/EPOXY COMPOSITES REINFORCED WITH CORE-SHELL SELF-REPAIRING NANOFIBERS AT INTERFACES

This chapter focuses on the self-repairing effect of healing agent [Dicyclopentadiene (DCPD)] loaded ultrathin core-shell nanofibers in carbon fiber fabric (CFF)/epoxy composites in terms of stiffness recovery. Randomly oriented ultrathin self-repairing nanofibrous interlayers made of core-shell nanofibers encapsulated with healing agent were produced by coelectrospinning (Yarin, 2010; Sinha-Ray et al., 2012) and inserted between neighboring fabrics prior to resin infusion to process the novel self-repairing CFF/epoxy composites by means of VARTM technique. Grubbs' catalyst [http://en.wikipedia.org/wiki/Grubbs'_catalyst] was mixed into the resin in the system during the manufacturing process. Three-point bending tests were performed on the novel composite laminates with self-repairing interfaces. SEM-based fractographical analysis was performed to explore the toughening and self-repairing mechanisms of the novel hybrid multiscale self-repairing composites.

5.1. Introduction

Due to the presence of different phases, microscopic cracks and damages commonly exist in polymer composites. Under external loading such as localized impact and long duration of cyclic loads, these microscopic cracks further coalescence and grow into cracks and cavities. The unstable growth of these cracks results into the catastrophic failure of composites such as interlaminar delamination. In view of physics, all these failure processes are thermodynamically irreversible, i.e. the material properties gradually degrade with time. Taking into account this phenomenon, researchers are working on design and fabrication of polymers and polymer composites which are able to heal themselves whenever and wherever like the human body tissues (Blaiszik et al., 2010). Such polymer composites can significantly reduce the damage monitoring and maintenance costs. Therefore, polymer composites with self-repairing function would form a novel class of composites with high reliability.

Self-repairing composites can be obtained simply by producing the composites with healing-agent loaded matrix resin. The healing agents can be encapsulated inside vessels. Two types of vessels have been explored. One method is based on healing-agent loaded hollow glass fibers [Bleay et al. (2001), Pang and Bond (2005a & 2005b)] and the other one is based on healing-agent loaded microcapsule (Brown et al., 2003).

The applicability of hollow glass fibers were first demonstrated by Dry (1994 & 1996). During the process, brittle thin-walled vessels are filled with polymerizable medium. Meanwhile, Motuku et al. (1999) used the same approach for the study of self-repairing composites. It needs to be mentioned that both Dry and Motuku utilized the hollow fibers (tubes) with the diameter much larger than that of the reinforcing fibers in composites. In such approach, the hollow glass fiber containing healing agent may act as the initiator responsible for the failure of composites, thus it is unsuitable to use hollow glass fibers with the diameter in millimeters. Later, Bleay et al. (2001), Pang and Bond (2005a & 2005b) used hollow fibers with the diameter much smaller (micro scale) than that used by Dry and Motuku. They used a vacuum-assisted capillary-action filling technique to fill the healing agent into the hollow fibers. Furthermore, Trask et al. (2006 & 2007) and Williams et al. (2007) considered incorporating layers of self-repairing hollow glass fibers into glass fiber fabric (GFF)/epoxy and CFF/epoxy composites. Their experiments indicated that a significant amount of strength restoration can be achieved.

In their research, the hollowness of 50% with the fiber diameter ranging from 30-100 μm has been tested.

All the previous works on self-repairing composites involve microscopic hollow fibers or spherical tubes with the diameter in the range of ~100 μm. The size of the carriers can adversely affect the mechanical properties of the material (Sinha-Ray et al., 2012). For example, the self-repairing methods mentioned above can be hardly utilized to specifically heal localized interlaminar failure and damage of fiber-reinforced polymer composites without negative effect in their global mechanical properties. In addition, preparation of the hollow fibers and microcapsules are complicated and time consuming.

In contrast, Dr. Wu’s research group at NDSU has recently developed a unique, low-cost technical route (NDSU invention disclosure, 2012) to produce ultrathin, continuous core-shell polymer fibers loaded with healing agent. Compared to the existing self-repairing techniques reported in the literature, the present technique has several superior advantages as follows. First, the diameter of the core-shell self-repairing polymer nanofibers produced by coelectrospinning is one or two orders smaller than that of the existing hollow glass fibers and microcapsules, thus the core-shell nanofibers can be easily incorporated into the ultrathin thin resin-rich interlayers in fiber-reinforced composites as demonstrated in Chapter 4 and by other researchers (Dzenis, 2008; Wu, 2003; 2009). Due to the low volume of the nanofibers, this technique does not hurt the unique existing advantages of polymer composites such as the high volume fraction of the reinforcing fibers, high specific stiffness and strength, etc. Second, these core-shell nanofibers loaded with liquid healing agent can be produced conveniently by the mature low-cost coelectrospinning developed recently (Sun et al. 2003; Yarin, 2010). The formed self-repairing fibrous interlayers can be easily sandwiched between laminas during lay-up of the reinforcing-fiber fabrics or prepregs before curing. Thus, this technique can be easily merged into the conventional polymer-composite manufacturing process. Lastly, besides addition of the unique self-repairing function to the polymer composites, entanglement of the core-shell self-healing nanofibers at ply interfaces can also potentially enhance the interlaminar fracture toughness of the polymer composites as discussed in Chapter 4. In this experimental study, we aimed to explore the efficient production of core-shell nanofibers to load the healing agents as core material by using coelectrospinning (Sun et al. 2003). This chapter was to explore the processing and characterization of CFF/epoxy composites reinforced with self-repairing core-shell nanofibers at interfaces.

5.2. Experimental procedure

5.2.1. Preparation of self-repairing core-shell nanofiber mat

5.2.1.1. Materials

PAN powder (M_w=150 kDa) and liquid DCPD were purchased from Sigma Aldrich. All the chemicals were used as received without any further purification or change.

5.2.1.2. Coelectrospinning for self-repairing core-shell nanofibers

Standard coelectrospinning technique (Sun et al., 2003) was employed to produce core-shell PAN nanofibers to encapsulate liquid DCPD. During this process, a lab-made coaxial needle setup was utilized for generating the core-shell jet. The inner diameter of the exterior needle was 0.97 mm, while the outer and inner diameters of the interior needle were 0.71 mm and 0.48 mm, respectively. The solution of 10 wt% PAN in DMF was issued as the outer jet (shell) and the solution of 10 wt% DCPD in DMF was issued as the inner jet (core). The flow rates of the outer jet (shell) and the inner jet (core) were controlled by two digital syringe pumps as 1.5 ml/h and 1.0 ml/h, respectively. A high DC voltage of 18 kV was generated by a high DC voltage power supply (Gamma High Voltage Research, Inc., Ormond Beach, FL) and applied between the coaxial needle and a rotating aluminum disk covered with an aluminum foil (used as fiber collector) at a distance of 25 mm. Figure 5.1 shows the core-shell PAN/DCPD nanofibers.

5.2.2. Processing and characterization of self-repairing composites

During the process, Epon 862 epoxy resin and Epicure 3234 curing agent were selected as the polymeric matrix for processing the novel polymer composite (see Section 4.2.2 in Chapter 4 for the physical and mechanical properties of this resin system). The resin system was purchased from Miller-Stephenson Chemical Company, Inc. (Morton Grove, IL). The mix ratio of Epon 862 and Epicure 3234 were 100/14 by weight. UD CFF (UDCFF) (9.0 oz/yd^2) and woven CFF (WCFF) (5.7 oz/yd^2) were purchased from Fibre Glast Development Corp. (Brookville, OH) as used in the experiments in Chapter 4.

An eight-ply quasi-isotropic composite laminate with a $[0^o/\pm 45^o/90^o]_s$ stacking sequence was manufactured with the UDCFF and WCFF. The self-repairing core-shell nanofiber mats were introduced at the interfaces of $0^o/45^o$,$-45^o/90^o$,$90^o/-45^o$, and $45^o/0^o$, respectively, which are the predicted failure interfaces in quasi-isotropic laminates (Trask & Bond, 2006). Wet lay-up followed by VARTM was used for the composite processing (Figure 5.2) as described in Chapter 4. Vacuum pressure of 27 mm Hg was maintained during the initial curing at room temperature for 24 hrs. The obtained composite panels were further cured in an oven (1 hr at 100^{o}C) before the mechanical tests for self-repairing evaluation.

5.2.3. Specimen preparation and mechanical test set up

Composite specimens were cut from the laminates (5" × 5") [Figure 5.2 (*a*)] using a diamond-tipped rotary saw installed with a water cooling system. The dimensions of the specimens were: ~100 mm in length, ~20 mm in width, and ~2.35 mm in thickness [Figure 5.2 (*b*)]. Edges of the specimens were then polished with sand paper to avoid potential pre-damage. Three-point bending test (ASTM-D790) was selected to characterize the stiffness of the novel hybrid CFF/epoxy composite reinforced with self-repairing core-shell nanofibers at interfaces using a Instron machine. All the tests were performed at room temperature. The span between two supporting pins of the three-point bending test was 75 mm [Figure 5.2 (*c*)]. Five specimens were evaluated, and the mean value and standard deviation of stiffness values were calculated.

5.3. Experimental results and discussions

By using the three-point bending test setup, pre-damage test was first performed by loading the self-repairing composite specimens at a constant crosshead speed of 5 mm/min until the first ply failure. Then, the test was stopped and the tested specimen was immediately removed from the testing frame. To simplify the self-repairing process for comparison, four specimens after the pre-damage test were heated in a hot press at 100^{o}C for 1 hr. One specimen was kept as it was after the pre-damage test. All the pre-damaged specimens were post-tested at room temperature using the same testing procedure and control parameters.

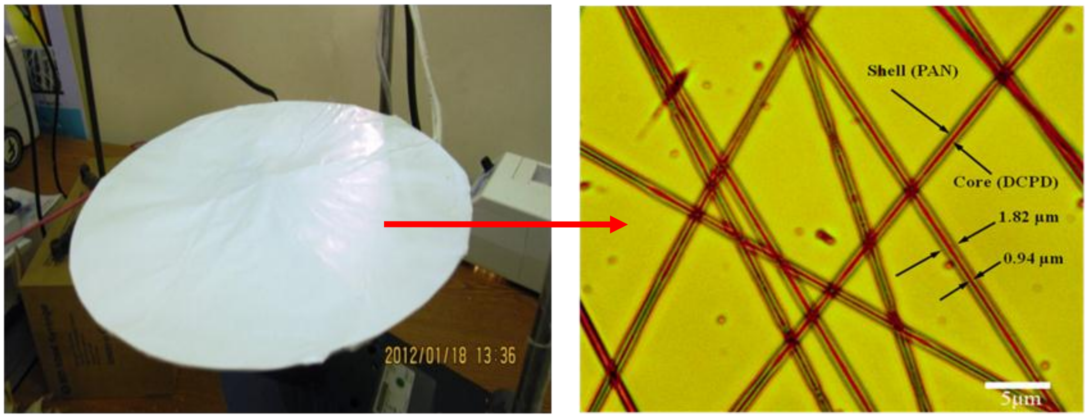

(*a*) (*b*)

Figure 5.1. Core-shell PAN/DCPD fibers: (*a*) fiber mat made of ultrathin core-shell nanofibers, (*b*) core-shell fiber morphologies (Z. Zhou, Dr. Wu's Group at NDSU).

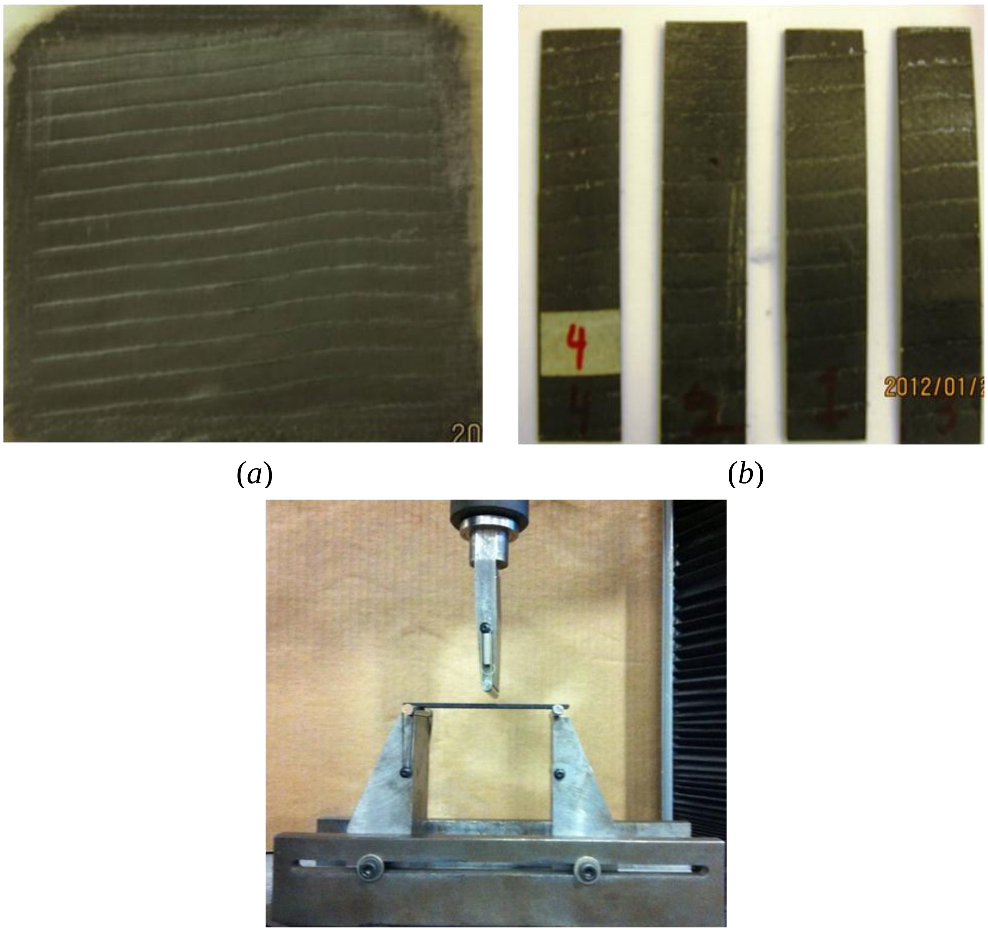

(*a*) (*b*)

(*c*)

Figure 5.2. Specimen preparation and test setup. (*a*) Laminate panel, (*b*) specimens (~100mm×20mm×2.35mm), (*c*) three-point bending test setup.

5.3.1. Experimental results and self-repairing effect

Figure 5.3 shows a typical load-displacement curve under three-point bending test and Figure 5.4 shows two comparative load-displacement curves of two other tested specimens. From Figure 5.4, it can be observed that the stiffness recovery after the heating is significant for each case. To better understand the self-repairing effect, the healing efficiency was calculated based on the stiffness recovery rate. Table 5.1 shows the results of the healing efficiency in terms of stiffness recovery percentage. This is calculated based on the initial stiffness and healed stiffness. It can be observed that except for one specimen, flexural stiffness of all the specimens is recovered in part by comparison with the ones at the unloading. The flexural stiffness of two specimens after self-repairing is even higher than that of the virgin ones. SEM fractographical analysis was employed to capture the evidence of the healing kinetics.

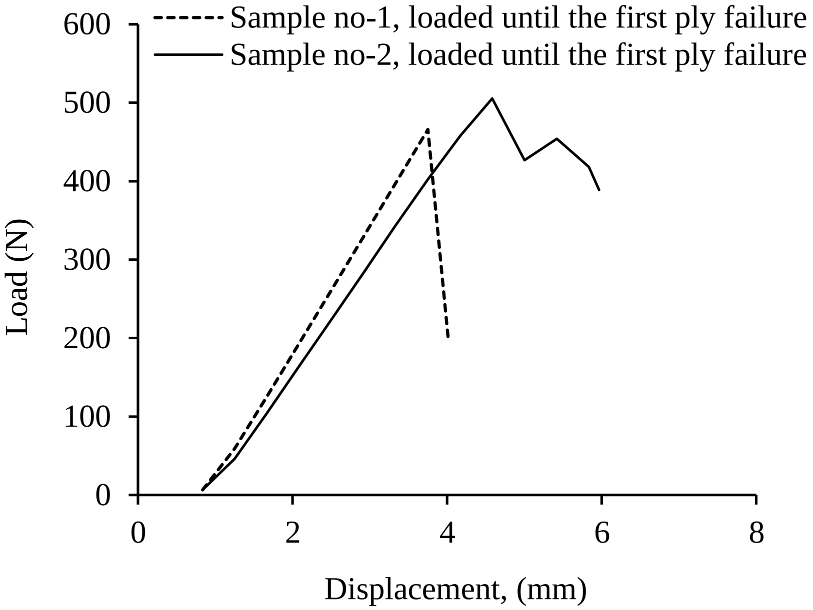

Figure 5.3. Typical load-displacement curves under three-point bending test of the novel hybrid self-repairing specimens (Until first ply failure).

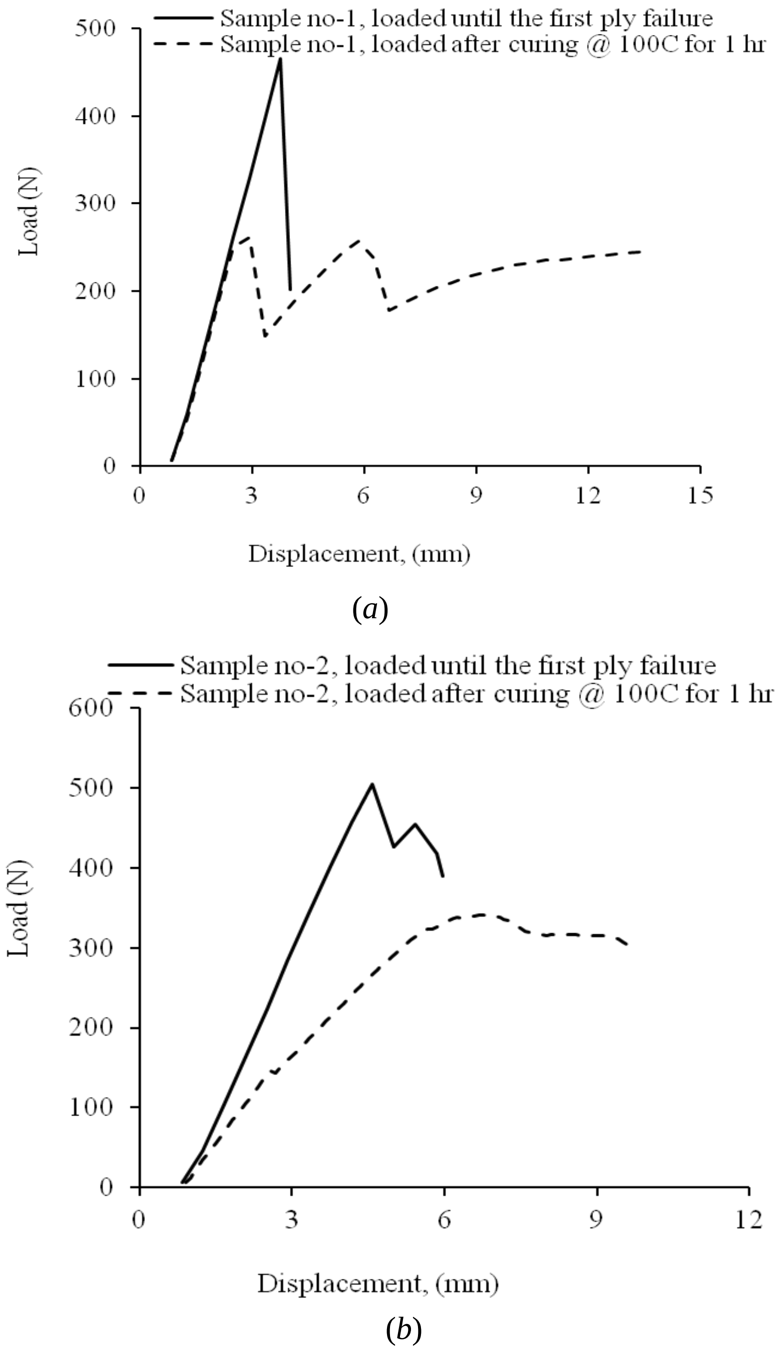

Figure 5.4. Typical comparative load-displacement curves under three-point bending test of the novel hybrid self-repairing specimens. (*a*) Sample No. 1 and (*b*) sample No. 2.

Table 5.1. Experimental data and healing efficiency in terms of stiffness.

Sample No.	Initial stiffness (E_0)	Stiffness after failure (E_{fpf})	Stiffness after healing (E_h)	Stiffness recovery (%)
1	163.885	61.213	158.978	97.005
2	144.836	74.532	98.973	68.334
3	145.541	46.337	150.523	103.422
4	49.0291	22.772	35.312	72.023
5	120.463	44.000	36.781	30.532

5.3.2. SEM fractographical analysis

SEM specimens were cut from the delaminated plies using a sharp scissor. Evaluation of the fracture surfaces was to show the evidence of the healing mechanisms. Figure 5.5 shows the fracture surfaces of the composite. It can be observed that when the core-shell nanofibers loaded with healing agent were scissored, the liquid healing agent released at crack surfaces. Once touching the matrix resin containing the Grubb's catalyst, the liquid healing agent (DCPD) polymerized and solidified instantaneously to seal the crack surfaces, similar to discrete stitching pins. The red circles in Figure 5.5 (*a*) clearly indicate the spots where healing agent released out of the core-shell nanofibers and solidified. Figure 5.5 (*b*) shows the core-shell fiber network. It can be detected that when the core-shell nanofibers were broken then released the healing agent [Figure 5.5 (*c*)]. Consequently, the monomer (healing agent) polymerized when coming across the catalyst (prevalent in the matrix). Simultaneously, the core-shell nanofibers can also function to toughen the polymer matrix via nanofiber bridging, pull-out, etc. as explored in Chapter 4 [see Figure 5.5 (*d*)].

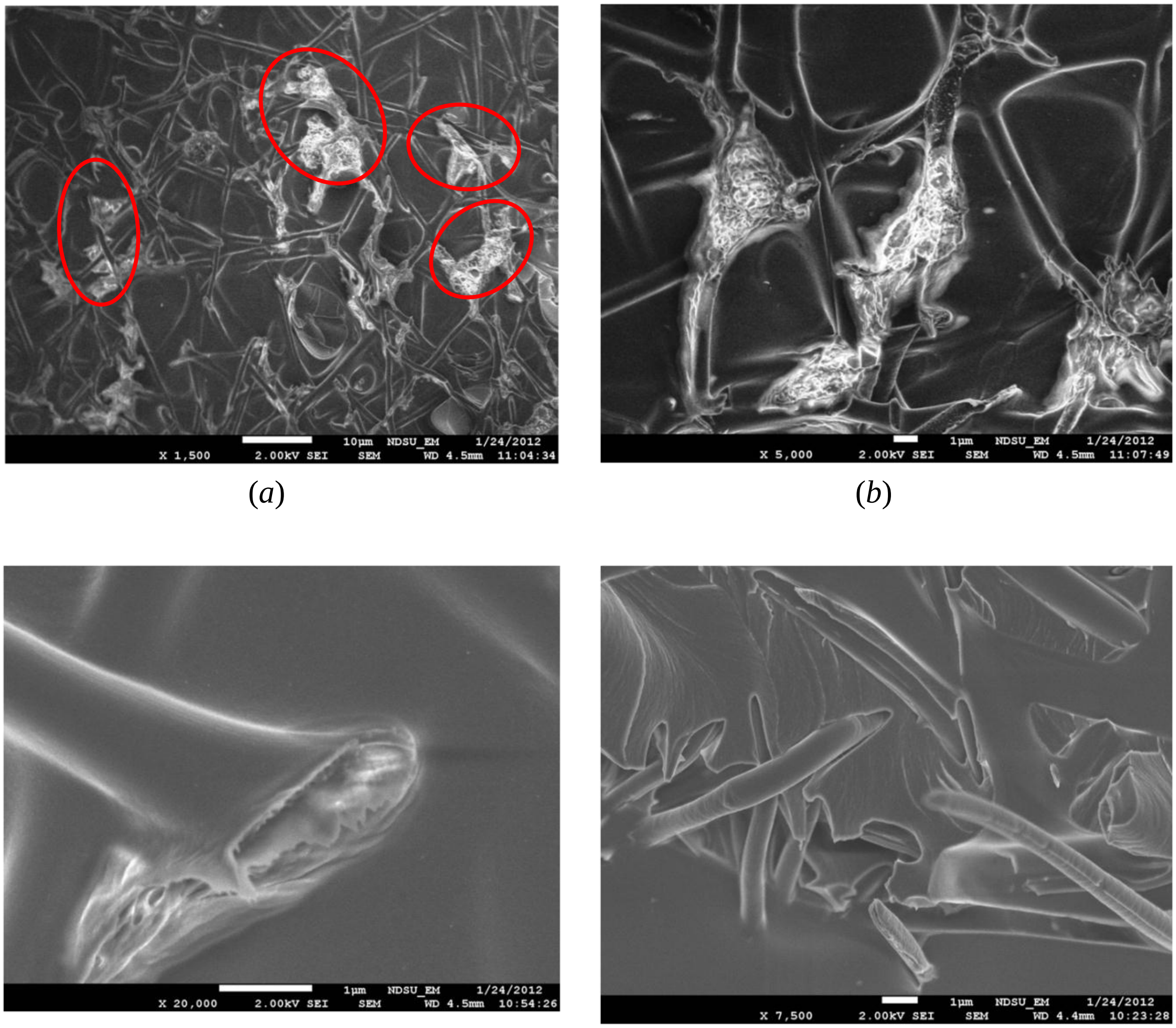

(*a*) (*b*)

(*c*) (*d*)

Figure 5.5. SEM fractographical analysis of hybrid self-reparing CFF/epoxy composite (*a*) fracture surface, (*b*) core-shell nanofiber network, (*c*) a single core-shell nanofiber breakage, and (*d*) toughening of the matrix by the nanofiber bridging, pull-out, etc.

5.4. Summary of results

The preliminary self-repairing tests indicate that the results of current self-repairing tests are still scattering, while the proof-of-concept self-repairing composite specimens did validate the self-repairing mechanisms. Detailed SEM-based fractographical analysis indicated that the healing agent release and polymerization on the fracture surface are responsible for such stiffness recovery. Also, it was evidenced in the SEM-based fractographical analysis that the core-shell PAN/DCPD nanofibers can also toughen the matrix by nanofiber bridging and pull out, among others.

CHAPTER 6. SUMMARY AND FUTURE RESEARCH

The experimental research of this thesis work focuses on the effect of interlaminar nanoreinforcement in several carbon fiber fabric (CFF)/epoxy composites. The CFF configurations were UD (UDCFF) and woven (WCFF). Two types of epoxy resin systems, namely SC-15 and Epon 862, were selected and used as the matrix resin for the research. Ultrathin toughening interlayers made of novel polymer nanofibers and CNFs were produced by electrospinning and carbonization of as-electrospun PAN nanofibers, respectively; these nanofibers were inserted between neighboring fabrics of the CFF/epoxy composites to produce the hybrid multiscale composites. Firstly, for hybrid multiscale composites, a piecewise layered theoretical model was developed, to examine the effect of interlaminar nanoreinforcement in the interfacial strength of the novel hybrid composites. Secondly, mode-I delamination tests were performed on various types of novel hybrid multiscale composites interleaved with PAN nanofibers and CNFs at the interfaces. Finally, the effect of ultrathin healing-agent-loaded core-shell nanofibers in CFF/epoxy composites was studied. The ultrathin self-repairing nanofibrous interlayers were produced by coelectrospinning and inserted between neighboring fabrics during the composite manufacturing. Three-point bending tests were performed on the novel composite laminates with self-repairing interfaces. Summary of the current research program and potential future research works on this study are presented in the following sections.

6.1. Summary of research program

In the first part of this research, a theoretical study was conducted on the hybrid multiscale composites to evaluate the effect of interlaminar nanoreinforcement. It was found that the shear and flexural strengths are correlated to the geometries and mechanical properties of the interlayers. The interlaminar properties can be enhanced substantially via incorporation with high stiffness and strength interlayers instead of simple pure resin interlayers that are formed during the composite processing.

In the second part of this research, an experimental program was conducted to evaluate the toughening effect of interlaminar nanoreinforcement on the delamination resistance of novel hybrid polymer composites. Both UDCFF and WCFF reinforced composites were modified with polymer nanofibers and CNFs to examine the toughening effect of the interlaminar nanoreinforcement. First, UDCFF/epoxy (SC-15) was reinforced with PAN nanofibers. Mode I delamination tests were performed. From the test results, it was found that due to the suppression of strong microfiber bridging by the PAN nanofibers, the fracture toughness of the resulting laminates was decreased in UDCFF reinforced specimens. Then, the WCFF reinforced composites were reinforced with PAN nanofibers and CNFs (as it was found that CNFs can improve the interlaminar shear and flexural strength to examining the toughening effect of these nanomaterials on the fracture toughness. The test results for WCFF reinforced composites with interfaces modified with PAN nanofibers and CNFs were scattered in a wide range; however, in both cases the fracture toughness of the modified samples was decreased. On an average, it was found that due to incorporation of nanofibers at interfaces, the fracture toughness was decreased by ~20% for PAN nanofiber reinforced specimens and ~16% for CNF reinforced specimens. The unique surface rippling, necking, and plastic deformation of the polymer nanofibers were revealed in this study, which offered rich experimental evidence for future study of the unique mechanical properties of polymer nanofibers.

Also, it was found that in general the fracture toughness of SC-15 epoxy was very high due to the involvement of tough rubber nanoparticles. The current study indicated that the present PAN nanofibers and CNFs could not further improve the fracture toughness of SC-15 based on composite laminates. Beyond that, we further examined the potential interfacial toughening effect of nanofibers in composite laminates based on a relatively weak epoxy resin system. In this case, Epon 862 resin and Epicure 3234 hardener were selected. Experimental results indicated that the interlaminar fracture toughness of WCFF/epoxy (Epon 862) composites reinforced with PAN nanofiber interlayers were improved up to 190.4% compared to those unmodified virgin samples that were fabricated with the same layup and processing conditions. Detailed SEM-based fractographical analysis indicated that the unique nanofiber bridging, surface rippling, fragmentation, and necking exerted by the thermoplastic PAN nanofibers are responsible for such improvement.

Finally, the effect of ultrathin healing-agent-loaded core-shell nanofibers in carbon-fiber/epoxy composites was studied. Ultrathin self-repairing nanofibrous interlayers made of core-shell nanofibers encapsulated with liquid healing agent were produced by coelectrospinning and inserted between neighboring fabrics. Three-point bending tests were performed on the novel composite laminates with self-repairing interfaces. SEM-based fractographical analysis of fractured sample surfaces confirmed the self-repairing mechanisms. The preliminary self-repairing tests indicate that the experimental self-repairing results are scattering, while the proof-of-concept self-specimens did validate the self-repairing mechanisms as expected. SEM images gained from fractographical analysis indicated that the healing agent release and polymerization on the fracture surface are responsible for the recovery of flexural stiffness of pre-damaged specimens. Also, it was evidenced that the core-shell PAN/DCPD nanofibers are able to toughen the matrix by nanofiber bridging, pull-out, plastic deformation, and so on.

6.2. Recommendations for future work

This present research has significantly advanced the research in interfacial toughening of advanced polymer composites and has also initiated a seminal research field of interfacial self-healing in polymer composites. The current research can be further extended to several directions in the future. Some recommendations for future work can be made below:

- It has been found that the interlaminar fracture toughness of polymer composites made of relatively weak resins can be improved by the polymer nanofibers. Yet, more detailed research is expected to evaluate the potential interfaical toughening effect in polymer composites subjected to cyclic (fatigue) and dynamic loading in pure and mixed-mode failure. Rate effect (either temperature or loading rate or both) would be considered as an important factor for interfacial tougening based on nanofibers.
- Though the proof-of-concept self-repairing composite has been validated, the effect of healing agent loaded core-shell nanofiers on the global mechanical propertis of the composites are needed to be explored.
- Potential applcations of the core-shell nanofibers for self-repairing of some other material systems such as ceramics, concretes, etc. can be further explored.

- Effect of the environmental conditions such as temperature, curing condition, etc. are needed to be studied for their applications in the real world.

REFERENCES

1. Adams, D. F., Carlsson, L. A., & Pipes, R. B. (2003) Experimental Characterization of Advanced Composite Materials. CRC Press: New York, p-29.
2. Agarwal, B. D. & Broutman, L. G. (1980) Analysis and Performance of Fiber Composites. Wiley: New York, p-315.
3. Alexandre, M. & Dubois, P. (2000) Polymer-layered silicate nanocomposites: preparation, properties and uses of a new class of materials. Materials Science and Engineering: R: Reports **28**, 1-63.
4. Anderson, H. M., Keller, M. W., Moore, J.S., Sottos, N.R., & White, S. R. (2007) Self healing in concrete materials. In S. van der Zwaag (ed.). Self Healing Materials – An Alternative Approach to 20 Centuries of Materials Science. Springer. The Netherlands, 19–44.
5. ASTM Standard. (2001) Standard Test Method for Mode I Interlaminar Fracture Toughness of Unidirectional Fiber-Reinforced Polymer Matrix Composites, ASTM Standard D 5528. ASTM International: West Conshohocken, Pennsylvania.
6. Auricchio, F. & Sacco, E. (2003) Refined first-order shear deformation theory models for composite laminates. Journal of Applied Mechanics **70**, 381–390.
7. Berthelot, J.-M. (1999) Composite materials: mechanical behavior and structural analysis, Springer, New York.
8. Beyakrova, E., Thostenson, E.T., Yu, A., Kim, Gao, H. J., & Tang, J. (2007) Multiscale carbon nanotube-carbon fiber reinforcement for advanced epoxy composites. Langmuir **23**, 3970–3974.

9. Bleay, S. M., Loader, C. B., Hawyes, V. J., Humberstone, L., & Curtis, P. T. (2001) A smart repair system for polymer matrix composites. Composites, Part A: Applied Science and Manufacturing **32**, 1767–1776.
10. Brown, E. N., Kessler, M. R., Sottos, N. R., & White, S. R. (2003). In situ poly (urea-formaldehyde) microencapsulation of dicyclopentadiene. J. Microencapsulation **20**, 719–730.
11. Blaiszik , B. J., Kramer , S. L. B., Olugebefola , S. C., Moore , J. S., Sottos , N. R., & White, S. R. (2010) Self-healing polymers and composites. Annual Review of Materials Research **40**, 179-.
12. Bucknall, C. B. (2000) Applications of microscopy to the deformation and fracture of rubber-toughened polymers. Journal of Microscopy **201**, 221-229.
13. Chan, C. M., Wu, J., Li, J. X., & Cheung, Y. K. (2002) Polypropylene/calcium carbonate nanocomposites. Polymer **43**, 2981-2992.
14. Chand, S. (2000) Carbon fibers for composites. Journal of Materials Science **35**, 1303-1313.
15. Chen, Q., Zhang, L. F., Rahman, A., Zhou, Z. P., Wu, X. F., & Fong, H. (2011) Hybrid multi-scale epoxy composites made of conventional carbon fiber fabrics with interlaminar regions containing electrospun carbon nanofiber mats. Composites Part A: Applied Science and Manufacturing **42**, 2036-2042.
16. Chen, Q., Zhao, Y., Zhou, Z. P., Rahman, A., Wu, X. F., & Fong, H. (2012) Fabrication and evaluation of hybrid multi-scale epoxy composites reinforced with conventional carbon fiber fabrics surface-covered with electrospun carbon nanofiber mats. Composites Part B: Engineering (to be submitted).

17. Chou, T. W. (1992) Microstructural Design of Fiber Composites. Cambridge University Press, UK.

18. Carlsson, L. A. & Pipes, R. B. (1987) Experimental Characterization of Advanced Composite Materials. New Jersey: Prentice-Hall, Inc., NJ.

19. Carlsson, L. A. & Aksoy, A. (1999) Analysis of interleaved end-notched flexure specimen for measuring mode II fracture toughness. International Journal of Fracture **52**, 67-77.

20. Carlson, H. C. & Goretta, K. C. (2006) Basic materials research programs at the U.S. Air Force Office of Scientific Research. Materials Science and Engineering B **132**, 2-7.

21. Coleman, J. N., Khan, U., & Gun'ko, Y. K. (2006) Mechanical reinforcement of polymers using carbon nanotubes. Advanced Materials **18**, 689-706.

22. Daniel, I.M. and Ishai, O. (2006) Engineering Mechanics of Composite Materials. Oxford University Press (2nd Edition).

23. Dransfield, K., Baillie, C., & Mai, Y. W. (1994) Improving the delamination resistance of CFRP by stitching-A review. Composite Science and Technology **50**, 305-317.

24. Dry, C. (1992). Passive tunable fibers and matrices. International Journal of Modern Physics B **6**, 2763–2771.

25. Dry, C., & Sottos, N. R. (1993) Passive smart self-repair in polymer matrix composite materials. Proceedings of SPIE–The International Society for Optical Engineering **1916**, 438–444.

26. Dry, C. (1994) Matrix cracking repair and filling using active and passive modes for smart timed release of chemicals from fibers into cement matrices. Smart Materials and Structures **3**, 118–123.

27. Dry, C. (1996) Procedures developed for self-repair of polymer matrix composite materials. Composite Structures **35**, 263–269.

28. Dzenis, Y. A. & Joshi, S. P. (1994) Damage evolution modeling in orthotropic laminated composites. AIAA Journal **32**, 357-364.

29. Dzenis, Y. A. (1996) Stochastic Damage Evolution Modeling in Laminates. Journal of Thermoplastic Composite Materials **9**, 21-34.

30. Dzenis, Y. A. & Qian, J. (2001) Analysis of microdamage evolution histories in composites. International Journal of Solids and Structures **38**, 1831–1854.

31. Dzenis, Y. A. (2008) Structural nanocomposites. Science **319**, 419–420.

32. Dzenis, Y.A. & Reneker, D.H. (2001) Delamination resistant composites prepared by small diameter fiber reinforcement at ply interfaces. US Patent **6,265,333**.

33. Gay, D., Hoa, S.V., & Tsai, S.N. (2003) Composite Materials: Design and Application. CRC Press, New York.

34. Garg, A. C. & Mai, Y. W. (1988) Failure mechanisms in toughened epoxy resins-A review. Composites Science and Technology **31**, 179-223.

35. Grimsley, B.W., Cano, R. J., Johnson, N.J., Loos, A. C., & McMahon, W. M. (2001) Hybrid composites for LH_2 fuel tank structure. In: Proceedings of 33rd international SAMPE technical conference, November 4–8, Seattle, Washington. pp. 1224–1235.

36. Hansen, C., Wu, W., Toohey, K. S., Sottos, N. R., White, S. R., & Lewis, J. A. (2009) Self-healing materials with interpenetrating microvascular networks. Advanced Materials **21**, 1-5 (2009).

37. Hashemi, S., Kinloch, A. J., & Williams, J. G. (1990). The analysis of interlaminar fracture in uniaxial fibre-polymer composites. Proceedings of the Royal Society of London A **427**, 173–99.

38. Jang, B. Z. (1994). Advanced Polymer Composites: Principles and Applications. Materials Park: ASM Internals, OH.

39. Jones, R. M. (1999). Mechanics of Composite Materials. (2nd edition). Philadelphia: Taylor & Francis, MA.

40. Jones, A. S., Rule, J. D., Moore, J. S., White, S. R., & Sottos N. R. (2006) Catalyst morphology and dissolution kinetics of self-healing polymers. Chemistry of Materials **18**, 1312-1317.

41. Kamphaus, J. M., Rule, J. D., Moore, J. S., Sottos, N. R., & White, S. R. (2008) A new self-healing epoxy with tungsten (VI) chloride catalyst. Journal of the Royal Society Interface **5**, 95-103.

42. Kang, W., Rajagopalan, J., & Saif, M. T. A. (2010) In Situ Uniaxial Mechanical Testing of Small Scale Materials-A Review. Nanoscience and Nanotechnology Letters **2**, 282-287.

43. Kevin, O. T. & Roderick, H. M. (1993). Round Robin testing for mode I interlaminar fracture toughness of composite material. Journal of Composites Technology and Research **15**, 269-281.

44. Kim, J. K. & Mai, Y. W. (1991) High strength, high fracture toughness fiber composites with interface control-A review. Composites Science and Technology **41**, 333-378.

45. Lai, C. L., Guo, Q. H., Wu, X. F. , Reneker, D. H., & Hou, H. Q. (2008) Growth of carbon nanostructures on carbonized electrospun nanofibers with palladium nanoparticles. Nanotechnology **19**, 195303.

46. Li, J., Sham, M. L., & Kim, J. K. (2007) Morphology and properties of UV/ozone treated graphite nanoplatelet/epoxy nanocomposites. Composites Science and Technology **67**, 296-305.

47. Lin, S., Cai, Q., Ji, J., Sui, G., Yu, Y., Yang, X., Ma, Q., Wei, Y., & Deng, X. (2008) Electrospun nanofiber reinforced and toughened composites through in situ nano-interface formation. Composites Science and Technology **68**, 3322-3329.

48. Liu, Y., Hedin, N. E., & Fong, H. (2008) Polycarbonate/poly (methyl methacrylate) nanofiber composites with improved impact strength. Journal of Advanced Materials **40**, 33-42.

49. Low, I. M. & Mai, Y. M. (1990) Fracture properties and failure mechanism of pure and toughened epoxy resins. in Handbook of Ceramics and Composites (edited by N. P. Cheremisinoff) **2**, 105-150.

50. Mallick, P. K. (1993) Fiber-reinforced composites: materials, manufacturing, and design. New York: Marcel Dekker. Inc., p. 6-47.

51. Mangun, C. L., Mader, A. C., Sottos, N. R., & White, S. R. (2010) Self-healing of a high temperature cured epoxy using poly (dimethylsiloxane) chemistry. Polymer **51**, 4063-4068.

52. Mauldin, T. C., Rulel, J. D., Sottos, N. R., White, S. R., & Moore, J. S. (2007) Self-healing kinetics and the stereoisomers of dicyclopentadiene. Journal of the Royal Society: Interface **4**, 389–393.

53. Motuku, M., Vaidya, U. K., & Janowski, C. M. (1999) Parametric studies on self-repairing approaches for resin infused composites subjected to low velocity impact. Smart Materials and Structures **8**, 623–638.

54. Mourtiz, A. P., Gallagher, J., & Goodwin, A. A. (1997) Flexural strength and interlaminar shear strength of stitched GRP laminates following repeated impacts. Composites Science and Technology **57**, 509-522.

55. Murphy, E. B. & Wudl, F. (2010) The world of smart healable materials. Progress in Polymer Science **35**, 223.

56. Murthy, M. V. V. (1981) An improved transverse shear deformation theory for laminated anisotropic plates. NASA Technical Paper.

57. Naraghi, M., Chasiotis, I., Kahn, H., Wen, Y. K., & Dzenis. Y. (2007a) Mechanical deformation and failure of electrospun polyacrylonitrile nanofibers as a function of strain rate. Applied Physics Letters **91**, 151901.

58. Naraghi, M., Chasiotis, I., Kahn, H., Wen, Y., & Dzenis. Y. (2007b) Novel method for mechanical characterization of polymeric nanofibers. Review of Scientific Instruments **78**, 085108.

59. Naraghi, M. & Chasiotis, I. (2009) Mechanics of PAN Nanofibers in Major Accomplishments in Composite Materials and Sandwich Structures: An anthology of ONR Sponsored Research (edited by I. M. Daniel), Springer, pp. 757.

60. Nguyen, T. K., Sab, K., & Bonnet, G. (2008) First-order shear deformation plate models for functionally graded materials. Composite Structures **83**, 25–36.

61. Pang, J. W. C., & Bond, I. P. (2005a) A hollow fibre reinforced polymer composite encompassing self-healing and enhanced damage visibility. Composites Science and Technology **65**, 1791–1799.
62. Pang, J. W. C., & Bond, I. P. (2005b) Bleeding composites-damage detection and self-repair using a biomimetic approach. Composites Part A: Applied Science and Manufacturing **36**, 183–188.
63. Reddy, J. N. (1984) A simple higher-order theory for laminated composite plates. Journal of Applied Mechanics **51**, 745-752.
64. Reneker, D. H., Yarin, A. L., Fong, H., & Koombhongse, S. (2000) Bending instability of electrically charged liquid jets of polymer solutions in electrospinning. Journal of Applied Physics **87**, 4531–4547.
65. Reneker, D. H. & Chun, I. (1996) Nanometre diameter fibres of polymer, produced by electrospinning. Nanotechnology **7**, 216–223.
66. Rosselli, F. & Santare, M. H. (1997) Comparison of the short beam shear (SBS) and interlaminar shear device (ISD) tests. Composites Part A: Applied Science and Manufacturing **28**, 587–594
67. Sager, R. J., Klein, P. J., Davis, D. C., Lagoudas, D. C., Warren, G. L., & Sue, H. J. (2011). Interlaminar fracture toughness of woven fabric composite laminates with carbon nanotube/epoxy interleaf films. Journal of Applied Polymer Science **121**, 2394–2405.
68. Sinha-Ray, S., Pelot, D. D., Zhou, Z. P., Rahman, A., Wu, X. F., & Yarin, A.L. (2012) Encapsulation of self-healing materials by coelectrospinning, emulsion electrospinning and solution blowing and intercalation. Journal of Materials Chemistry (Accepted).

69. Shaw, S. (1994) Rubber modified epoxy resins. in Rubber Toughened Engineering Plastics, A. Collyer (ed.). Chapman & Hall, 165–209.
70. Subramaniyan, A. K., & Sun, C. T. (2007) Toughening polymeric composites using nanoclay: crack tip scale effects on fracture toughness. Composites Part A: Applied Science and Manufacturing **38**, 34–43.
71. Subramaniyan, A. K., & Sun, C. T. (2008) Interlaminar fracture behavior of nanoclay reinforced glass fiber composites. Journal of Composite Materials **42**, 2111–2122.
72. Sun, Z., Zussman, E., Yarin, A. L., Wendorff, J. H. & Greiner, A. (2003) Compound core/shell polymer nanofibers by co-electrospinning. Advanced Materials **15**, 1929–1932.
73. Talreja, R. (1994) Damage Mechanics of Composites. New York: Elsevier.
74. Tenney, D. & Pipes, R. B. (2001) Advanced composites development for aerospace applications. The 7th Japan International SAMPE Symposium and Exhibition. Tokyo: Japan, 2001-11-13.
75. Theron, A., Zussman, E., & Yarin, A. L. (2001) Electrostatic field-assisted alignment of electrospun nanofibres. Nanotechnology **12**, 384–390.
76. Thostenson, E. T., Li, W. Z., Wang, D. Z., Ren, Z. F., & Chou, T. W. (1998) Carbon nanotube/carbon fiber hybrid multiscale composites. Journal of Applied Physics **91**, 6034–6037
77. Thostenson, E. T., Li, C., & Chou, T. W. (2005) Nanocomposites in context. Composites Science and Technology **65**, 491-516.
78. Trask, R. S., & Bond, I. P. (2006). Biomimetic self-healing of advanced composite structures using hollow glass fibres. Smart Materials and Structures **15**, 704–710.

79. Trask, R. S., Williams, G. J., & Bond, I. P. (2007) Bioinspired self-healing of advanced composite structures using hollow glass fibres. Journal of the Royal Society: Interface **4**, 363–371.

80. Toohey, K., Sottos, N. R., & White, S. R. (2009) Characterization of microvascular-based self-healing coatings. Experimental Mechanics **49**, 707-717.

81. Tsai, S. W. (2005) Three decades of composites activities at US Air Force Materials Laboratory. Composites Science and Technology **65**, 2295-2299.

82. Vable, M. (2008) Intermediate Mechanics of Materials. Oxford: Oxford University Press, UK.

83. Van der Zwaag, S. (2007). Self-Healing Materials-An Alternative Approach to 20 Centuries of Materials Science. Springer: New York.

84. Veedu, V. P., Cao, A., Li, X., Ma, K., Soldano, C., Kar, S., Ajayan, P. M., & Ghasemi-Nejhad, M. N. (2006) Multifunctional composites using reinforced laminae with carbon-nanotube forests. Nature Materials **5**, 457-462.

85. Wicks, S. S., Guzman de Villoria, R., & Wardle, B. L. (2010) Interlaminar and intralaminar reinforcement of composite laminates with aligned carbon nanotubes. Composites Science and Technology **70**, 20-28.

86. Williams, G., Trask, R. S., & Bond, I. P. (2007) A self-healing carbon fiber reinforced polymer for aerospace applications. Composites Part A: Applied Science and Manufacturing **38**, 1525–1532.

87. Whitney, J. W. (1969) The effect of transverse shear deformation on the bending of laminated plates. Journal of Composite Materials **3**, 534-547.

88. White, S. R., Sottos, N. R., Geubelle, Moore, J. S., Kessler, M. R., Sriram, S. R., Brown, E. N. and Viswanathan, S. (2001) Autonomic healing of polymer composites, Nature **409**, 794-797.
89. Whitney, J. M. & Browning, C. E. (1985) On Short-Beam Shear Tests for Composite Materials. Experimental Mechanics **25**, 294-300.
90. Whitney, J. M. & Pagano, N. J. (1970) Shear deformation in heterogeneous anisotropic plates. Journal of Composite Materials **37**, 1031-1036.
91. Whitney, J. M. (1987). Structural Analysis of Laminated Anisotropic Plates. Technomic Publishing Company, Lancaster.
92. Wool, R. P. (2001) A material fix. Nature **409**, 794-797.
93. Wu, X.F. (2003). Fracture of Advanced Polymer Composites with Nanofiber Reinforced Interfaces. Ph.D. thesis, University of Nebraska, Lincoln, USA.
94. Wu, X.F. & Dzenis, Y. A. (2005) Experimental determination of probabilistic edge delamination strength of a graphite–fiber/epoxy composite. Composite Structure **70**, 100–108.
95. Wu, X. F. & Dzenis, Y. A. (2005) Determination of dynamic delamination toughness of a graphite-fiber/epoxy composite using Hopkinson pressure bar. Polymer Composites **26**, 165-180.
96. Wu, X. F., Kostogorova-Beller, Y. Y., Goponenko, A. V., Hou, H. Q., & Dzenis, Y. A. (2008) Rippling of polymer nanofibers. Physical Review E **78**, 061804.
97. Wu, X. F. (2009) Fracture of Advanced Polymer Composites with Nanofiber Reinforced Interfaces: Fabrication, Characterization, and Modeling. VDM Verlag (Germany).

98. Wu, X. F., Zhou, Z. P., Rahman, A., & Bedarkar, A. (2012) Mechanical properties of continuous nanofibers: Characterization and mechanics. Chapter 8 in Nanostructures: Properties, Production Methods and Applications [Editors: Yu (Roger) Dong]. Nova Publisher, USA (Accepted).
99. Yarin, A. L., Koombhongse, S., & Reneker, D. H. (2001) Taylor cone and jetting from liquid droplets in electrospinning of nanofibers. Journal of Applied Physics **89**, 4836–4846.
100. Yarin, A. L. & Zussman, E. (2004) Upward needleless electrospinning of multiple nanofibers. Polymer **45**, 2977-2980.
101. Yarin, A.L. (2010). Coaxial electrospinning and emulsion electrospinning of core–shell fibers. Polymers Advanced Technology, 22, 310–317.
102. Yong, L., & Ji-Huan, H. (2007) Bubble electrospinning for mass production of nanofibers. International Journal of Nonlinear Sciences and Numerical Simulation **8**, 393–396.
103. Youngblood, J. P. & Sottos, N. R. (2008) Bioinspired materials for self-cleaning and self-healing. MRS Bulletin **33**, 732-741.

APPENDIX A. STRESS VARIATION ALONG THE DEPTH OF A BEAM

To observe the stress variation along the depth of a beam, it is necessary to analyze the beam as a special orthotropic material (three mutually perpendicular planes of symmetry). In general, for a special orthotropic material, 9 independent material parameters exist to describe its deformation ($E_{11}, E_{22}, E_{33}, \nu_{12}, \nu_{13}, \nu_{23}, G_{12}, G_{13}$ and G_{23}) (Daniel & Ishai, 2006).

1. Stress nomenclature

Figure A-1 shows the reference axes and the stresses acting on a stress element of a point inside an anisotropic material.

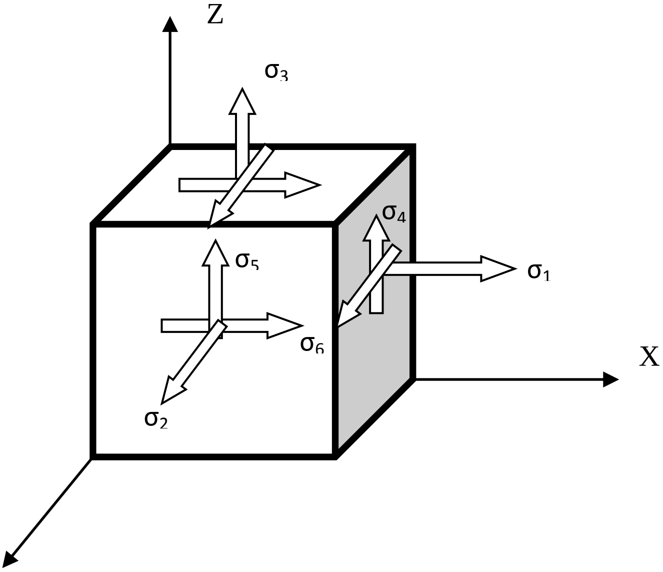

Figure A-1. Stress nomenclature of a material point inside the body.

2. Laminate: Strain-displacement relations

With the assumption of small deformation, the strain-displacement relationships of an elastic body can be expressed using Green strain tensor:

$$\epsilon_{11} = \frac{\partial u_1}{\partial x_1}\ ,\ \epsilon_{22} = \frac{\partial u_2}{\partial x_2}, \epsilon_{33} = \frac{\partial u_3}{\partial x_3} \tag{A-1}$$

$$\epsilon_{23} = \frac{\partial u_3}{\partial x_2} + \frac{\partial u_2}{\partial x_3}, \epsilon_{13} = \frac{\partial u_3}{\partial x_1} + \frac{\partial u_1}{\partial x_3}, \epsilon_{12} = \frac{\partial u_2}{\partial x_1} + \frac{\partial u_1}{\partial x_2} \tag{A-2}$$

3. Plate displacement

With Kirchhoff's plate assumption, the in-plane displacements *u* and *v* are linear functions of the *z*-coordinate (Figure A-2); the transverse shear stresses $\sigma_{xz} = \sigma_{yz} = 0$; the in-plane displacement components at a point can be expressed as

$$u_x = u_{x0} - z\frac{\partial w}{\partial x} \tag{A-3}$$

$$u_y = u_{y0} - z\frac{\partial w}{\partial x} \tag{A-4}$$

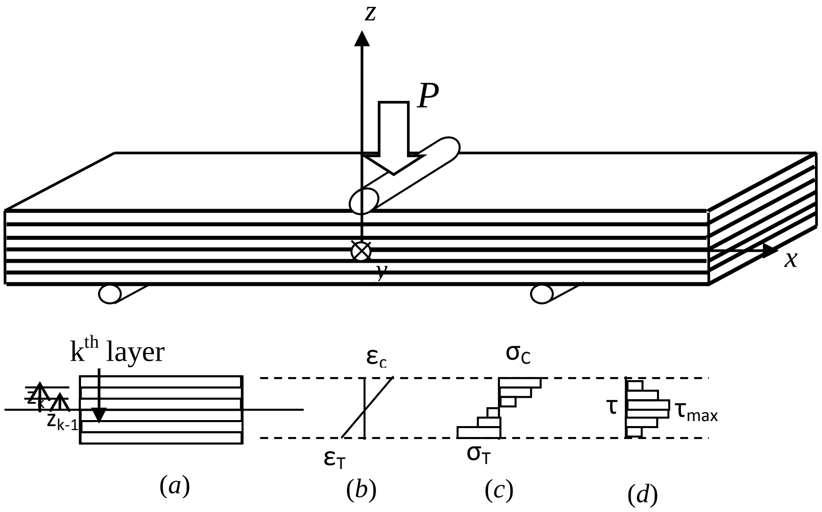

Figure A-2. Schematic diagram of three-point bending test. (*a*) *y*-*z* section at the mid-span, (*b*) strain distribution, (*c*) normal stress distribution, and (*d*) shear stress distribution.

Thus the strain-displacement relations are of the form:

$$\epsilon_x = \epsilon_x^0 + zk_x \tag{A-5}$$

$$\epsilon_y = \epsilon_y^0 + zk_y \tag{A-6}$$

$$\epsilon_{xy} = \epsilon_{xy}^{0} + zk_{xy} \tag{A-7}$$

where

$$\epsilon_x^0 = \frac{\partial u^0}{\partial x}, \quad \epsilon_y^0 = \frac{\partial u^0}{\partial y}, \quad \epsilon_{xy}^0 = \frac{\partial u^0}{\partial y} + \frac{\partial v^0}{\partial x} \tag{A-8}$$

$$k_x = -\frac{\partial^2 w}{\partial x^2}, \quad k_y = -\frac{\partial^2 w}{\partial y^2}, \quad k_{xy} = -2\frac{\partial^2 w}{\partial x \partial y} \tag{A-9}$$

By assuming that the transverse shear strains ϵ_{13} and ϵ_{23} are negligible, the stress equilibrium equation for the kth layer can be written with the consideration of only the equations of motion terms involving products of stresses and plate slopes and neglecting other nonlinear terms (Whitney, 1987):

$$\frac{\partial \sigma_{xx}^k}{\partial x} + \frac{\partial \tau_{yx}^k}{\partial y} + \frac{\partial \tau_{xz}^k}{\partial z} = 0 \tag{A-10}$$

$$\frac{\partial \tau_{xy}^k}{\partial x} + \frac{\partial \sigma_{yy}^k}{\partial y} + \frac{\partial \tau_{yz}^k}{\partial z} = 0 \tag{A-11}$$

$$\frac{\partial}{\partial x}\left(\tau_{xz}^k + \sigma_{xx}^k \frac{\partial w}{\partial x} + \tau_{xy}^k \frac{\partial w}{\partial y}\right) + \frac{\partial}{\partial y}\left(\tau_{yz}^k + \tau_{xy}^k \frac{\partial w}{\partial x} + \sigma_{yy}^k \frac{\partial w}{\partial y}\right) + \frac{\partial}{\partial z}\left(\sigma_z^k + \tau_{xz}^k \frac{\partial w}{\partial x} + \tau_{yz}^k \frac{\partial w}{\partial y}\right) = 0 \tag{A-12}$$

Now the stress and moment resultants (Figure A-3) can be expressed as:

$$\left(N_x, N_y, N_{xy}\right) = \int_{-h/2}^{h/2} \left(\sigma_{xx}^k, \sigma_{yy}^k, \tau_{xy}^k\right) dz \tag{A-13}$$

$$\left(Q_x, Q_y\right) = \int_{-h/2}^{h/2} \left(\tau_{xz}^k, \tau_{yz}^k\right) dz \tag{A-14}$$

$$\left(M_x, M_y, M_{xy}\right) = \int_{-h/2}^{h/2} \left(\sigma_{xx}^k, \sigma_y^k, \tau_{xy}^k\right) z dz \tag{A-15}$$

From Eqs. A-10 through A-15, the force equilibriums can be expressed

$$\frac{\partial N_x}{\partial x} + \frac{\partial N_{xy}}{\partial y} = 0 \tag{A-16}$$

$$\frac{\partial N_{xy}}{\partial x} + \frac{\partial N_y}{\partial y} = 0 \tag{A-17}$$

$$\frac{\partial M_x}{\partial x} + \frac{\partial M_{xy}}{\partial y} - Q_x = 0 \qquad \text{(A-18)}$$

$$\frac{\partial M_{xy}}{\partial x} + \frac{\partial M_y}{\partial y} - Q_y = 0 \qquad \text{(A-19)}$$

$$N_x \frac{\partial^2 w}{\partial x^2} + 2N_{xy} \frac{\partial^2 w}{\partial x \partial y} + N_y \frac{\partial^2 w}{\partial y^2} + \frac{\partial Q_x}{\partial x} + \frac{\partial Q_y}{\partial y} + q = 0 \qquad \text{(A-20)}$$

$$\frac{\partial^2 M_x}{\partial x^2} + 2\frac{\partial^2 M_{xy}}{\partial x \partial y} + \frac{\partial^2 M_y}{\partial y^2} + N_x \frac{\partial^2 w}{\partial x^2} + 2N_{xy} \frac{\partial^2 w}{\partial x \partial y} + N_y \frac{\partial^2 w}{\partial y^2} + q = 0 \qquad \text{(A-21)}$$

where $q = \sigma_z^k\left(\frac{h}{2}\right) - \sigma_z^k\left(-\frac{h}{2}\right)$.

In addition, by assuming an approximate state of plane stress, the transverse normal strain ϵ_z can be calculated in terms of lamina stiffness through generalized Hooke’s law:

$$\epsilon_z = -\frac{c_{13}}{c_{33}}\epsilon_x - \frac{c_{23}}{c_{33}}\epsilon_y - \frac{c_{36}}{c_{33}}\epsilon_{xy} \qquad \text{(A-22)}$$

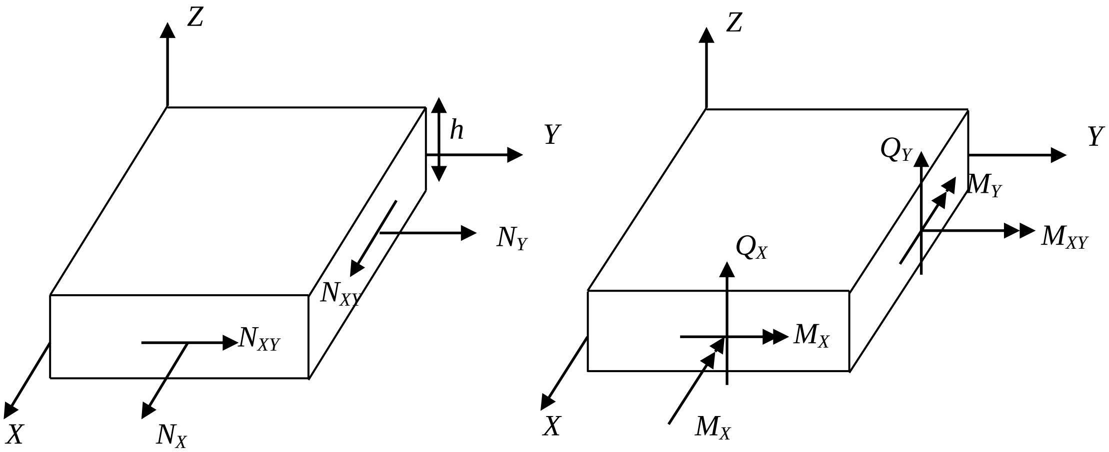

Figure A-3. Force and moment resultants.

The transverse strain in the laminate is related to the planar strains and needs to be considered for determining the laminate stress in *z*-direction. Thus, for a given layer (kth) within the laminate, the stress-strain relationship is

$$\begin{bmatrix} \sigma_{xx}^{k} \\ \sigma_{yy}^{k} \\ \sigma_{xy}^{k} \end{bmatrix} = \begin{bmatrix} Q_{11}^{k} & Q_{12}^{k} & Q_{16}^{k} \\ Q_{12}^{k} & Q_{22}^{k} & Q_{26}^{2} \\ Q_{16}^{k} & Q_{26}^{k} & Q_{66}^{k} \end{bmatrix} \begin{bmatrix} \epsilon_{x} \\ \epsilon_{y} \\ \epsilon_{xy} \end{bmatrix} \tag{A-23}$$

where the stiffness elements can be obtained as

$$Q_{ij} = c_{ij} - \frac{c_{i3}c_{j3}}{c_{33}} \tag{A-24}$$

With Eqs. (A-7) and (A-23) and the assumption that the strain varies linearly across the thickness, the stress can be expressed as

$$[\sigma]_{x,y}^{k} = [Q]_{x,y}^{k}[\epsilon^{0}\,]_{x,y} + z[Q]_{x,y}^{k}[k]_{x,y} \tag{A-25}$$

where $[\sigma]_{x,y}^{k}$ is the stresses in the (*x*,*y*)-coordinate system of the k$^{\text{th}}$ layer, $[Q]_{x,y}^{k}$ is the stiffness matrix in the (*x*,*y*)-coordinate system of the k$^{\text{th}}$ layer, and $[k]_{x,y}$ is the curvature of the laminate.

Because of the discontinuous variation of out-of-plane stresses from layer to layer, it is convenient to treat the integrated effect of these stresses in the laminate. Thus, the force and moment resultants of the laminate can be obtained from Eqs. (A-13), (A-14), (A-15), and (A-23) such that

$$\begin{bmatrix} N_{x} \\ N_{y} \\ N_{xy} \\ M_{x} \\ M_{y} \\ M_{xy} \end{bmatrix} = \begin{bmatrix} A_{11} & A_{12} & A_{16} & B_{11} & B_{12} & B_{16} \\ A_{12} & A_{22} & A_{26} & B_{12} & B_{22} & B_{26} \\ A_{16} & A_{26} & A_{66} & B_{16} & B_{26} & B_{66} \\ B_{11} & B_{12} & B_{16} & D_{11} & D_{12} & D_{16} \\ B_{12} & B_{22} & B_{26} & D_{12} & D_{22} & D_{26} \\ B_{16} & B_{26} & B_{66} & D_{16} & D_{26} & D_{66} \end{bmatrix} \begin{bmatrix} \epsilon_{x}^{0} \\ \epsilon_{y}^{0} \\ \epsilon_{xy}^{0} \\ k_{x} \\ k_{y} \\ k_{xy} \end{bmatrix} \tag{A-26}$$

where the [A], [B] and [D] matrices can be calculated based on the lamina position and properties (Agarwal, 1980) :

$$A_{ij} = \sum_{k=1}^{n} Q_{ij}^{k}(z_{k} - z_{k-1}) \tag{A-27}$$

$$B_{ij} = \frac{1}{2}\sum_{k=1}^{n} Q_{ij}^{k}(z_{k}^{2} - z_{k-1}^{2}) \tag{A-28}$$

$$D_{ij} = \frac{1}{3}\sum_{k=1}^{n} Q_{ij}^{k}(z_k^3 - z_{k-1}^3) \quad \text{(A-29)}$$

4. Calculation of elastic stiffness

To use the above relations for practical calculations, it is necessary to transfer the engineering constants to the reference coordinate system (Figure A-1). This is particularly important to angle-ply laminates as the ply axes and laminate axes are typically different. By using the stress (T_σ) and strain (T_ϵ) transformation matrices, the transformations can be expressed as:

$$C = T_\sigma^{-1} C' T_\epsilon \quad \text{(A-30)}$$

where C and C' are the stiffness matrices in the global or reference coordinate system and material coordinate system of individual lamina, respectively.

As the calculation is based on the laminate of symmetry with respect to the mid-plane, it needs 13 constants for each lamina of the laminate to fully express the stress-strain relations. If a particular ply inside the laminate has an angle θ with respect to the X_1-axis, by assuming$cos\theta = m, sin\theta = n$, the stiffness elements in the global coordinate system can be obtained as

$$\begin{aligned}
C_{11} &= C_{11}'m^4 + 2m^2n^2(C_{12}' + 2C_{66}') + C_{22}'n^4 \\
C_{12} &= m^2n^2(C_{11}' + C_{22}' - 4C_{66}') + C_{12}'(m^4 + n^4) \\
C_{13} &= C_{13}'m^2 + C_{23}'n^2 \\
C_{16} &= mn[C_{11}'m^2 - C_{22}'n^2 - (C_{12}' + 2C_{66}')] \\
C_{22} &= C_{11}'n^4 + 2m^2n^2(C_{12}' + 2C_{66}') + C_{22}'m^4 \qquad \text{(A-31)} \\
C_{23} &= C_{13}'n^2 + C_{23}'m^2 \\
C_{26} &= mn[C_{11}'n^2 - C_{22}'m^2 + (C_{12}' + 2C_{66}')(m^2 - n^2)] \\
C_{33} &= C_{33}'
\end{aligned}$$

$$C_{36} = (C_{23}^{'} - C_{13}^{'})mn$$

$$C_{44} = C_{44}^{'}m^2 + C_{55}^{'}n^2$$

$$C_{45} = \left(C_{44}^{'} - C_{55}^{'}\right)mn$$

$$C_{55} = C_{44}^{'}n^2 + C_{55}^{'}m^2$$

$$C_{66} = (C_{11}^{'} + C_{22}^{'} - 2C_{12}^{'})m^2n^2 + C_{66}^{'}(m^2 - n^2)^2$$

When the lamina axes coincides with the global coordinate axes, i.e. $\theta = 0^0$ then $m = \cos\theta = 1 \; and \; n = sin\theta = 0$. The example of this type is a UD lamina. Thus, above equations become,

$$\begin{gathered} C_{11} = C_{11}^{'}\,; \quad C_{12} = C_{12}^{'}\,; C_{13} = C_{13}^{'} \\ C_{16} = 0\,; \quad C_{22} = C_{22}^{'} \quad ; C_{23} = C_{23}^{'} \\ C_{26} = 0; \quad C_{33} = C_{33}^{'}; C_{36} = 0 \\ C_{44} = C_{44}^{'};\; C_{45} = 0;\; C_{55} = C_{55}^{'};\; C_{66} = C_{66}^{'} \end{gathered} \qquad \text{(A-32)}$$

Again for a UD lamina with transverse isotropy, i.e. if x_1 is perpendicular to the axis of isotropy then$C_{33} = C_{22}, C_{13} = C_{12}, C_{55} = C_{66}, C_{44} = \frac{1}{2}(C_{22} - C_{23})$. The stress elements can be expressed in the contracted form:

$$\begin{bmatrix} \sigma_1 & \sigma_6 = \tau_{12} & \sigma_5 = \tau_{13} \\ \sigma_6 = \tau_{12} & \sigma_2 & \sigma_4 = \tau_{23} \\ \sigma_5 = \tau_{13} & \sigma_4 = \tau_{23} & \sigma_3 \end{bmatrix} \qquad \text{(A-33)}$$

where $\sigma_1, \sigma_2, \sigma_3$ are the normal stresses along the reference axes and $\sigma_4, \sigma_5, \sigma_6$ or $\tau_{23}, \tau_{13}, \tau_{12}$ are the shear stresses in the reference planes.

For a special orthotropic material, there is no coupling between normal stresses and shear strains or between shear stresses and normal strains; also, no coupling exists between shear stresses (Daniel & Ishai, 2006). For a beam the normal stress σ_3 is negligible and the interlaminar shear stress τ_{13} is of particular interest in the data reduction of composite beam tests. The stress continuity of a homogeneous, isotropic material states that τ_{13} and τ_{23} are the same (Figure A-4), i.e. the interlaminar shear stress and transverse shear stress are the same. On the other hand, for a composite laminate, the interlaminar shear stresses are varying in different layers, and the transverse shear stress cannot be directly calculated. Thus, Eq. (3.27) is sought.

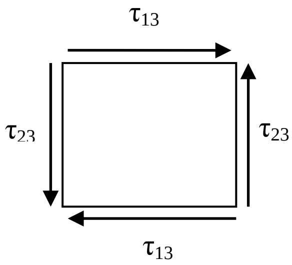

Figure A-4. Shear stress along the edges of a material cube.

APPENDIX B. SC-15: TOUGHENED EPOXY RESIN SYSTEM

(Source: Applied Poleramic Inc., Benicia, CA**)**

Product Description

SC-15 is a very low viscosity two-phase toughened epoxy resin system. SC-15 was specifically developed for Vacuum Assisted Resin Transfer Molding (VARTM) processes. The pot-life and viscosity have been tailored to allow infusion at 77ºF. This resin system works very well in structural and ballistic applications that require good damage resistance.

Application

Infuse preform at 75-80ºF. Allow resin to vitrify at 77ºF overnight or 140ºF for two hours. Post-cure four hours at 200ºF (ramp temperature to 200ºF with a rate 2-4 ºF/min). If composite part is removed from mold and post-cured freestanding, use a 25ºF/hr ramp or step from 140ºF.

Product Application

- Low viscosity amine cured epoxy resin system
- VARTM processing or equivalent
- Advanced composite resin for carbon, glass, Kevlar, or other fibers
- Room temperature cure, 200°F post-cure
- Shelf Life: 24 mos. in closed drum at ambient.

PHYSICAL PROPERTIES

Viscosity @ 77ºF		
	Mixed	300 cP
	Resin	580 cP
	Hardener	45 cP
Cured Density:		1.09 g/cm3
Wt. Gal:		
	Resin	9.42 lbs/gal
	Hardener	8.02 lbs/gal

CURED RESIN MECHANICALS

Tg (dry)		220°F
Tg (wet)		178°F
Modulus E' at ambient	390 ksi	
$G_{ic,}$ in-lb/in^2		5.65 in-lb/in^2
Elongation		6.0%
Tensile Strength	9.0 ksi	
Tensile Mod		3.8 msi
Kic		1400 psi-in$^{.5}$
% water pickup (10 days @ 180°F)		1.7

The following data was generated by the Center for Composite Materials at the University of Delaware & the Army Research Lab

NEAT RESIN

Temp, °F	Storage Modulus (Dry), MPa
85	1970
180	1180

ADHESIVE PROPERTIES

T Peel, lbs/in^2	
RT	18

Aluminum Lap Shear	
RT	3900 psi
160°F	2050 psi

** Need to add glass beads or equivalent for bond line control.

Tg Dry, °F	212
Tg Wet, °F (after 400 hrs @ 160°F)	183
Toughness	High
Tensile Str, psi	8,100
Tensile Mod, msi	3.8
% elongation	6.0
Viscosity, cps (77°F)	300

*** The University of Delaware Center for Composite Materials did a thorough evaluation for material property balance to meet requirements for Future Combat Systems ground vehicles. This optimized formula was a blend of SC-15 and SC-79 which is now designated *CCMFCS2, also available from Applied Poleramic Inc.*

S-2 Woven Roving, $G_{ic,}$ J/M^2 (ASTM D 5528-94a), Initiation – 688 Propagation - 1104

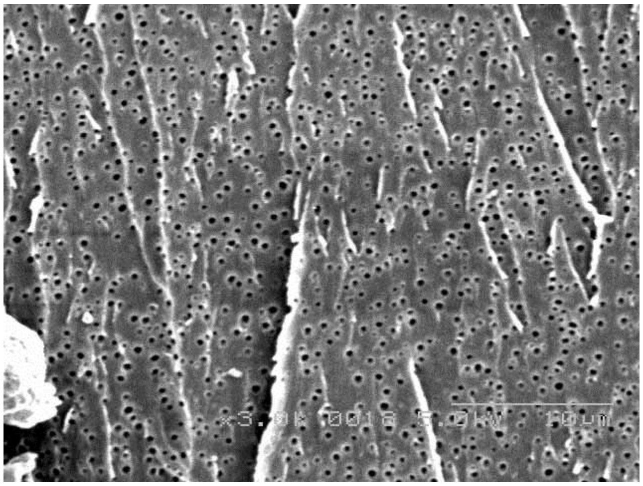

SEM micrograph @3K

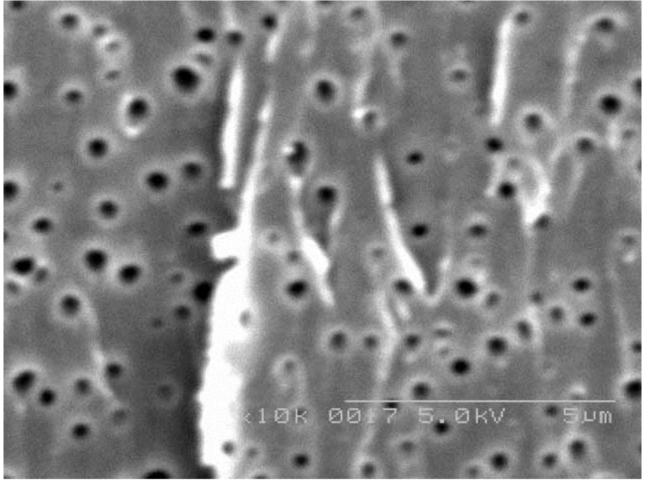

SEM micrograph @10K

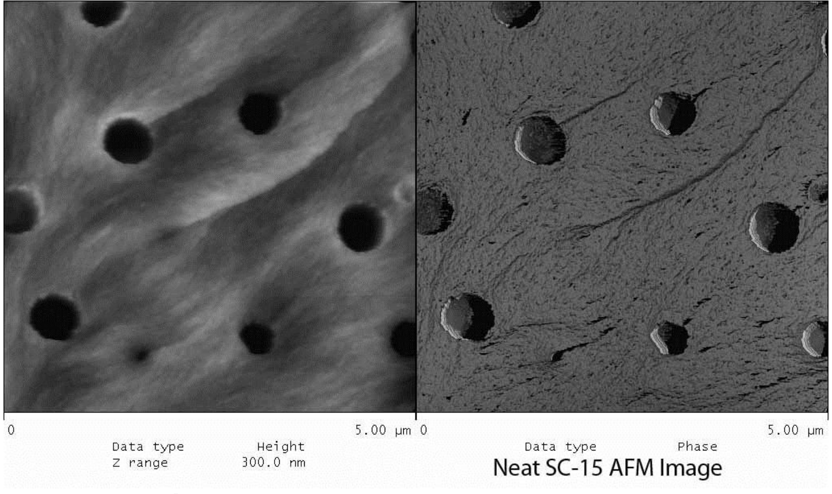

AFM micrograph

All data given is believed to be accurate based on the material tested. Since the processing and testing is application and user specific, API has no assurance of how the product will be used and therefore cannot make any guarantees as to these properties or the final performance.

RELEVANT PUBLICATIONS & PRESENTATIONS/POSTS

Publications

1. Chen, Q., Zhang, L. F., **Rahman, A.**, Zhou, Z. P., Wu, X. F., & Fong, H. (2011) Hybrid multi-scale epoxy composites made of conventional carbon fiber fabrics with interlaminar regions containing electrospun carbon nanofiber mats. Composites Part A: Applied Science and Manufacturing 42, 2036-2042.
2. Sinha-Ray, S., Pelot, D. D., Zhou, Z. P., **Rahman, A.**, Wu, X. F., & Yarin, A.L. (2012) Encapsulation of self-healing materials by coelectrospinning, emulsion electrospinning and solution blowing and intercalation. Journal of Materials Chemistry (Accepted).
3. Chen, Q., Zhao, Y., Zhou, Z. P., **Rahman, A.**, Wu, X. F., & Fong, H. (2012) Fabrication and evaluation of hybrid multi-scale epoxy composites reinforced with conventional carbon fiber fabrics surface-covered with electrospun carbon nanofiber mats. Composites Part B: Engineering (to be submitted).
4. **Rahman, A.** & Wu, X. F. (2012) Computational scaling analysis of the mechanical properties of clay/polymer nanocomposites," Journal of Materials Science (to be submitted).
5. **Rahman, A.** & Wu, X. F. (2012) A differential experimental investigation on delamination of polymer composites (in preparation).
6. Wu, X. F., **Rahman, A.**, Zhou, Z. P., & Yarin, A.L. (2012) Core-shell nanofibers for interfacial self-healing of polymer composites (in preparation).
7. Wu, X. F., **Rahman, A.**, Zhou, Z. P., & Fong, H. (2012) Improvement of the interlinear fracture toughness of polymer composites by incorporation of electrospun nanofibers at interfaces (in preparation).

Book chapter

1. Wu, X.F., Zhou, Z. P., **Rahman, A.**, & Bedarkar, A. (2012) Mechanical properties of continuous nanofibers: Characterization and mechanics", Nanostructures: Properties, Production Methods and Applications [Editors: Yu (Roger) Dong, et al.] Nova Publisher, USA (2012) (accepted).

Post/Presentations

1. **Rahman, A.,** Zhou, Z. P., & Wu, X.F. (2011) Manufacturing of novel continuous nanofibers for advanced structural applications. *ND-SD 2011 Joint EPSCoR Conference*, Fargo, ND.
2. Zhou, Z. P., **Rahman, A.,** & Wu, X.F. (2011) Electrospun nanofibers for use of porous electrodes of supercapacitor-battery hybrids. *ND-SD 2011 Joint EPSCoR Conference*, Fargo, ND.
3. Wu, X.F., Zhou, Z. P., Jenson, R.A., & **Rahman, A.** (2011) Manufacturing of novel continuous nanofibers for advanced structural and storage energy applications. NDSU- SDSU-UND Engineering Research Summit, Fargo, ND.
4. **Rahman, A.** (November 7, 2011) Experimental and computational study of the interfacial mechanical properties of novel hybrid micro/nanofiber-reinforced polymer composites. Graduate seminar presentation. Mechanical Engineering Department, NDSU, Fargo, ND.

VITA

Mr. Rahman received his B.S. degree in Civil Eng. from the Bangladesh Univ. of Eng. & Tech (BUET), Dhaka, Bangladesh in June, 2007. After graduation, Mr. Rahman worked as a design engineer at a steel manufacturing company in Bangladesh. He, as a M.S. graduate, joined the Civil Eng. Dept at NDSU in January, 2009, and then transferred to ME Dept. in August, 2010. He has worked as a research and teaching assistant in the department of Civil and Mechanical engineering at NDSU. During the course of his master's study he has worked on the development of novel hybrid multiscale fiber composites with improved delamination toughness and unique interfacial self-repairing function. The research was sponsored by the ND NASA EPSCoR and NDSU Development Foundation. He has started working as a Technical Support Engineer at Baker Hughes Inc. from Feb. 2012.